

A DENSITY FUNCTIONAL THEORY INVESTIGATION FOR SOLID STATE
HYDROGEN STORAGE MATERIALS

A THESIS SUBMITTED TO
THE GRADUATE SCHOOL OF NATURAL AND APPLIED SCIENCES
OF
MIDDLE EAST TECHNICAL UNIVERSITY

BY

AYŞENUR GENCER

IN PARTIAL FULFILLMENT OF THE REQUIREMENTS
FOR
THE DEGREE OF DOCTOR OF PHILOSOPHY
IN
PHYSICS

MAY 2019

Approval of the thesis:

**A DENSITY FUNCTIONAL THEORY INVESTIGATION FOR SOLID
STATE HYDROGEN STORAGE MATERIALS**

submitted by **AYŞENUR GENCER** in partial fulfillment of the requirements for the degree of **Doctor of Philosophy in Physics Department, Middle East Technical University** by,

Prof. Dr. Halil Kalıpçılar
Dean, Graduate School of **Natural and Applied Sciences**

Prof. Dr. Altuğ Özpıneci
Head of Department, **Physics**

Assoc. Prof. Dr. Hande Toffoli
Supervisor, **Physics, METU**

Assoc. Prof. Dr. Gökhan Sürücü
Co-Supervisor, **Electric and Energy, Ahi Evran University**

Examining Committee Members:

Prof. Dr. Mehmet Çakmak
Physics , Gazi University

Assoc. Prof. Dr. Hande Toffoli
Physics, METU

Prof. Dr. Hatice Kökten
Physics, METU

Prof. Dr. Mehmet Parlak
Physics, METU

Assoc. Prof. Dr. Yavuz Dede
Chemistry, Gazi University

Date: 07.05.2019

I hereby declare that all information in this document has been obtained and presented in accordance with academic rules and ethical conduct. I also declare that, as required by these rules and conduct, I have fully cited and referenced all material and results that are not original to this work.

Name, Surname: Ayşenur Gencer

Signature:

ABSTRACT

A DENSITY FUNCTIONAL THEORY INVESTIGATION FOR SOLID STATE HYDROGEN STORAGE MATERIALS

Gencer, Ayşenur
Doctor of Philosophy, Physics
Supervisor: Assoc. Prof. Dr. Hande Toffoli
Co-Supervisor: Assoc. Prof. Dr. Gökhan Sürücü

May 2019, 146 pages

The world's energy demand is increasing with the population growth and technology development. In addition, the electronic devices are an essential part of the daily life that require portable energy sources. Therefore, energy storage is necessary in order to store energy from the renewable energy sources and also provide portable energy sources for electronic devices. Hydrogen being the most abundant element in the world, is a good energy carrier with high energy density. Also, hydrogen does not release greenhouse gases that contribute to the global warming. In addition to these properties, it can be stored in metals with physical or chemical bonds that allows an interest to the solid state hydrogen storage materials which are considered as a promising solution with effective and safe hydrogen storage. For these reasons, its use in fuel cells is emerging. Considering the cost and difficulties of experimental studies for determination of new materials to be used in hydrogen storage, theoretical studies have become a tool for experimental studies. The most important method of theoretical studies is Density Functional Theory (DFT). This method is popular in recent years because it can be used without depending on any experimental data. In this study, the first principles calculations have been performed to investigate the hydrogen storage properties of perovskite materials that could be a possible candidate material group for the solid state hydrogen storage method due to having stability and ceramic nature. The studied perovskite materials are divided into

three groups as perovskite materials with $BaXO_3$ ($X = Sc$ or Y) and $XTiO_3$ ($X = Mg$ or Ca) compounds, anti-perovskite materials with Ca_3XH ($X = C$ or N) compounds and perovskite type hydrides with $XNiH_3$ ($X = Li, Na$ or K) compounds. The structural, mechanic, electronic, thermodynamic and lattice dynamic properties of these materials have been examined by using the Vienna Ab-initio Simulation Package (VASP) based on DFT. The results have been compared with the available results from the literature and it has been found that the results are consistent with the literature. Furthermore, the hydrogen doping studies to $BaXO_3$, $XTiO_3$ and Ca_3XH compounds have been performed and the gravimetric hydrogen storage capacities and the hydrogen desorption temperatures have been obtained to reveal the properties of these materials for the hydrogen storage applications.

Keywords: Hydrogen Storage, Density Functional Theory, Perovskite Materials

ÖZ

KATI-HAL HİDROJEN DEPOLAMA MALZEMELERİNİN YOĞUNLUK FONKSİYONEL TEORİSİ İLE İNCELENMESİ

Gencer, Ayşenur

Doktora, Fizik

Tez Danışmanı: Doç. Dr. Hande Toffoli

Ortak Tez Danışmanı: Doç. Dr. Gökhan Sürücü

Mayıs 2019, 146 sayfa

Dünya'nın enerji talebi, nüfus artışı ve teknolojinin gelişmesiyle birlikte artmaktadır. Özellikle taşınabilir enerji kaynaklarına ihtiyaç duyan elektronik cihazlar günlük hayatın önemli bir parçası haline gelmiştir. Bu nedenle, yenilenebilir enerji kaynaklarından üretilen enerjinin depolanması ve ayrıca elektronik cihazlara taşınabilir enerji kaynağı sağlamasından dolayı enerji depolama önemli bir gerekliliktir. Hidrojen evrende en çok bulunan element olarak yüksek enerji yoğunluğuna sahip iyi bir enerji taşıyıcıdır. Ayrıca, hidrojen küresel ısınmaya neden olan sera gazlarını salmamaktadır. Bu özelliklere ek olarak, hidrojenin metallerde fiziksel ya da kimyasal bağlarla depolanabilmesi, hidrojen depolama konusunda etkili ve güvenli bir umut verici çözüm olarak görülen katı-hal hidrojen depolama konusunda bir ilginin olmasını sağlamıştır. Bu nedenlerle, hidrojenin yakıt pillerinde kullanımı ortaya çıkmaktadır. Hidrojen depolamada kullanılacak yeni malzemelerin belirlenebilmesi için deneysel çalışmaların maliyeti, zorlukları dikkate alındığında, teorik çalışmalar deneysel çalışmaların aracı durumuna gelmiştir. Teorik çalışmaların en önemli metodu ise yoğunluk fonksiyoneli teorisi (DFT). Bu metodun son yıllarda oldukça popüler olmasının nedeni, hiçbir deneysel veriye ihtiyaç duymadan kullanılabilmesidir. Bu çalışmada, ilk prensipler hesaplamaları ile katı-hal hidrojen

depolama için aday malzeme grubu olabilecek kararlı ve seramik özellik gösteren perovskite malzemelerin hidrojen depolama özellikleri incelenmiştir. Çalışılan perovskite malzemeleri, $BaXO_3$ ($X = Sc$ or Y) and $XTiO_3$ ($X = Mg$ or Ca) bileşikleri ile perovskite malzemeler, Ca_3XH ($X = C$ or N) bileşikleri ile de anti-perovskite malzemeler ve $XNiH_3$ ($X = Li, Na$ or K) bileşikleri ile de perovskite tipi hidrürler olarak üç gruba ayrılmıştır. Bu bileşiklerin yapısal, mekanik, elektronik, termodinamik ve örgü dinamik özellikleri DFT tabanlı Vienna Ab-initio Simulation Package (VASP) ile incelenmiştir. Elde edilen sonuçlar literatürdeki mevcut çalışmalar ile karşılaştırılmış ve sonuçların literatür ile uyumlu olduğu bulunmuştur. Bunlara ek olarak $BaXO_3$, $XTiO_3$ ve Ca_3XH bileşiklerine hidrojen katılma çalışmaları yapılmış olup bu bileşiklerin hidrojen depolama uygulamalarında kullanımını belirlemek için hidrojen ağırlık depolama kapasitesileri ve hidrojen geri bırakma sıcaklıkları elde edilmiştir.

Anahtar Kelimeler: Hidrojen Depolama, Yoğunluk Fonksiyoneli Teorisi, Perovskite Malzemeler

To My Family

ACKNOWLEDGMENTS

I would like to thank my advisor Assoc. Prof. Hande Toffoli for her support. Also, I would like to express my deepest gratitude to my co-advisor Assoc. Prof. Gökhan Sürücü for his guidance, patience and immense knowledge through my studies. His support gives me the strength to finish this study. His advice on both research as well as on my career have been invaluable.

Besides my advisors, I would like to thank my thesis progress committee: Prof. Hatice Kökten and Assoc. Prof. Yavuz Dede for their comments. Also, I would like to thank Prof. Mehmet Çakmak and Prof. Mehmet Parlak for their comments.

My sincere thanks also goes to Dr. Özge Sürücü for her support when I need and her belief in me in my dark times. Also, I would like to thank my friends Kübra Erkan Türkmen and Fatih Türkmen for their support and friendship.

Last but not least I would like to thank my family who encouraged me and prayed for me throughout the time of my study.

I would like to thank Turkish Scientific and Technical Research Council, TÜBİTAK, for awarding the scholarship (2211/A) during my doctorate programe.

TABLE OF CONTENTS

ABSTRACT	v
ÖZ	vii
ACKNOWLEDGMENTS	x
TABLE OF CONTENTS	xi
LIST OF TABLES	xiv
LIST OF FIGURES	xviii
LIST OF ABBREVIATIONS	xxii
CHAPTERS	1
1. INTRODUCTION	1
2. THEORETICAL BACKGROUND.....	7
2.1. Density Functional Theory	7
2.1.1. Functionals for Exchange and Correlation	13
2.1.2. Pseudopotentials	14
2.2. Crystal Systems	16
2.3. Band Theory	18
2.4. Mechanical Properties	21
2.5. Vibrational Properties.....	29
2.6. Hydrogen Storage Properties.....	33
2.7. Perovskite Materials	35
2.8. VASP Software	37
3. HYDROGEN STORAGE STUDIES FOR PEROVSKITE MATERIALS	39
3.1. Introduction	39

3.2. Studies for $BaXO_3$ (X= Sc or Y).....	39
3.2.1. Structural Optimization for $BaXO_3$	39
3.2.2. Electronic Properties for $BaXO_3$	45
3.2.3. Mechanical Properties for $BaXO_3$	49
3.2.4. Vibrational Properties for $BaXO_3$	54
3.2.5. Hydrogen Storage Studies for $BaXO_3$	55
3.3. Studies for $XTiO_3$ (X = Mg or Ca)	65
3.3.1. Structural Optimization for $XTiO_3$	65
3.3.2. Electronic Properties for $XTiO_3$	67
3.3.3. Mechanical Properties for $XTiO_3$	70
3.3.4. Hydrogen Storage Studies for $XTiO_3$	74
4. HYDROGEN STORAGE STUDIES FOR ANTI-PEROVSKITE MATERIALS	
.....	83
4.1. Introduction.....	83
4.2. Studies for Ca_3XH (X= C or N).....	83
4.2.1. Structural Optimization for Ca_3XH	83
4.2.2. Mechanical Properties for Ca_3XH	88
4.2.3. Thermo-elastic Properties for Ca_3XH	92
4.2.4. Electronic Properties for Ca_3XH	98
5. HYDROGEN STORAGE STUDIES FOR PEROVSKITE TYPE HYDRIDES	
.....	103
5.1. Introduction.....	103
5.2. Structural Optimization for $XNiH_3$	103
5.3. Electronic Properties for $XNiH_3$	105

5.4. Mechanical Properties for $XNiH_3$	108
5.5. Vibrational and Thermal Properties for $XNiH_3$	111
6. CONCLUSION.....	117
REFERENCES.....	119
APPENDICES	127
A. Band Structure and Partial Density of States for $BaXO_3$ Perovskite Compounds	127
B. Input Files for VASP	137
CURRICULUM VITAE	141

LIST OF TABLES

Table 2.1 Seven crystal systems and the relations between the lattice vectors and the lattice angles	17
Table 2.2 The Born stability criteria for the possible crystal phases of the perovskite materials.....	22
Table 2.3 The k-points (MP for Monkhorst-Pack grid and GC for Gamma centered grid) and the cut off energies($E_{\text{cut off}}$ in eV) for the studied compounds.....	38
Table 3.1 The optimized lattice parameters (a, b, c in Å), the calculated formation energies (ΔE_{For} in eV/atom) and the atomic positions for BaXO_3	41
Table 3.2 The Bader net charges (in units of e per unit cell) for BaXO_3	48
Table 3.3 The calculated elastic constants (C_{ij} in GPa) for BaXO_3	50
Table 3.4 Bulk modulus (B in GPa), Shear modulus (G in GPa), Young's modulus (E in GPa), Poisson's ratio (ν), G/B ratio and B/G ratio for the mechanically stable phases of BaXO_3	51
Table 3.5 The minimum and maximum values of Young's modulus (E in GPa), linear compressibility (β), shear modulus (G in GPa), and Poisson's ratio(ν) for BaXO_3 ..	51
Table 3.6 The optimized lattice parameters (a, b, c in Å), the calculated formation energies (ΔE_{For} in eV/atom) and atomic positons for $\text{BaScO}_3\text{H}_{0.5}$, BaYO_3H_3 , and BaYO_3H_9	57
Table 3.7 The Bader net charges (in units of e per unit cell) for $\text{BaScO}_3\text{H}_{0.5}$ and BaYO_3H_3	62
Table 3.8 The calculated elastic constants (C_{ij} in GPa) for $\text{BaScO}_3\text{H}_{0.5}$ and BaYO_3H_3	63
Table 3.9 Bulk modulus (B in GPa), Shear modulus (G in GPa), Young's modulus (E in GPa), Poisson's ratio (ν), G/B ratio and B/G ratio for $\text{BaScO}_3\text{H}_{0.5}$ and BaYO_3H_3	63

Table 3.10 The minimum and maximum values of Young's modulus (E in GPa), linear compressibility (β), shear modulus (G in GPa), and Poisson's ratio(ν) for BaScO ₃ H _{0.5} and BaYO ₃ H ₃	65
Table 3.11 The optimized lattice parameters (a in Å), the calculated formation energies (ΔE_{For} in eV/atom) and the atomic positions for XTiO ₃	66
Table 3.12 The Bader net charges (in units of e per unit cell) for XTiO ₃	70
Table 3.13 The calculated elastic constants (C_{ij} in GPa) for XTiO ₃	71
Table 3.14 Bulk modulus (B in GPa), Shear modulus (G in GPa), Young's modulus (E in GPa), Poisson's ratio (ν), G/B ratio and B/G ratio for XTiO ₃	71
Table 3.15 The maximum and minimum values of Young's modulus (E in GPa), linear compressibility (β), shear modulus (G in GPa), and Poisson's ratio(ν) for XTiO ₃ ...	74
Table 3.16 The optimized lattice parameters (a in Å), the calculated formation energies (ΔE_{For} in eV/atom) and the atomic positions for XTiO ₃ H _x	75
Table 3.17 The Bader net charges (in units of e per unit cell) for XTiO ₃ H _x	80
Table 3.18 The calculated elastic constants (C_{ij} in GPa) for XTiO ₃ H _x	80
Table 3.19 Bulk modulus (B in GPa), Shear modulus (G in GPa), Young's modulus (E in GPa), Poisson's ratio (ν), G/B ratio and B/G ratio for CaTiO ₃ H ₆	80
Table 3.20 The minimum and maximum values of Young's modulus (E in GPa), linear compressibility (β), shear modulus (G in GPa), and Poisson's ratio(ν) for CaTiO ₃ H ₆	82
Table 4.1 The lattice constants (a in Å), the calculated formation energies (ΔE_{For} in eV/atom) and the atomic positions for Ca ₃ XH	84
Table 4.2 The lattice constants (a in Å), the calculated formation energies (ΔE_{For} in eV/atom) and the atomic positions for Ca ₃ XH ₄ , Ca ₃ XH ₇ , Ca ₃ XH ₉ , and Ca ₃ XH ₁₀	86
Table 4.3 The gravimetric hydrogen capacities (Cwt%) and the hydrogen desorption temperatures (T in K) for Ca ₃ XH, Ca ₃ XH ₄ , Ca ₃ XH ₇ , Ca ₃ XH ₉ , and Ca ₃ XH ₁₀	88
Table 4.4 The elastic constants (C_{ij} in GPa) for Ca ₃ XH, Ca ₃ XH ₄ , Ca ₃ XH ₇ , Ca ₃ XH ₉ , and Ca ₃ XH ₁₀	89

Table 4.5 Bulk modulus (B in GPa), Shear modulus (G in GPa), Young's modulus (E in GPa), Poisson's ratio (ν), G/B ratio and B/G ratio for Ca ₃ XH, Ca ₃ XH ₄ , and Ca ₃ XH ₇	89
Table 4.6 The minimum and maximum values of Young's modulus (E in GPa), linear compressibility (β), shear modulus (G in GPa), and Poisson's ratio(ν) for Ca ₃ XH, Ca ₃ XH ₄ , and Ca ₃ XH ₇	92
Table 4.7 The Debye temperature (Θ_D in K), the longitudinal wave velocity (V_l in m/s), the transverse wave velocity (V_t in m/s), the average wave velocity (V_m in m/s), the Zener anisotropic factor (A), the anisotropic factor in shear (A_G) and compression (A_B) and the universal anisotropic factor (A^U) for Ca ₃ XH, Ca ₃ XH ₄ , and Ca ₃ XH ₇ ..	97
Table 4.8 The minimum thermal conductivities (λ_{min} in Wm ⁻¹ K ⁻¹), the average mass per atom (M_a in 10 ⁻²⁶ kg) for Clarke model and the density of number of atoms per volume (n in 10 ²⁸ m ⁻³) for Cahill model for Ca ₃ XH, Ca ₃ XH ₄ , and Ca ₃ XH ₇	98
Table 4.9 The Bader net charges (in units of e per unit cell) for Ca ₃ CH, Ca ₃ CH ₄ , Ca ₃ CH ₇ , Ca ₃ NH, and Ca ₃ NH ₄	101
Table 5.1 The optimized lattice constants (a in Å), the calculated formation energies (ΔE_{For} in eV/atom), the atomic positions, the gravimetric hydrogen storage capacities ($C_{wt\%}$) and the hydrogen desorption temperatures (T in K) for XNiH ₃	104
Table 5.2 The Bader net charges (in units of e per unit cell) for XNiH ₃	108
Table 5.3 The calculated elastic constants (C_{ij} in GPa) for XNiH ₃	108
Table 5.4 Bulk modulus (B in GPa), shear modulus (G in GPa), Young's modulus (E in GPa), Poisson's ratio (ν), G/B ratio and B/G ratio for XNiH ₃	109
Table 5.5 The minimum and maximum values of Young's modulus (E in GPa), linear compressibility (β), shear modulus (G in GPa), and Poisson's ratio(ν) for XNiH ₃	109
Table 5.6 The Debye temperature (Θ_D in K), longitudinal wave velocity (V_l in m/s), the transverse wave velocity (V_t in m/s), the average wave velocity (V_m in m/s), the Zener anisotropic factor A, the anisotropic factor in shear (A_G) and compression (A_B)and the universal anisotropic for (A^U) for XNiH ₃	111

Table 5.7 The minimum thermal conductivities (λ_{\min} in $\text{Wm}^{-1}\text{K}^{-1}$), the average mass per atom (M_a in 10^{-26} kg) for Clarke model and the density of number of atoms per volume (n in 10^{28} m^{-3}) for Cahill model for XNiH_3114

LIST OF FIGURES

Figure 2.1 The Coulomb potential and the wavefunction of a system and the pseudopotential and corresponding pseudo-wavefunction [37]	15
Figure 2.2 The energy levels of electrons when atoms come closer [54].....	19
Figure 2.3 The plot of ω versus k [75].....	32
Figure 2.4 The pressure composition isotherm for a metal-hydride system and the right plot shows the Van't Hoff relation of this material [78]	34
Figure 2.5 The ideal cubic crystal structure of perovskite materials [84]	36
Figure 2.6 (a) Orthorhombic and (b) hexagonal perovskite crystal structures [85] ..	37
Figure 3.1 The crystal structures of $BaXO_3$ for cubic, tetragonal, hexagonal, rhombohedral, and orthorhombic phases.....	40
Figure 3.2 The energy as a function of volume for different crystal phases of $BaScO_3$	42
Figure 3.3 The enthalpy as a function of pressure for different crystal phases of $BaScO_3$	43
Figure 3.4 The energy as a function of volume for different crystal phases of $BaYO_3$	43
Figure 3.5 The enthalpy as a function of pressure for different crystal phases of $BaYO_3$	44
Figure 3.6 X-ray diffraction patterns for $BaScO_3$ orthorhombic phase and $BaYO_3$ cubic phase	45
Figure 3.7 The band structure for $BaScO_3$ orthorhombic phase.....	46
Figure 3.8 The partial density of states for $BaScO_3$ orthorhombic phase	46
Figure 3.9 The band structure for $BaYO_3$ cubic phase	47
Figure 3.10 The partial density of states for $BaYO_3$ cubic phase.....	47
Figure 3.11 The electron-density distributions for (a) $BaScO_3$ orthorhombic phase and (b) $BaYO_3$ cubic phase	49

Figure 3.12 The direction dependent (a) Young's modulus, (b) linear compressibility, (c) shear modulus, and (d) Poisson's ratio both in 2D and 3D for BaScO ₃ orthorhombic phase.....	52
Figure 3.13 The direction dependent (a) Young's modulus, (b) linear compressibility, (c) shear modulus, and (d) Poisson's ratio both in 2D and 3D for BaYO ₃ cubic phase	53
Figure 3.14 Phonon dispersion curve and phonon density of states for BaScO ₃ orthorhombic phase.....	54
Figure 3.15 Phonon dispersion curve and phonon density of states for BaYO ₃ cubic phase.....	55
Figure 3.16 The crystal structure of BaScO ₃ H _{0.5}	56
Figure 3.17 The crystal structures of (a) BaYO ₃ H ₃ and (b) BaYO ₃ H ₉	56
Figure 3.18 X-ray diffraction patterns for BaScO ₃ H _{0.5} and BaYO ₃ H ₃	58
Figure 3.19 The band structure for BaScO ₃ H _{0.5}	59
Figure 3.20 The partial density of states for BaScO ₃ H _{0.5}	59
Figure 3.21 The band structure for BaYO ₃ H ₃	60
Figure 3.22 The partial density of states for BaYO ₃ H ₃	61
Figure 3.23 The electron-density distributions for (a) BaScO ₃ H _{0.5} and (b) BaYO ₃ H ₃	62
Figure 3.24 The direction dependent (a) Young's modulus, (b) linear compressibility, (c) shear modulus, and (d) Poisson's ratio in 3D for BaScO ₃ H _{0.5} and BaYO ₃ H ₃	64
Figure 3.25 The crystal structure of XTiO ₃ (X= Mg or Ca)	66
Figure 3.26 X-ray diffraction patterns for MgTiO ₃ and CaTiO ₃	67
Figure 3.27 The band structure for MgTiO ₃	68
Figure 3.28 The partial density of states for MgTiO ₃	68
Figure 3.29 The band structure for CaTiO ₃	69
Figure 3.30 The partial density of states for CaTiO ₃	69
Figure 3.31 The electron-density distributions for CaTiO ₃ (a) in (1 0 0) plane and (b) in (1 1 1) plane	70

Figure 3.32 The direction dependent (a) Young's modulus, (b) linear compressibility, (c) shear modulus, and (d) Poisson's ratio in 3D for MgTiO ₃	72
Figure 3.33 The direction dependent (a) Young's modulus, (b) linear compressibility, (c) shear modulus, and (d) Poisson's ratio in 3D for CaTiO ₃	73
Figure 3.34 The crystal structures of (a) XTiO ₃ H ₃ , (b) XTiO ₃ H ₆ and (c) XTiO ₃ H ₈ ..	74
Figure 3.35 X-ray diffraction patterns for MgTiO ₃ H ₃ , CaTiO ₃ H ₃ , CaTiO ₃ H ₆ , and CaTiO ₃ H ₈	76
Figure 3.36 The band structure for MgTiO ₃ H ₃	77
Figure 3.37 The partial density of states for MgTiO ₃ H ₃	77
Figure 3.38 The band structure for CaTiO ₃ H ₆	78
Figure 3.39 The partial density of states for CaTiO ₃ H ₃ , CaTiO ₃ H ₆ and CaTiO ₃ H ₈ ..	78
Figure 3.40: The electron-density distributions for CaTiO ₃ H ₃ (a) in (1 0 0) plane and (b) in (1 1 1) plane, for CaTiO ₃ H ₆ (c) in (1 0 0) plane and (d) in (1 1 1) plane, for CaTiO ₃ H ₈ (e) in (1 0 0) plane and (f) in (1 1 1) plane.....	79
Figure 3.41 The direction dependent (a) Young's modulus, (b) linear compressibility, (c) shear modulus, and (d) Poisson's ratio in 3D for CaTiO ₃ H ₆	81
Figure 4.1 The crystal structure of Ca ₃ XH	84
Figure 4.2 The crystal structures for Ca ₃ XH ₄ , Ca ₃ XH ₇ , Ca ₃ XH ₉ , and Ca ₃ XH ₁₀ compounds.....	85
Figure 4.3 X-ray diffraction patterns for Ca ₃ CH _x (X= 1, 4, 7, 9, 10).....	87
Figure 4.4 X-ray diffraction patterns for Ca ₃ NH _x (X= 1, 4, 7, 9, 10).....	87
Figure 4.5 The direction dependent (a) Young's modulus, (b) linear compressibility, (c) shear modulus, and (d) Poisson's ratio in 3D for Ca ₃ CH, Ca ₃ CH ₄ and Ca ₃ CH ₇ ..	90
Figure 4.6 The direction dependent (a) Young's modulus, (b) linear compressibility, (c) shear modulus, and (d) Poisson's ratio in 3D for Ca ₃ NH and Ca ₃ NH ₄	91
Figure 4.7 The thermal expansion, heat capacity at constant volume, entropy and free energy as a function of temperature at 0 GPa pressure for Ca ₃ CH _x	94
Figure 4.8 The thermal expansion, heat capacity at constant volume, entropy and free energy as a function of temperature at 0 GPa pressure for Ca ₃ NH _x	96
Figure 4.9 The band structure for Ca ₃ CH ₇	99

Figure 4.10 The partial density of states for Ca_3CH , Ca_3CH_4 and Ca_3CH_7	99
Figure 4.11 The partial density of states for Ca_3NH and Ca_3NH_4	100
Figure 4.12 The electron-density distributions for Ca_3CH , Ca_3CH_4 and Ca_3CH_7 ...	101
Figure 5.1 The crystal structure for XNiH_3	104
Figure 5.2 X-ray diffraction patterns for XNiH_3	105
Figure 5.3 The band structures and corresponding partial density of states for (a) LiNiH_3 , (b) NaNiH_3 and (c) KNiH_3	107
Figure 5.4 The electron-density distribution for LiNiH_3 along (1 0 0) direction for a $2 \times 2 \times 2$ supercell	108
Figure 5.5 The direction dependent (a) Young's modulus, (b) linear compressibility (c) shear modulus and (d) Poisson's ratio in 3D for XNiH_3	110
Figure 5.6 The phonon dispersion curves and corresponding phonon density of states for (a) LiNiH_3 , (b) NaNiH_3 and (c) KNiH_3	113
Figure 5.7 The free energy, enthalpy, entropy and heat capacity as a function of temperature for (a) LiNiH_3 , (b) NaNiH_3 and (c) KNiH_3	115

LIST OF ABBREVIATIONS

2D	2 Dimensional
3D	3 Dimensional
DFT	Density Functional Theory
DOE	Department of Energy
f. u.	Formula Unit
GC	Gamma centered
GGA	Generalized Gradient Approximation
LDA	Local Density Approximation
MP	Monkhorst-Pack
PAW	Projector Augmented Wave
PBE	Perdew-Burke-Ernzerhof
PCI	Pressure Composition Isotherm
PDOS	Partial Density of States
VASP	Vienna Ab-initio Simulation Package

CHAPTER 1

INTRODUCTION

The digital technologies and the electrical vehicles are an essential part of our daily life. Also, the increasingly use of cell phones and laptops requires to have long battery time for these devices that is the one of the most important consideration for a device choice. In addition to personnel electronic devices, it is important to have portable energy sources for military applications, leisure activities, educational purposes, etc. [1]. The current battery technology has some limitations such as higher energy densities, weight and flexibility [2]. However, the fuel cells are a promising candidate for providing higher energy densities. Also, the fuel cells provide clean and safe energy [2].

The batteries convert the chemical energy to electrical energy with the connection of the electrodes. The batteries are closed systems and they have a limitation on capacity due to the electrode volume [2]. The fuel cells are open systems and they combust a stored fuel with ambient oxygen [2]. For the fuel cells, the stored energy is related to the amount of stored fuel. There are fuel cells that use methanol, ethanol, etc. Moreover, the fuel cells that use hydrogen as the fuel get attention because of the anode kinetics and clean product of water [2].

The hydrogen fuel cells generate low voltage and high current and also the generated electricity do not depend on the fuel level [2]. The clean product of water could be released as a water vapor. These fuel cells could be designed as rechargeable or disposable fuel systems [2]. But, the necessary high volumetric and gravimetric densities of hydrogen fuel are the most important considerations. The aim of this thesis is to study the perovskite materials for hydrogen storage that could be a powerful

candidate as a hydrogen fuel material due having stability with ceramic properties that are preferred properties for portable hydrogen power systems.

Hydrogen is the most abundant element in the Earth and it is the lightest element on the periodic table. In addition, hydrogen is an odorless, colorless, tasteless and non-poisonous gas. The energy content of hydrogen is higher on the mass basis but it has lower energy content on the volume basis. As an example, hydrogen has three times higher mass energy content while it has four times lower volume energy content than gasoline [3]. Moreover, hydrogen could be used to store the electricity generated from renewable energy sources [4]. These properties provide significant advantages to hydrogen as a possible future energy source and portable power equipment.

The energy policies involve a hydrogen economy that includes production of hydrogen, storage of hydrogen and usage of hydrogen [4]. If hydrogen produces using non-fossil fuels, only the water is produced. The most commonly used methods for hydrogen production are conventional and renewable technologies [5]. The conventional methods use fossil fuels to produce hydrogen that also contribute to the emission of greenhouse gases. The steam reforming is the most common process of the conventional methods. The renewable technologies use the renewable energy sources to produce hydrogen that is environmentally friendly and preferable technique to produce hydrogen. Among these techniques, the water splitting is the most considered method for the renewable technologies.

The produced hydrogen needs storage and the methods for the hydrogen storage could be classified into three: gas hydrogen storage, liquid hydrogen storage and solid state hydrogen storage [6–10]. Hydrogen is a gas at ambient conditions and so, the high pressure vessels are necessary for the gas hydrogen storage method [6]. However, the safety is an important issue for this method. The liquid hydrogen storage method requires extra energy to liquefy hydrogen. Moreover, the boiling of hydrogen is another issue that must be considered. Solid state hydrogen storage methods include physisorption of hydrogen and chemisorption of hydrogen [10]. The hydrogen atoms

physically bound on a high surface area material for the physisorption of hydrogen while the hydrogen atoms have bonds with the materials for the chemisorption of hydrogen [10]. For the physisorption of hydrogen, a low temperature is required to have a significant amount of hydrogen stored due to the low van der Waals force between hydrogen atoms and the surface [11]. However, high temperatures are necessary for the chemisorption of hydrogen in order to break the chemical bonds to release the stored hydrogen [12]. Therefore, the storage methods should satisfy some necessary conditions such as reversible storage for several times, hydrogen store and release at ambient conditions, sufficient gravimetric and volumetric storage capacities, etc. [13].

The US Department of Energy (DOE) sets targets for portable hydrogen power equipment [14]. The followings are some of these targets for 2020 [14]:

- The gravimetric hydrogen storage capacity should be 4.0 wt.% for single used portable power equipment and 3.0 wt.% for rechargeable power equipment.
- The volumetric hydrogen storage capacity should be 0.04 kg H₂/L system for single used portable power equipment and 0.03 kg H₂/L system for rechargeable power equipment.
- The operating ambient temperature should be between -40 °C and 60 °C.
- The minimum delivery pressure and the maximum delivery pressure should be 1.5 bar and 3.0 bar, respectively.
- The cost should be 1 \$/g H₂ stored for single used portable power equipment and 13 \$/g H₂ stored for rechargeable power equipment.

These targets should be satisfied for a portable power equipment but any method has not satisfied all these requirements at the same time up to date. Among the hydrogen storage methods, both gas and liquid ones have drawbacks of low storage capacities to meet these targets. However, the solid state hydrogen storage method provides to get significant storage capacities and to be considered a possible solution for portable energy sources.

Solid state hydrogen storage is mostly studied for metal hydrides, complex hydrides, carbon structures and metal organic frameworks [15–18]. For the carbon structures and the metal organic frameworks, it is important to have large pore size to store more hydrogen. For the metal hydrides, magnesium gets considerable attention due to its low weight and low cost [18]. However, magnesium hydrides have low hydrogen desorption kinetics and high reactivity to air and oxygen [18]. Another material group is the complex hydrides that are composed of hydrogen and group IA, group IIA and group IIIA elements on the periodic table [17]. The mostly studied complex hydrides are alanates, amides, imides and borohydrides [18]. But, the complex hydrides do not have reversible storage capacities that is the biggest problem for hydrogen storage applications.

Another promising material group for hydrogen storage is the perovskite type hydrides. The perovskite type hydrides having ABH_3 formula generally composed of group IA and group IIA elements and hydrogen on the periodic table [19] and these compounds have high gravimetric storage capacities. Hence, the perovskite type hydrides get great interest and there are several studies for these compounds both theoretically and experimentally in the literature [19–28].

There is a request for a material that satisfy the US DOE targets for hydrogen storage. So, within this thesis, the perovskite materials have been investigated for hydrogen storage using theoretical calculation, Density Functional Theory (DFT). In recent years, the theoretical studies are a part of experimental studies. Because, these theoretical studies do not need any large infrastructures and also the results could lead to experimental studies. For this purpose, the chosen perovskite materials have been doped with hydrogen atoms and the main physical properties (structural, electronic, mechanic, vibrational and thermal properties) have been investigated.

Chapter 2 presents the theoretical background for this thesis where DFT has been briefly detailed. In addition, the required formulas and definitions have been reported and the perovskite materials have been detailed in this section. In Chapter 3, the

hydrogen storage studies for perovskite materials have been presented. $BaXO_3$ ($X=$ Sc or Y) and $XTiO_3$ ($X=$ Mg or Ca) have been studied for this purpose. All structures have been studied using Vienna Ab-initio Simulation Package (VASP) [29], [30] and have been investigated for their structural, mechanic, electronic and vibrational properties. Furthermore, the hydrogen doping has been performed and the hydrogen doped structures have been examined to detailed the properties of them. Another material group, the anti-perovskite compounds Ca_3XH ($X=$ C or N) have been presented in Chapter 4 and the hydrogen doping studies have been performed that are also detailed in this chapter. Chapter 5 presents the studies for perovskite type hydrides $XNiH_3$ ($X=$ Li, Na or K). These hydrides have been optimized and their structural, mechanic, electronic and vibrational properties have been studied as well as their hydrogen storage properties. The last chapter gives a brief conclusion.

CHAPTER 2

THEORETICAL BACKGROUND

The theoretical calculations are crucial that provide to simulate the materials in extreme conditions. These theoretical studies could save time and resources and the experiments could be designed with the obtained results. Density Functional Theory (DFT) is an elegant theory that does not depend on any experimental results. In addition, DFT calculations give consistent results with the experimental results. DFT calculations have been applied to physics, chemistry and material science. In this thesis, DFT calculations have been performed using the Vienna Ab-initio Simulation Package (VASP) [29–30]. In this chapter, the necessary theoretically background of DFT has been presented. Also, the required definitions for the calculations of the main physical properties of materials have been detailed. Furthermore, the properties of the perovskite materials have been given in this chapter. DFT has been studied for several decades where several books and reviews could be found in the literature and in this chapter, the mainly used sources are References [31–39].

2.1. Density Functional Theory

The nature of the atoms and subatomic particles have been investigated in detail with the foundations of the quantum mechanics. The Schrödinger equation given in Equation 2.1, has been calculated to find the ground state wavefunction of a system that could be used to obtain an observable for a system. The solution of the Schrödinger equation is rather easy for H atom, while it is not an easy task for many body systems.

$$H(\vec{r}_i, \vec{R}_I)\Psi(\vec{r}_1, \vec{r}_2, \dots, \vec{r}_N) = E \Psi(\vec{r}_1, \vec{r}_2, \dots, \vec{r}_N) \quad (2.1)$$

In Equation 2.1, H is the Hamiltonian for the many electron system, Ψ is the ground state wavefunction and E is the ground state energy. The Hamiltonian is given in Equation 2.2 where r_i and m_e are the positions and the mass of the electrons and R_I and M_I are the positions and the mass of the nuclei.

$$H(\vec{r}_i, \vec{R}_I) = \frac{-\hbar^2}{2m_e} \sum_i \nabla_i^2 + \sum_{i,I} \frac{Z_I e^2}{|r_i - R_I|} + \frac{1}{2} \sum_{i \neq j} \frac{e^2}{|r_i - r_j|} - \sum_I \frac{\hbar^2}{2M_I} \nabla_I^2 + \frac{1}{2} \sum_{I \neq J} \frac{Z_I Z_J e^2}{|R_I - R_J|} \quad (2.2)$$

In Equation 2.2, the first term corresponds to the kinetic energy of the electrons, the second term corresponds to the electron-nuclei interaction energy, the third term corresponds to the electron-electron interaction energy, the fourth term corresponds to the kinetic energy of the nuclei and the last term corresponds to the nuclei-nuclei interaction energy. However, the electron-electron interaction energy is hard to calculate. At this point, some approximations could be made to solve this Hamiltonian. The first approximation was proposed by Born and Oppenheimer called Born-Oppenheimer approximation [40] that separate the motions of the nuclei and the electrons and take the nuclei as stationary compared to the electrons. The nuclei are more heavy than electron and the kinetic energy of the nuclei can be neglected in Equation 2.2. The nuclei-nuclei interaction energy could be taken as a constant that behaves like an external potential.

With the Born-Oppenheimer approximation, the Hamiltonian describes the system with the effect of the nuclei to the electrons as a fixed external potential. This external potential could also include an external electric or magnetic field. Also, the nuclei-nuclei interaction is a constant and could be added as a constant to external potential.

So, if the number of electrons and the external potential are known, the many-body Hamiltonian could be solved in principle.

Another simplification could be done taking the electrons as non-interacting particles. Hartree made an approximation and the Schrödinger equation could be solved for the single particle states [37]. The electrons interact with the average electron density in the Hartree approximation that results the self-interaction of the electrons. Then, Hartree-Fock approximation takes into account the fermionic nature of the electrons and the wavefunction of a many body system could be found with a single Slater determinant that minimizes the ground state energy [37]. Hartree-Fock approximation takes into account the exchange property of electrons and the self-interaction of the electrons has been cancelled with the exchange of the electrons.

The stated approximations could not have the potential to fully describe the many body systems. The electrons have both the exchange and correlation properties. When the two electrons change their positions, the interaction energy between these electrons changes that is the exchange property. Also, the motion of every other electron in the system affects each electron that is the correlation property. The revolution and the discovery of DFT come with the two papers written by Hohenberg-Kohn [41] and Kohn-Sham [42] that take into account the total electron density to solve the Schrödinger equation like Kohn-Sham equations.

The density ($n(\vec{r})$) of a many-body system is an observable and could be found with the expectation value of the single particle density operator for the many body wavefunction using Equation 2.4. The density operator is the probability of finding a particle at a position in space such as \vec{r}_i as given in Equation 2.3.

$$n(\vec{r}) = \sum_{i=1,N} \delta(\vec{r} - \vec{r}_i) \quad (2.3)$$

$$\begin{aligned}
n(\vec{r}) &= \langle \Psi | n(\vec{r}) | \Psi \rangle = \sum_{i=1, N} \int \delta(\vec{r} - \vec{r}_i) |\Psi(\vec{r}_1, \vec{r}_2, \dots, \vec{r}_N)|^2 d\vec{r}_1 \dots d\vec{r}_N \\
&= N \int |\Psi(\vec{r}, \vec{r}_2, \dots, \vec{r}_N)|^2 d\vec{r}_2 \dots d\vec{r}_N
\end{aligned} \tag{2.4}$$

If the wavefunction is normalized, the expectation value of the density operator over all space gives the total number of electrons N .

The density is more useful that depends on 3 degrees of freedom while the wavefunctions of many body system depend on $3N$ degrees of freedom. The statements made by Hohenberg and Kohn [41] are:

- The external potential that acting on a many body system could be determined with the ground state density.
- The ground state electron density gives the minimum ground state energy that is a functional of the ground state density.

To prove the first statement, two external potentials $V_{ext}^{(1)}(\vec{r})$ and $V_{ext}^{(2)}(\vec{r})$ should be considered that give the same ground state density. These external potentials belong to two Hamiltonians as $H^{(1)}(\vec{r})$ and $H^{(2)}(\vec{r})$ that give two wavefunctions $\Psi^{(1)}(\vec{r})$ and $\Psi^{(2)}(\vec{r})$. For $H^{(1)}(\vec{r})$, the ground state energy could be obtained with $\Psi^{(1)}(\vec{r})$:

$$E^{(1)} = \langle \Psi^{(1)} | H^{(1)} | \Psi^{(1)} \rangle < \langle \Psi^{(2)} | H^{(1)} | \Psi^{(2)} \rangle \tag{2.5}$$

We assume that the ground state is non-degenerate and the last term could be written as follows:

$$\langle \Psi^{(2)} | H^{(1)} | \Psi^{(2)} \rangle = \langle \Psi^{(2)} | H^{(2)} | \Psi^{(2)} \rangle + \langle \Psi^{(2)} | H^{(1)} - H^{(2)} | \Psi^{(2)} \rangle$$

$$= E^{(2)} + \int d^3r [V_{ext}^{(1)}(\vec{r}) - V_{ext}^{(2)}(\vec{r})]n(\vec{r}) \quad (2.6)$$

Now, we have

$$E^{(1)} < E^{(2)} + \int d^3r [V_{ext}^{(1)}(\vec{r}) - V_{ext}^{(2)}(\vec{r})]n(\vec{r}) \quad (2.7)$$

If we consider $E^{(2)}$ with the same approach, we will find

$$E^{(2)} < E^{(1)} + \int d^3r [V_{ext}^{(2)}(\vec{r}) - V_{ext}^{(1)}(\vec{r})]n(\vec{r}) \quad (2.8)$$

If we add Equation 2.7 and Equation 2.8, we will come up with a contradictory inequality. So, the first statement has been proved and two different external potentials that differ more than a constant cannot give the same ground state density. However, we still need to solve the many-body problem in the effect of an external potential.

The second statement could be proved considering $n(\vec{r})$ as the ground state density with an external potential V_{ext} . If $n(\vec{r})$ is known, the properties such as kinetic energy could be determined as considering the functional of density. The total energy functional is given in Equation 2.9.

$$\begin{aligned} E[n] &= T[n] + E_{int}[n] + \int d^3r V_{ext}(\vec{r})n(\vec{r}) + E_N \\ &= F[n] + \int d^3r V_{ext}(\vec{r})n(\vec{r}) + E_N \end{aligned} \quad (2.9)$$

In Equation 2.9, E_N is the interaction energy of the nuclei and $F[n]$ includes the kinetic and potential energies for the electrons in the system. The ground state density $n^{(1)}(\vec{r})$ determines the ground state energy.

$$E^{(1)} = E[n^{(1)}] = \langle \Psi^{(1)} | H^{(1)} | \Psi^{(1)} \rangle \quad (2.10)$$

Another density $n^{(2)}(\vec{r})$ gives a higher energy than $E^{(1)}$.

$$E^{(1)} = E[n^{(1)}] = \langle \Psi^{(1)} | H^{(1)} | \Psi^{(1)} \rangle < \langle \Psi^{(2)} | H^{(1)} | \Psi^{(2)} \rangle = E^{(2)} \quad (2.11)$$

So, the total energy of the system could be written as a functional of $n(\vec{r})$ and the minimization with respect to $n(\vec{r})$ gives the ground state energy.

Kohn and Sham [42] proposed a method to solve this interacting particle systems. They take the system as non-interacting particles and add the interaction terms as an exchange-correlation functional of the density. The obtained ground state density and the ground state energy depend on the accuracy of the exchange-correlation functional. The independent particle Hamiltonian includes the kinetic energy operator for the independent particle ($T_s[n]$) and the external potential and similar to Hohenberg-Kohn expression, the ground state energy functional could be written as

$$E_{KS} = T_s[n] + \int d^3r V_{\text{ext}}(\vec{r})n(\vec{r}) + E_{\text{Hartree}}[n] + E_N + E_{xc}[n] \quad (2.12)$$

$$E_{\text{Hartree}}[n] = \frac{1}{2} \int d^3 r \int d^3 r' \frac{n(\vec{r})n(\vec{r}')}{|\vec{r}-\vec{r}'|} \quad (2.13)$$

In Equation 2.12, $V_{\text{ext}}(\vec{r})$ is the external potential due to the nuclei and any other electric or magnetic field, $E_{\text{Hartree}}[n]$ is the classical Coulomb interaction for the electron density given in Equation 2.13 and E_N is the interaction energy between nuclei. Also, Equation 2.12 includes the many body effect of exchange and correlation as the exchange-correlation energy ($E_{\text{xc}}[n]$). Here, if we compare Equation 2.9 and Equation 2.12, the E_{xc} is the difference of the kinetic and the internal interaction energies for the true interacting many body systems from the independent particle system with electron-electron interactions replaced with Hartree energy. If E_{xc} is known explicitly, the exact ground state energy could be determined with the Kohn-Sham equations for the independent particles. So, after these statements, DFT became a promising tool in physics, chemistry and materials science.

2.1.1. Functionals for Exchange and Correlation

The exchange-correlation functional is a useful consideration in the DFT. Despite E_{xc} is very complex, approaches have been performed to define it. One approach for the exchange-correlation functional is the Local Density Approximation (LDA) [36] that accounts the exchange-correlation energy as simply an integral over all space with the same exchange-correlation energy density ($\epsilon_{\text{xc}}^{\text{hom}}(n(\vec{r}))$) as given in Equation 2.14.

$$E_{\text{xc}}^{\text{LDA}} = \int d^3 r n(\vec{r}) \epsilon_{\text{xc}}^{\text{hom}}(n(\vec{r})) \quad (2.14)$$

LDA takes the density as a constant but in some cases this approximation is not valid and the variation of the density should be included. So, another approach for the exchange-correlation functional is called Generalized Gradient Approximation

(GGA) [36] that depends on the gradient of the density ($f(n(\vec{r}), \nabla(n(\vec{r})))$) as given in Equation 2.15.

$$E_{xc}^{GGA} = \int d^3r f(n(\vec{r}), \nabla(n(\vec{r}))) \quad (2.15)$$

There are different GGA methods that take different $f(n(\vec{r}), \nabla(n(\vec{r})))$ such as Perdew-Wang (PW91) [43], Perdew-Burke-Ernzerhof (PBE) [44], etc. The GGA with Perdew-Burke-Ernzerhof (PBE) functional has been employed for the exchange-correlation calculations within this thesis.

LDA and GGA are the mostly used approximations for the exchange-correlation functional. Another approach is LDA+U or GGA+U approach that based on LDA or GGA type functional with an additional orbital dependent interaction parameter. The interaction parameter is essential for highly localized orbitals as d and f orbitals. The U parameter gives better results than LDA or GGA.

Another functional used in DFT calculations is called hybrid functional. The hybrid functionals are composed of a density functional and orbital dependent Hartree-Fock term. The hybrid functionals could predict better excitation energies than LDA or GGA. The one of the most used hybrid functional is B3LYP [45].

2.1.2. Pseudopotentials

DFT calculations take into account the nuclei and the full electron interactions. However, to reduce the complexity of the problem, the pseudopotential approach has been used that considers an effective potential acting on the valence electrons and

ignore the strong Coulomb interaction with the nuclei and the effects of the core electrons. The pseudopotential approach does not reduce the accuracy of the DFT calculations because the contributions from the core electrons to the energy of a material is minor and the major contribution comes from the valence electrons. The pseudopotential approach is based on the fact that the scattering of the electrons from the nuclei could be resembled with the weak potential of the valence electrons. Also, the nuclei exert an attractive force to the valence electrons and the wavefunction of the valence electrons must be orthogonal to the wavefunction of the nuclei. Figure 2.1 shows the pseudopotential and the pseudo-wavefunction of a system that beyond a cut off radius (r_c), the wavefunction and the potential are not affected.

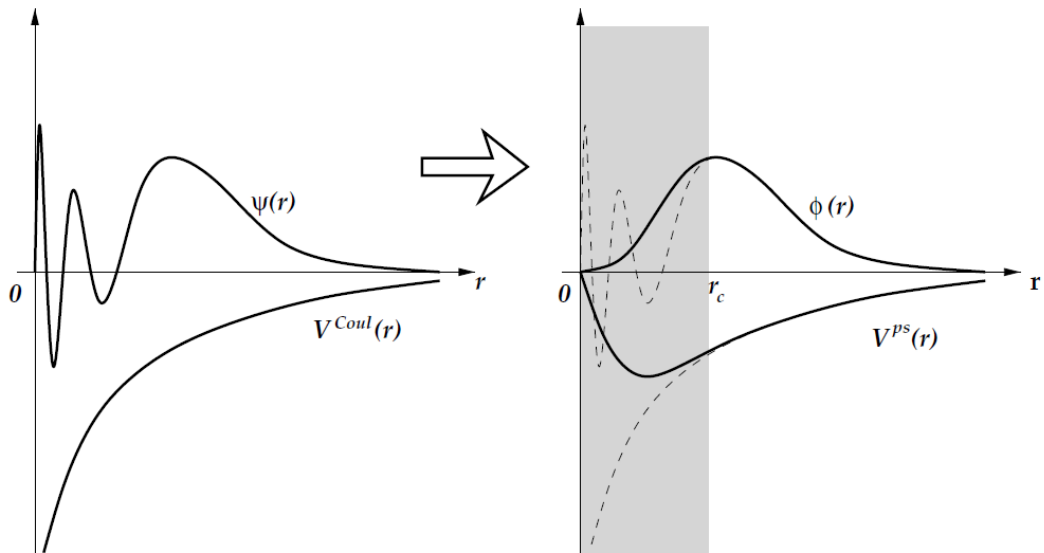


Figure 2.1 The Coulomb potential and the wavefunction of a system and the pseudopotential and corresponding pseudo-wavefunction [37]

The pseudopotential methods such as norm conserving [46], ultra-soft [47] and projector augmented wave (PAW) [48], etc. have been employed for DFT calculations. The norm conserving pseudopotentials are normalized and they generate the same properties with all electron calculations. The wavefunction of the norm conserving pseudopotential has the same norm with the wavefunction of all electron

calculations inside a cut off radius and outside the cut off radius, the wavefunction of the norm conserving pseudopotential is same with the wavefunction of all electrons. However, the norm conserving pseudopotentials are not so smooth and another pseudopotential approach is the ultra-soft pseudopotentials having smooth functions. The ultra-soft pseudopotentials also give accurate results. Also, the ultra-soft pseudopotentials have lower cutoff energy. Furthermore, the PAW method has lower cutoff radius than ultra-soft pseudopotentials. The wavefunctions near the core region has an oscillating nature due to the strong Coulomb interaction. So, the PAW method approximate these oscillating wavefunctions to smooth wavefunctions. The PAW method has been used for the electron-ion interaction calculations within this thesis.

The DFT calculations are self-consistent calculations. First, the prediction of the ground state electron density is made. Then, the effective potential that depends on the density is obtained. The Kohn-Sham equations is solved with this density and the ground state energy and the ground state density are obtained. If the initial guess and the obtained density are consistent, the calculations are finished. If the initial guess and the obtained density are not consistent, another guess is made and the previous steps are performed.

2.2. Crystal Systems

A crystal is formed by arranging atoms in a periodic system. So, the crystal is invariant under translation that provides periodic physical properties. There are seven crystal systems that formed according to the lattice vectors a , b , c and the angle between these vectors α , β , γ namely cubic, trigonal, hexagonal, tetragonal, orthorhombic, monoclinic, triclinic [49] and the relation between the lattice vectors and the angles for these systems are presented in Table 2.1. These crystal systems form 230 space groups according to the symmetry of the systems [49]. The crystal structure of a material could be found with the experimental studies in the literature and also some

web sites like Bilbao Crystallographic Server [50], Materials Project [51], etc. The studied perovskite materials within this thesis could crystallize in five possible crystal phases: cubic (Pm-3m), tetragonal (P4mm), hexagonal (P-3m1), rhombohedral (R-3c) and orthorhombic (Pbnm) [52] and the studied structures have been obtained from literature [52]. Also, the visualization of the crystals have been obtained by using VESTA software [53].

Table 2.1 Seven crystal systems and the relations between the lattice vectors and the lattice angles

Crystal system	Lattice vectors	Lattice angles
Triclinic	$a \neq b \neq c$	$\alpha \neq \beta \neq \gamma$
Monoclinic	$a \neq b \neq c$	$\alpha = \gamma = 90^\circ \neq \beta$
Orthorhombic	$a \neq b \neq c$	$\alpha = \beta = \gamma = 90^\circ$
Tetragonal	$a = b \neq c$	$\alpha = \beta = \gamma = 90^\circ$
Cubic	$a = b = c$	$\alpha = \beta = \gamma = 90^\circ$
Trigonal	$a = b = c$	$\alpha = \beta = \gamma < 120^\circ, \neq 90^\circ$
Hexagonal	$a = b \neq c$	$\alpha = \beta = 90^\circ, \gamma = 120^\circ$

The formation energies have been calculated for the studied compounds to determine their energetic stability and to decide their synthesizability using Equation 2.16 where $E_{Total}^{ABX_3}$ is the total energy for ABX_3 compound and E_{Solid}^A , E_{Solid}^B and E_{Solid}^X are the ground states energies for A, B and X atoms. If the calculated formation energy is negative, this compound is energetically stable and also synthesizable.

$$\Delta E_{For}(ABX_3) = E_{Total}^{ABX_3} - E_{Solid}^A - E_{Solid}^B - 3 \cdot E_{Solid}^X \quad (2.16)$$

2.3. Band Theory

The energy of the electrons has considered to reveal the properties of the solids. For this purpose, the free electron model studied to determine the energy of each electron in the atoms. This model considers electrons as non-interacting particles and neglect the exchange and correlation property. This model is successful for the metals but it does not explain magnetism, superconductivity, optical and electronic properties of semiconductors.

Then, a more successful model should be considered to overcome the explanation of these properties. The electrons could be considered in a periodic potential as given in Equation 2.17 that results from the nuclei and the other electrons.

$$V(\vec{r}) = V(\vec{r} + \vec{r}_n) \text{ where } \vec{r}_n = n_1\vec{a} + n_2\vec{b} + n_3\vec{c} \quad (2.17)$$

In Equation 2.17, \vec{r}_n is the arbitrary translation vector with n_1, n_2, n_3 are integers and $\vec{a}, \vec{b}, \vec{c}$ are lattice vectors. The Schrödinger equation with the periodic potential yields the wavefunctions as plane waves:

$$\Psi_k(\vec{r}) = u_k(\vec{r})e^{i\vec{k}\cdot\vec{r}} \text{ with } u_k(\vec{r}) = u_k(\vec{r} + \vec{r}_n) \quad (2.18)$$

This periodic potential and the plane wave solution are known as the Bloch's theorem and the states are called the Bloch states of electrons. This periodicity could also be obtained with the consideration of the reciprocal lattice. The periodic potential results in the same energy eigenvalues for a Bloch state that differ by a reciprocal lattice vector \vec{G} :

$$E(\vec{k}) = E(\vec{k} + \vec{G}) \quad (2.19)$$

These energy values form energy bands called electronic band structure of a solid. For the electronic band structure, it is sufficient to know \vec{k} values and consider only the first Brillouin zone. The band structure has discrete energy levels and when the atoms come together to form the solid, the potentials of the other atoms also affect and the width of the band increases as shown in Figure 2.2. In addition, each energy level could occupy two electrons due to their spin degree of freedom and the occupation of the electrons starts from the lowest lying state.

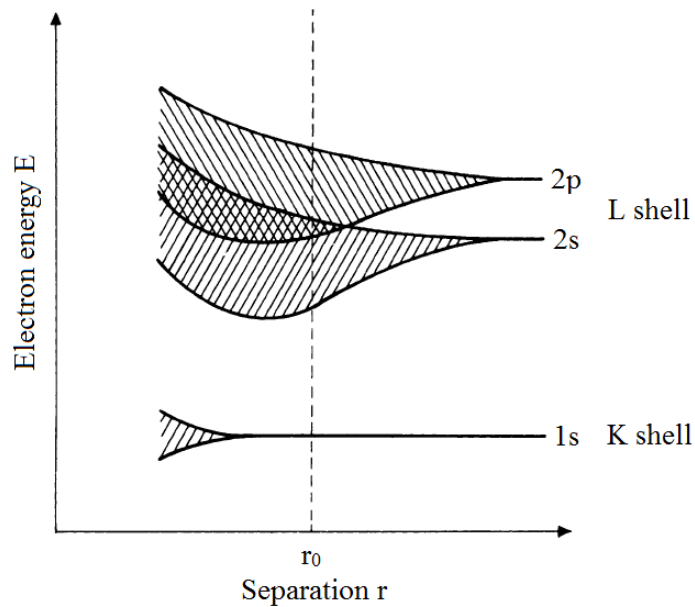


Figure 2.2 The energy levels of electrons when atoms come closer [54]

The bands are filled with the electrons and some bands are empty. The energy difference between the highest occupied level and the lowest unoccupied level is known as band gap. If the band gap is large, the material is called insulator. For semiconductors, the band gap is lower than that of insulators and the electrons could move from occupied bands to unoccupied bands. For the semiconductors, the

occupied bands are called valence bands and the unoccupied bands are called the conduction bands. For metals, there is no gap between the occupied bands and unoccupied bands. Thus, the electrons could move from occupied bands to unoccupied bands that results the electrical conductivity of the metals. The Fermi level is defined as the level that is between the occupied bands and unoccupied bands.

Another representation of the band structure is the density of states (DOS). The DOS is the number of electrons with a dE energy value as:

$$dZ = \frac{V}{(2\pi)^3} \int_E^{E+dE} d\vec{k} \quad (2.20)$$

The band structure of the solids could provide the information of electrical resistivity, optical properties, etc. The several methods have been employed for the calculation of the band structures of the solids such as plane wave method, linear augmented plane wave method, tight binding method, etc. The VASP employs the plane wave method for the band structure calculations and the calculated band structures presented in the subsequent chapters have been obtained with this method.

In addition to band structure and the DOS calculations, the Bader partial charge analysis has been performed within this thesis. The determination of the partial charges of the atoms provide to obtain the charge transfer between the atoms and their bonding contributions. The Bader partial charge analysis based on Richard Bader's Atoms in Molecules [55] definition has been employed within this thesis. The method is based on the surfaces that has zero flux. This zero flux surface is the separation point between the atoms. The charge within this surfaces is the charge of the atom. The analysis of the Bader charge calculation has been performed with the algorithm

developed by Henkelman et. al. [56]. If the calculated Bader net charge is negative, the charge is transferred to the atom, while if it is positive, the charge is transferred away from the atom. In addition to the Bader partial charge method, there are several other methods such as Mulliken population analysis [57], Hirshfeld charges [58] etc. However, VASP is compatible with the Bader partial charge calculation and this method has been employed within this thesis.

2.4. Mechanical Properties

The mechanical properties of solids determine their usage in technological applications. DFT calculations provide to obtain the single crystal properties. At this point, the relation between the single crystal properties and the polycrystalline properties should be made. The single crystal properties could be calculated using two methods: volume conserving method [59] and stress-strain method [60]. The stress-strain method has been employed to the calculations in this thesis that converges faster than the volume conserving method.

A stress (σ_i) is defined as the force per unit area with units of pressure and a strain (ε_i) is defined as the amount of change when a distortion applied with respect to the reference configuration and it is unitless. There is a relation between the stress and strain as given in Equation 2.21.

$$\sigma_i = \sum_{j=1,6} C_{ij} \varepsilon_j \quad (2.21)$$

The constants C_{ij} are called elastic constants. The elastic constants C_{ij} form a 6x6 matrix but C_{ij} equals to C_{ji} and reduce 21 independent elastic constants. According to the symmetry of the crystal, these 21 constants could be reduced more. These elastic

constants should satisfy the well-known Born stability criteria [61–63] for a mechanically stable compound. Table 2.2 lists the Born stability criteria for the crystal phases that are the possible crystal phases of the studied perovskite materials in this thesis.

Table 2.2 The Born stability criteria for the possible crystal phases of the perovskite materials

Crystal phase	Born stability criteria
Orthorhombic	$C_{ii} > 0 \ (i=1, \dots, 6)$ $C_{11} + C_{22} - 2C_{12} > 0$ $C_{11} + C_{33} - 2C_{13} > 0$ $C_{22} + C_{33} - 2C_{23} > 0$ $[C_{11} + C_{22} + C_{33} + 2(C_{12} + C_{13} + C_{23})] > 0$
Tetragonal	$C_{ii} > 0 \ (i=1, 3, 4, 6)$ $C_{11} - C_{12} > 0$ $C_{11} - 2C_{13} + C_{33} > 0$ $2C_{11} + 2C_{12} + 4C_{13} + C_{33} > 0$
Rhombohedral and Hexagonal	$C_{11} > 0$ $C_{11} - C_{12} > 0$ $C_{44} > 0$ $(C_{11} + C_{12}) C_{33} - 2C_{12}^2 > 0$
Cubic	$C_{11} > 0$ $C_{12} > 0$ $C_{44} > 0$ $C_{12} > C_{44}$ $C_{11} + 2C_{12} > 0$ $C_{11} - C_{12} > 0$

The polycrystalline properties as the bulk modulus (B) and the shear modulus (G) could be obtained using these elastic constants. The bulk modulus is the resistance to change when a hydrostatic pressure is applied to the material. The bulk modulus is related to the stiffness of a material. The shear modulus also called modulus of rigidity is the ratio of the shear stress to the shear strain. The Voigt approach [64] gives the upper bound for these moduli while the Reuss approach [65] gives the lower bound. The V and R subscripts correspond to the calculations with the Voigt and Reuss approaches in the following equations.

The bulk and shear modulus of the orthorhombic phase are as follows:

$$B_V = \frac{C_{11} + C_{22} + C_{33} + 2C_{12} + C_{13} + C_{23}}{9} \quad (2.22)$$

$$G_V = \frac{C_{11} + C_{22} + C_{33} + 3C_{44} + C_{55} + C_{66} - C_{12} + C_{13} + C_{23}}{15} \quad (2.23)$$

$$a = C_{11} C_{22} + C_{33} - 2C_{23} + C_{22} C_{33} - 2C_{13} - 2C_{33} C_{12} \quad (2.24)$$

$$b = C_{12} 2C_{23} - C_{12} + C_{13} 2C_{12} - C_{13} + C_{23} 2C_{13} - C_{23} \quad (2.25)$$

$$c = C_{11} C_{22} + C_{33} + C_{23} + C_{22} C_{33} + C_{13} + C_{33} C_{12} \quad (2.26)$$

$$d = C_{12} C_{23} + C_{12} - C_{13} C_{12} + C_{13} - C_{23} C_{13} + C_{23} \quad (2.27)$$

$$\Delta = C_{13} C_{12} C_{23} - C_{13} C_{22} + C_{23} C_{12} C_{13} - C_{23} C_{11} + C_{33} C_{11} C_{22} - C_{12}^2 \quad (2.28)$$

$$B_R = \frac{\Delta}{a+b} \quad (2.29)$$

$$G_R = 15 \left\{ 4 \frac{c-d}{\Delta} + 3 \left[\frac{1}{C_{44}} + \frac{1}{C_{55}} + \frac{1}{C_{66}} \right] \right\}^{-1} \quad (2.30)$$

The bulk and shear moduli of the tetragonal phase are as follows:

$$B_V = \frac{2C_{11} + C_{12} + C_{33} + 4C_{13}}{9} \quad (2.31)$$

$$G_V = \frac{4C_{11} - 2C_{12} + 2C_{33} - 4C_{13} + 12C_{44} + 6C_{66}}{30} \quad (2.32)$$

$$B_R = \frac{C_{11} + C_{12} C_{33} - 2C_{13}^2}{C_{11} + C_{12} + 2C_{33} - 4C_{13}} \quad (2.33)$$

$$G_R = \frac{15}{\frac{18B_V}{C_{11} + C_{12} C_{23} - 2C_{13}^2} + \frac{6}{C_{11} - C_{12}} + \frac{6}{C_{44}} + \frac{3}{C_{66}}} \quad (2.34)$$

The bulk and shear moduli of the rhombohedral and hexagonal phases are as follows:

$$B_V = \frac{2C_{11} + C_{12} + 4C_{13} + C_{33}}{9} \quad (2.35)$$

$$G_V = \frac{C_{11} + C_{12} + 2C_{33} - 4C_{13} + 12C_{44} + 12C_{66}}{30} \quad (2.36)$$

$$B_R = \frac{C_{11} + C_{12} C_{33} - 2C_{13}^2}{C_{11} + C_{12} + 2C_{33} - 4C_{13}} \quad (2.37)$$

$$G_R = \frac{5 [C_{11} + C_{12} C_{33} - 2C_{13}^2 C_{44} C_{66}]}{6B_V C_{44} C_{66} + 2 C_{11} + C_{12} C_{33} - 2C_{13}^2 C_{44} + C_{66}} \quad (2.38)$$

The bulk and shear moduli of the cubic phase are as follows:

$$B_V = \frac{C_{11} + 2C_{12}}{3} \quad (2.39)$$

$$G_V = \frac{C_{11} - C_{12} + 3C_{44}}{5} \quad (2.40)$$

$$B_R = B_V \quad (2.41)$$

$$G_R = \frac{5C_{11} - C_{12}C_{44}}{4C_{44} + 3C_{11} - C_{12}} \quad (2.42)$$

The Hill approach [66] gives the average of these Voigt and Reuss bounds that is close to the experimental results. The B and G values could be obtained with the average of the above B_V , B_R and G_V , G_R values.

$$B = \frac{B_R + B_V}{2} \quad G = \frac{G_R + G_V}{2} \quad (2.43)$$

The G/B ratio also called Pugh's modulus and the B/G ratio could be useful to find out the bonding nature and the brittle or the ductile character of a material, respectively. If the G/B ratio has a value around 1.1, the dominant bonding type of the material is covalent [67]. Besides, the materials having dominantly ionic bonding have the G/B ratio around 0.6 [67]. For the B/G ratio, the critical value is 1.75. The ductile materials have the B/G ratio higher than 1.75 while the brittle materials have the B/G ratio lower than 1.75. The ductile materials are preferred for the portable hydrogen storage systems.

Using obtained B and G values, the other polycrystalline properties could be determined. The Young's modulus (E) is the ratio of the stress to strain when a force is applied that compress or extend the material. If the Young's modulus is high, the stiffness of a material is also high. The Young's modulus could be calculated using Equation 2.44 for all crystal structures.

$$E = \frac{9GB}{G+3B} \quad (2.44)$$

The Poisson's ratio (ν), another polycrystalline property, is defined as the measure of the expansion of perpendicular directions to the direction of compression or the measure of contraction of perpendicular directions to the direction of stretching. Equation 2.45 could be used to obtain the Poisson's ratio with obtained B and G values. Moreover, the Poisson's ratio could be applied for the determination of the bonding nature of a material. If the Poisson's ratio is around 0.1, this means that the material has covalent bonding and if it is 0.25, the material has ionic bonding.

$$\nu = \frac{1}{2} \left[\frac{(B - \frac{2}{3}G)}{(B + \frac{2}{3}G)} \right] \quad (2.45)$$

The elastic anisotropic factors (A) also called Zener anisotropic factors affect the physical properties of a material for a preferred direction and could result in dislocation or cracks [68]. The elastic anisotropic factors are defined with A_1 for (1 0 0) plane, A_2 for (0 1 0) plane and A_3 for (0 0 1) plane and could be calculated using the following equations [68]:

$$A_1 = \frac{4C_{44}}{C_{11} + C_{33} - 2C_{13}} \quad (2.46)$$

$$A_2 = \frac{4C_{55}}{C_{22} + C_{33} - 2C_{23}} \quad (2.47)$$

$$A_3 = \frac{4C_{66}}{C_{11} + C_{22} - 2C_{12}} \quad (2.48)$$

The cubic crystals have $A_1 = A_2 = A_3$ and the tetragonal crystals have $A_1 = A_2$ due to the symmetry of the crystals. The isotropic materials have the anisotropic factors that equal to one. The deviation from one for A_1 , A_2 and A_3 results in anisotropy for that material. Another consideration for the anisotropic factors is the anisotropic factors in compression and shear (A_B and A_G) [68] and the universal anisotropic factor (A^U) [69] that could be calculated with the following equations.

$$A_B = \frac{B_V - B_R}{B_V + B_R} \quad (2.49)$$

$$A_G = \frac{G_V - G_R}{G_V + G_R} \quad (2.50)$$

$$A^U = 5\frac{G_V}{G_R} + \frac{B_V}{B_R} - 6 \quad (2.51)$$

The anisotropic factors in compression and shear are the percentage factors and if they are equal to zero, the material is isotropic while if they are different than zero, the material is anisotropic. Same criterion is applied to the universal anisotropic index, so the universal anisotropic factors of the isotropic materials are zero. In addition to the determination of the anisotropy of a material, the visualization of the some mechanical properties could be useful to the determination of the anisotropy of that material in some crystal directions. The direction dependent Young's modulus, linear compressibility, shear modulus and Poisson's ratio have been studied and will be presented in the next chapters. The ELATE software [70] have been used for the visualization of these properties.

Another important parameter is Debye temperature (Θ_D) that is related to the heat capacity and melting temperature of the solids. The Debye temperature could be calculated using the elastic constants with the following equation [71]:

$$\Theta_D = \frac{\hbar}{k_B} \left[\frac{3n}{4\pi} \left(\frac{N_A \rho}{M} \right) \right]^{1/3} V_m \quad (2.52)$$

where \hbar is the Planck constant, k_B is the Boltzman constant, n is the number of atoms per formula unit, N_A is the Avogadro's number, ρ is the density, M is the mass per formula unit and V_m is the average wave velocity.

The wave velocities could be determined using following equations [71]:

$$V_l = \sqrt{\frac{3B+4G}{3\rho}} \quad (2.53)$$

$$V_t = \sqrt{\frac{G}{\rho}} \quad (2.54)$$

$$V_m = \left[\frac{1}{3} \left(\frac{2}{V_t^3} + \frac{1}{V_l^3} \right) \right]^{-1/3} \quad (2.55)$$

The thermal conductivity of a material should be considered that is related to the technological applications for that material. The empirical models have been used to determine the thermal conductivity of solid materials. In this thesis, two empirical models as Clarke model [72] and Cahill model [73] have been employed for the determination of the thermal conductivities of the studied compounds with the following equations [74]:

Clarke's model:

$$\lambda_{min} = 0.87 k_B M_a^{-3/2} E^{2/3} \rho^{1/6} \quad M_a = \left[\frac{M}{(n \cdot N_A)} \right] \quad (2.56)$$

Cahill's model:

$$\lambda_{min} = \frac{k_B}{2.48} n^{2/3} (V_l + 2V_t) \quad (2.57)$$

where M_a is the average mass per atom and n is the density of number of atoms per volume.

2.5. Vibrational Properties

The energy of solids could be studied in two different approach: one is the study of electrons in the solid as explained in Section 2.3 and the other is the vibrations of the atoms around their equilibrium positions. The lattice vibrations arise from the small movements of atoms in the solids that are called phonons. Similar to photons, a phonon could also be both a wave or a particle. The particle phonon arises from the quantization of the vibrations. If the temperature of the solid increases, the number of the phonons increases.

The best way to explain the phonons is the one dimensional problem. In this problem, the atomic bonds are considered as springs that bound the atoms each other. Then, the

problem is reduced to Hooke's law that is the result of the Taylor expansion of the potential and taking the first derivative of the potential vanishing at equilibrium position. Any change in position of an atom could result a force that is proportional to a force constant. The one dimensional problem consists of N atoms with mass M at r_n positions. If the only neighborhood interaction is considered, the force on nth atom is

$$F_n = C(r_{n+1} - r_n) + C(r_{n-1} - r_n) \quad (2.58)$$

The equation of motion is

$$M \frac{d^2 r_n}{dt^2} = C(r_{n+1} + r_{n-1} - 2r_n) \quad (2.59)$$

The solutions of Equation 2.59 has the form of $e^{-i\omega t}$ and $\frac{d^2 r_n}{dt^2}$ equals to $-\omega^2 r_n$. Then the equation of motion becomes

$$-M \omega^2 r_n = C(r_{n+1} + r_{n-1} - 2r_n) \quad (2.60)$$

Then r_n has the travelling wave solutions as

$$r_{n\pm 1} = r e^{\pm ika} \quad (2.61)$$

a is the distance between the atoms and k is the wave vector. With Equation 2.61, the equation of motion becomes

$$-M \omega^2 r e^{inka} = C r [e^{i(n+1)ka} + e^{i(n-1)ka} - 2e^{inka}] \quad (2.62)$$

Cancelling re^{inka} gives

$$M \omega^2 = -C [e^{ika} + e^{-ika} - 2] \quad (2.63)$$

Using the relation $2\cos ka = e^{ika} + e^{-ika}$, the dispersion relation is obtained as

$$\omega^2 = (2C/M)(1 - \cos ka) \quad (2.64)$$

or using another trigonometric identity it could be expressed as

$$\omega^2 = (4C/M)\sin^2\left(\frac{1}{2}ka\right) \text{ or } \omega = (4C/M)^{1/2} \left|\sin\left(\frac{1}{2}ka\right)\right| \quad (2.65)$$

Then one can draw ω versus k and obtain Figure 2.3. This figure is called phonon dispersion curve.

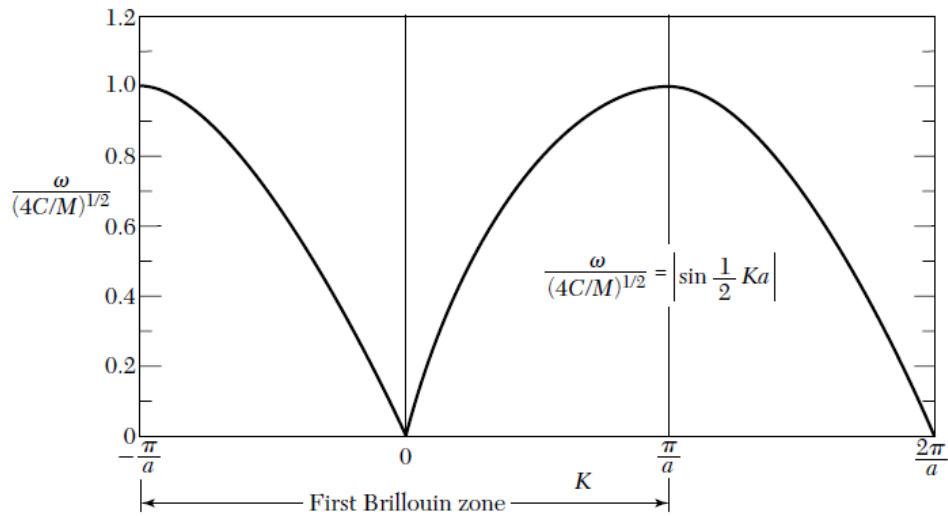


Figure 2.3 The plot of ω versus k [75]

The above consideration of one dimensional problem is a simplified version of the vibrational properties of solids. The solids have 3 degrees of freedom and therefore the resulting vibrations has $3N$ degrees for a solid containing N atoms. The vibrations are classified into two categories: acoustic and optical phonon branches. The number of the acoustic branches are three and the remaining $3N-3$ branches are the optical branches.

For the determination of the phonon frequencies, the force constants should be determined. For this purpose, the linear response method [76] and the finite displacement method [77] could be employed. The linear response method perturbs the solid and obtain the resultant frequencies. For the finite displacement method, one of the atoms is displaced and the resultant phonon frequencies could be obtained. The linear response method has been employed for the vibrational properties calculations within this thesis.

2.6. Hydrogen Storage Properties

Hydrogen storage properties of materials are important for the consideration in the hydrogen storage applications. There are several properties that could be considered such as gravimetric hydrogen storage capacity, hydrogen desorption temperature, cyclic stability, kinetics, hydrogen desorption pressure, etc. [13]. These properties could be determined with the experimental methods such as gas sorption measurements, temperature programmed methods, etc. and the theoretical modelling. In this thesis, the gravimetric hydrogen storage capacity and the hydrogen desorption temperature have been studied in detail. These properties could be determined with the bulk DFT studies of the solid materials.

The gravimetric hydrogen storage capacity is the amount of hydrogen stored per unit mass of a material that could be calculated using Equation 2.66 [13]. In Equation 2.66, H/M is the hydrogen to material atom ratio, M_H is the molar mass of hydrogen and M_{Host} is the molar mass of the material. As stated in Chapter 1, the US DOE target for the gravimetric storage capacity is 4.0 wt.% for single used portable power equipment and 3.0 wt.% for rechargeable power equipment. It should be noted that these capacity targets are for the whole equipment not only the capacity of the material.

$$C_{wt\%} = \left(\frac{\left(\frac{H}{M}\right)M_H}{M_{Host} + \left(\frac{H}{M}\right)M_H} \times 100 \right) \% \quad (2.66)$$

The hydrogen storage materials are characterized with the pressure composition isotherms (PCI) [78] as given in Figure 2.4. As the pressure increases the hydrogen atoms diffuses to material which correspond to the α phase in the figure. At a plateau pressure, there are two phases as the α phase and the β phase that is the hydride phase and with the increasing pressure, the α phase transforms to the β phase and similar to

the α phase region, the increasing of the pressure results in the increasing of H/M. The temperature is important for PCIs and different temperatures show different PCI as shown in the figure.

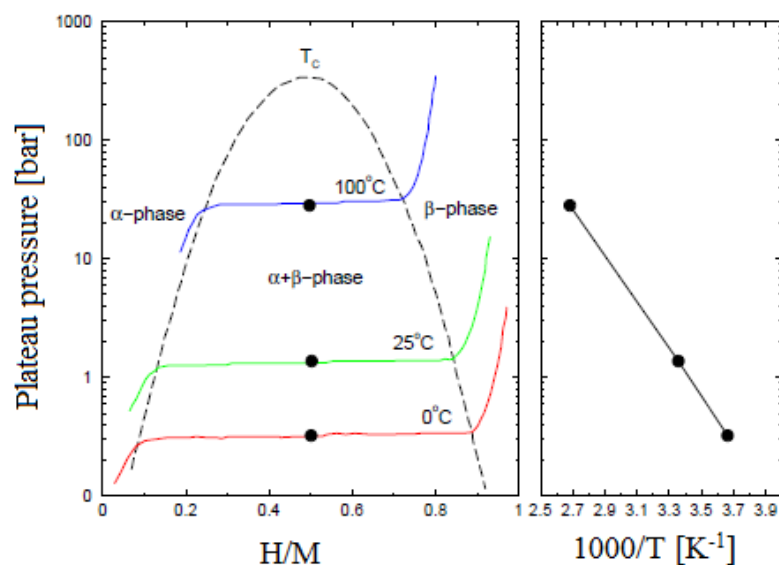


Figure 2.4 The pressure composition isotherm for a metal-hydride system and the right plot shows the Van't Hoff relation of this material [78]

The PCIs could be described with Equation 2.67 where P is the decomposition pressure, P_0 is equilibrium pressure, R is the universal gas constant, ΔH is the reaction enthalpy and ΔS is the change in entropy.

$$\ln \frac{P}{P_0} = \frac{\Delta H}{RT} - \frac{\Delta S}{R} \quad (2.67)$$

The right part of Figure 2.4 shows this relation given in Equation 2.67 also called Van't Hoff equation [13] where the slope gives $\Delta H/R$ and the intercept gives $\Delta S/R$. If the decomposition pressure is taken as 1 bar so the term $\ln P/P_0$ equals to zero which

results to the following equation:

$$\Delta H = T \times \Delta S \quad (2.68)$$

For the hydrogen storage materials, the entropy change mainly comes from the hydrogen atoms due to changing from solid phase to the gas phase. So, ΔS could be taken as 130.7 J/mol.K [79] that is the entropy change of hydrogen at 1 bar pressure. The hydrogen desorption temperature could be calculated with Equation 2.68 that is the required temperature to release the stored hydrogen at 1 bar pressure. As expressed in Chapter 1, the required operating temperature should be between -40 °C and 60 °C for portable power equipment. So, the hydrogen desorption temperatures should be at least close to the upper limit.

2.7. Perovskite Materials

The mineral CaTiO_3 discovered by German mineralogist Gustav Rose and it named as perovskite after Russian mineralogist Lev Perovski [80]. After then, the materials having the same crystal structure with CaTiO_3 are called perovskite materials [81]. In addition, there are abundant perovskite materials such as MgSiO_3 , FeSiO_3 , etc. in the Earth's crust [82]. The general chemical formula for the perovskite materials are ABX_3 where A and B are cations and X is an anion [83]. The ideal crystal structure of perovskite materials is cubic as shown in Figure 2.4. The A cation could be monovalent, divalent or trivalent metal ions while the B cation is a transition metal. The A cation is surrounded by 12 equidistant X anions while the B cation is surrounded by 6 X anions.

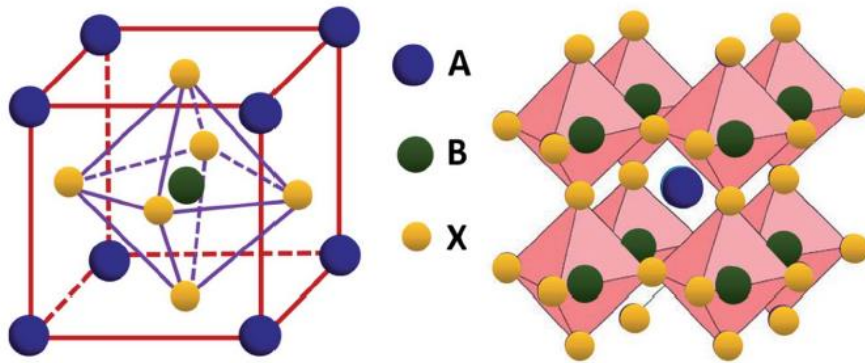


Figure 2.5 The ideal cubic crystal structure of perovskite materials [84]

The well-known cubic perovskite structures are SrTiO_3 , KTaO_3 , and BaTiO_3 [82]. The determination of the formation of perovskite compounds could be made using the Goldschmidt tolerance factor (t) as given in Equation 2.69 [84] where r_A , r_B and r_X are the atomic radii of A, B and X ions. The ideal cubic perovskite structure has a tolerance factor of one and if the tolerance factor is in the range between $0.89 \leq t \leq 1.00$, the cubic crystal phase is still attainable. However, due to the difference of the atomic radii of the atoms distorted structures could be formed and Figure 2.6 shows the perovskite structures for orthorhombic and hexagonal crystal phases [85]. The perovskite compounds generally compose in cubic, orthorhombic, hexagonal, tetragonal and rhombohedral crystal phases [52]. Also, the crystal phases could be transform from rhombohedral to orthorhombic, orthorhombic to tetragonal and tetragonal to cubic phases with the temperature increment [85].

$$t = \frac{(r_A + r_X)}{\sqrt{2} (r_B + r_X)} \quad (2.69)$$

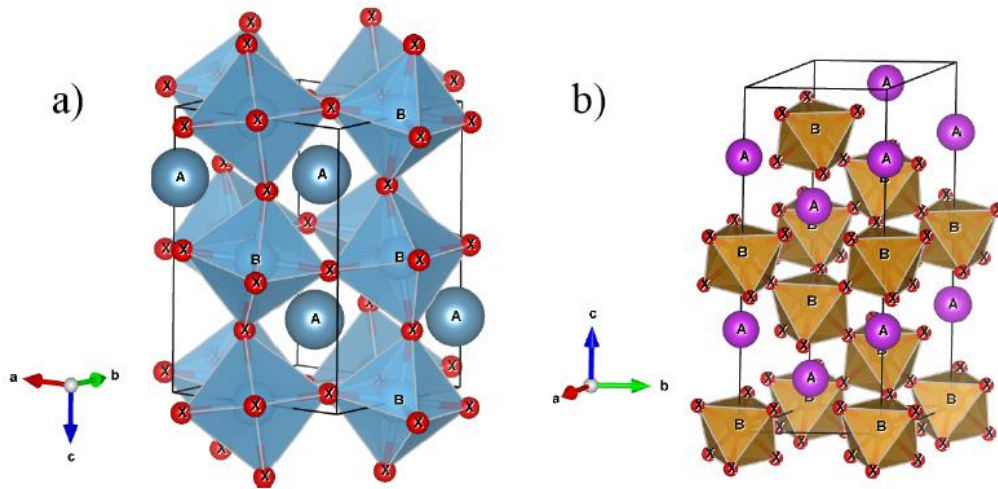


Figure 2.6 (a) Orthorhombic and (b) hexagonal perovskite crystal structures [85]

The perovskite materials are ceramic materials with proton conductivity, ferroelectricity, super conductivity, high dielectric constant, etc. [86] that enable to use them in many technological fields such as in solar cells [87], optoelectronics [88], proton conductors [89], etc. The perovskite compounds could be synthesized with solid-state reactions, gas phase preparations, precipitation, etc. [90]. The aim of this thesis comes from the investigation of the perovskite materials for hydrogen storage especially due to the ceramic nature of perovskite materials applying in portable power applications.

2.8. VASP Software

The Vienna Ab-initio Simulation Package (VASP) [29], [30] is based on DFT which calculate the main physical properties of solids such as elastic constants, band structures, density of states, phonon dispersion curves, optical properties, etc. VASP could take the pseudopotentials as LDA and GGA. Also, the hybrid potentials could be employed to VASP. VASP needs four input files as INCAR, POSCAR, POTCAR and KPOINTS. The INCAR file is the input file that has the required parameters for

the calculations. The POSCAR file includes the crystal information with the positions of each atom. The POTCAR file has the potentials of the atoms in the structure. The KPOINTS file defines the number of k-points in the first Brillouin zone. For the k-points generation two methods could be used: Gamma centered k-points and Monkhorst-Pack scheme. These input files have been presented in Appendix B. Also, “VASP.5.4.4” version has been used in this thesis.

The DFT calculations have been performed with ISIF=3 parameter to conserve the beginning crystal symmetry. Also, the force convergence criterion has been set to lower than 10^{-9} eV/Å for the stresses and Hellmann-Feynman forces. The energy tolerance criterion has been set to 10^{-10} eV per unit cell for the solution of the Kohn-Sham equations. The k-points have been sampled with a gamma centered [91] or Monkhorst-Pack [92] grid according to the crystal structure. The cut off energies have been determined according to the compound. Table 2.2 lists the employed k-points and the cutoff energies for the studied compounds.

Table 2.3 The k-points (MP for Monkhorst-Pack grid and GC for Gamma centered grid) and the cut off energies($E_{cut\ off}$ in eV) for the studied compounds

Compound	Crystal Phase	K-point	$E_{cut\ off}$
BaScO ₃	Orthorhombic	6 x 8 x 8 MP	1000
	Tetragonal	18 x 18 x 14 MP	
	Rhombohedral	16 x 16 x 16 MP	
	Hexagonal	12 x 12 x 3 GC	
	Cubic	16 x 16 x 16 GC	
BaYO ₃	Orthorhombic	6 x 8 x 8 MP	1000
	Tetragonal	10 x 10 x 8 GC	
	Rhombohedral	14 x 14 x 14 MP	
	Hexagonal	12 x 12 x 3 GC	
	Cubic	15 x 15 x 15 GC	
MgTiO ₃	Cubic	12 x 12 x 12 GC	800
CaTiO ₃	Cubic	12 x 12 x 12 GC	600
Ca ₃ CH and Ca ₃ NH	Cubic	10 x 10 x 10 GC	550
LiNiH ₃	Cubic	12 x 12 x 12 GC	600
NaNiH ₃ and KNiH ₃	Cubic	12 x 12 x 12 GC	550

CHAPTER 3

HYDROGEN STORAGE STUDIES FOR PEROVSKITE MATERIALS

3.1. Introduction

In this chapter, structural, mechanic, electronic, vibrational and hydrogen storage properties of perovskite materials have been investigated. For this purpose, two material groups have been studied which are $BaXO_3$ where X is Sc or Y, and $XTiO_3$ where X is Mg or Ca. In the following sections, the studies for these perovskite compounds will be presented separately for $BaXO_3$ and $XTiO_3$. In addition, some part of the studies for $BaXO_3$ have been accepted to publish in Canadian Journal of Physics with the title of “DFT Study of $BaScO_3H_{0.5}$ Compound and Its Hydrogen Storage Properties” and have been under review in International Journal of Hydrogen Energy with the title of “Properties of $BaYO_3$ Perovskite and Hydrogen Storage Properties of $BaYO_3H_x$ ”. Moreover, some part of the studies for $XTiO_3$ have been published in International Journal of Hydrogen Energy with the title of “ $MgTiO_3H_x$ and $CaTiO_3H_x$ Perovskite Compounds for Hydrogen Storage Applications”.

3.2. Studies for $BaXO_3$ (X= Sc or Y)

3.2.1. Structural Optimization for $BaXO_3$

$BaXO_3$ (where X is Sc or Y) perovskite compounds have been investigated using VASP. Perovskite compounds generally crystallize in five possible crystal phases: cubic (Pm-3m), tetragonal (P4mm), hexagonal (P-3m1), rhombohedral (R-3c) and orthorhombic (Pbnm) [52]. Therefore, these compounds have been studied in these crystal structures in order to determine the most stable phases of these compounds and then the hydrogen bonding studies have been performed using the most stable phases

of these compounds. In literature, Narejo et. al. [93] studied BaScO_3 perovskite compound in the cubic crystal structure and there is no study for the remaining crystal phases. Also, BaYO_3 is a hypothetical compound and there is no study to compare the obtained results for this compound. Figure 3.1 shows the crystal structures for the five possible crystal phases of BaXO_3 and Table 3.1 lists the optimized lattice parameters, the calculated formation energies using equation given in Chapter 2 and the atomic positions. The lattice parameter for the cubic phase of BaScO_3 is consistent with the literature. All the structures have negative formation energies that imply these structures are energetically stable and synthesizable. In addition, the formation energies for BaScO_3 phases are more negative than BaYO_3 phases which shows that BaScO_3 phases are energetically more stable except the cubic phase.

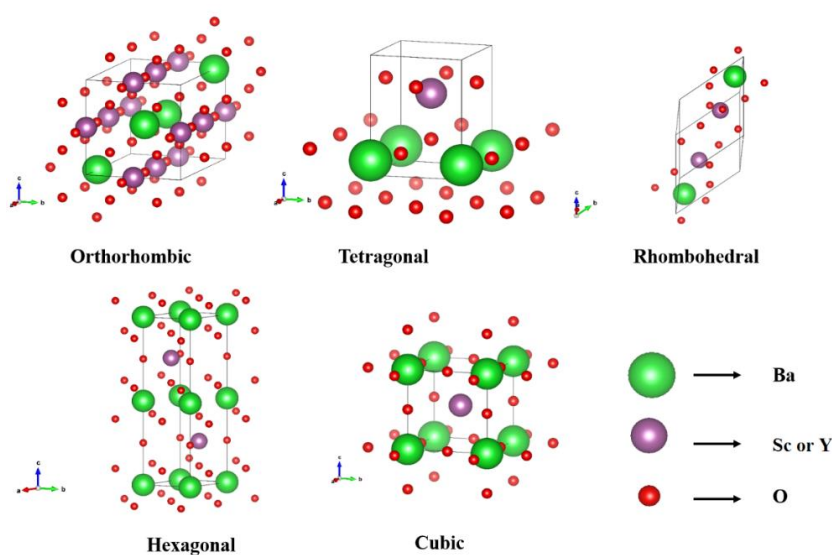


Figure 3.1 The crystal structures of BaXO_3 for cubic, tetragonal, hexagonal, rhombohedral, and orthorhombic phases

Table 3.1 The optimized lattice parameters (a, b, c in Å), the calculated formation energies (ΔE_{For} in eV/atom) and the atomic positions for BaXO_3

Phase	Compound	a	b	c	ΔE_{For}	Atomic Positions
Orthorhombic	BaScO_3	5.94	8.41	5.95	-2.78	Ba: 4c (0.482, 0.250, 0.505) Sc: 4b (0.500, 0.000, 0.000) O ₁ : 4c (0.514, 0.250, 0.073) O ₂ : 8d (0.776, 0.539, 0.225)
	BaYO_3	6.36	9.79	6.37	-1.10	Ba: 4c (0.499, 0.250, 0.000) Y: 4b (0.500, 0.000, 0.000) O ₁ : 4c (0.999, 0.250, 0.500) O ₂ : 8d (0.749, 0.499, 0.250)
Tetragonal	BaScO_3	3.95	3.95	5.19	-2.69	Ba: 1a (0.000, 0.000, 0.123) Sc: 1b (0.500, 0.500, 0.641) O ₁ : 2c (0.500, 0.000, 0.753) O ₂ : 1b (0.500, 0.500, 0.259)
	BaYO_3	3.88	3.88	6.36	-2.26	Ba: 1b (0.500, 0.500, 0.602) Y: 1a (0.000, 0.000, 0.016) O ₁ : 2c (0.500, 0.000, 0.845) O ₂ : 1b (0.500, 0.500, 0.219)
Rhombohedral	BaScO_3	6.43	6.43	6.43	-2.64	Ba: 6c (0.000, 0.000, 0.127) Sc: 6c (0.000, 0.000, 0.342) O: 18f (0.068, 0.318, 0.263)
	BaYO_3	6.61	6.61	6.61	-1.65	Ba: 6c (0.000, 0.000, 0.370) Y: 6c (0.000, 0.000, 0.153) O: 18f (-0.046, 0.262, 0.240)
Hexagonal	BaScO_3	3.81	-	13.59	-2.56	Ba: 2a (0.000, 0.000, 0.000) Sc: 2c (0.333, 0.666, 0.250) O ₁ : 2b (0.000, 0.000, 0.250) O ₂ : 4f (0.333, 0.666, 0.398)
	BaYO_3	3.94	-	14.15	-1.35	Ba: 2c (0.333, 0.666, 0.205) Y: 2a (0.000, 0.000, 0.000) O ₁ : 2b (0.000, 0.000, 0.250) O ₂ : 4f (0.333, 0.666, 0.062)
Cubic	BaScO_3	4.59	-	-	-0.70	Ba: 1a (0.000, 0.000, 0.000) Sc: 1b (0.500, 0.500, 0.500) O: 3d (0.500, 0.000, 0.000)
	BaScO_3	4.14 ^[93]	-	-	-	-
	BaYO_3	4.43	-	-	-2.67	Ba: 1a (0.000, 0.000, 0.000) Y: 1b (0.500, 0.500, 0.500) O: 3d (0.500, 0.000, 0.000)

In order to determine the most stable crystal phase of BaXO_3 , the energy as a function of volume and the enthalpy as a function of pressure have been studied. Figure 3.2 shows the energy as a function of volume for BaScO_3 and as can be seen from the figure, the most stable crystal structure is the orthorhombic crystal phase having the lowest volume and the lowest energy. In addition, there is no phase transition above 0

GPa pressure as can be seen from Figure 3.3 which shows the enthalpy as a function of pressure for BaScO₃. Figure 3.4 shows the energy as a function of volume for BaYO₃ and as can be seen from the figure, the most stable crystal phase of this structure is the cubic phase of BaYO₃ among the considered phases. Furthermore, there is no phase transition above 0 GPa pressure for BaYO₃ as can be seen from Figure 3.5 which shows the enthalpy as a function of pressure for BaYO₃.

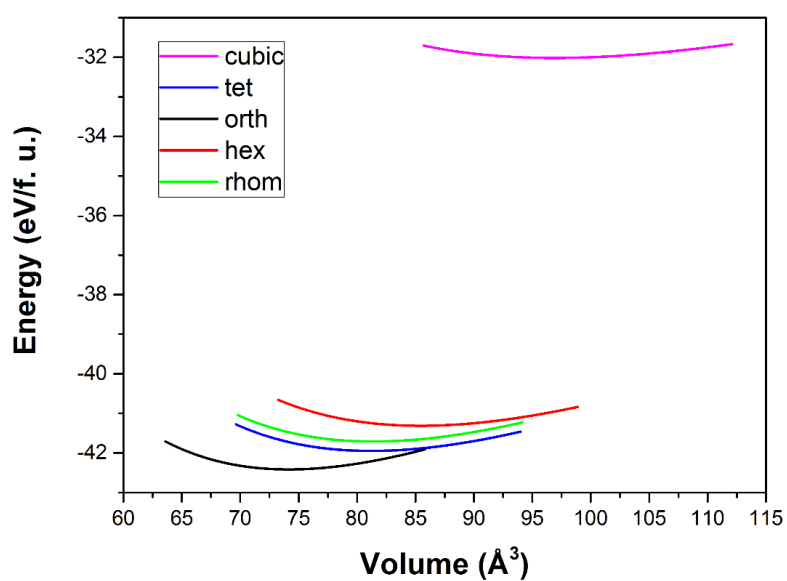


Figure 3.2 The energy as a function of volume for different crystal phases of BaScO₃

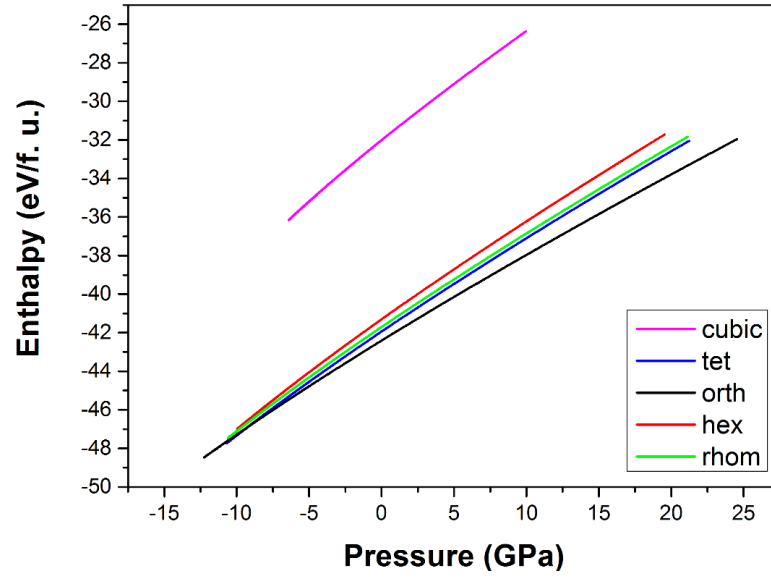


Figure 3.3 The enthalpy as a function of pressure for different crystal phases of $BaScO_3$

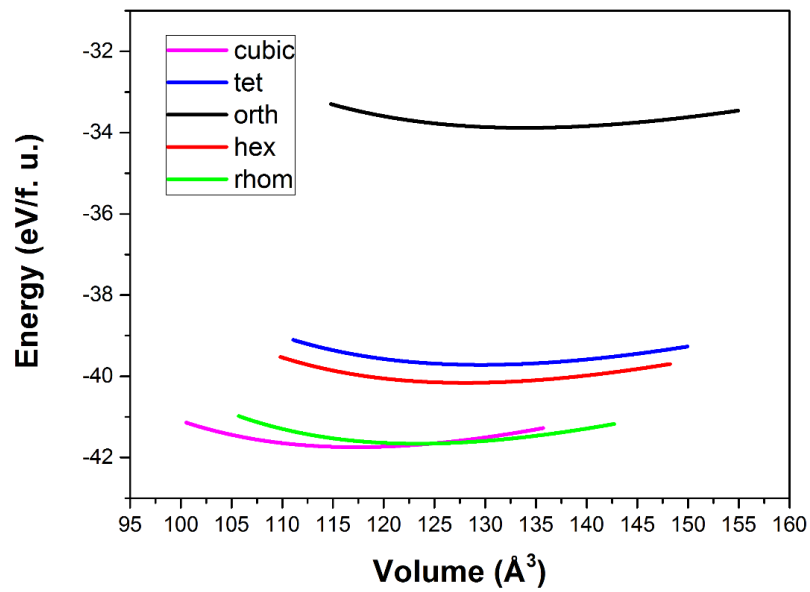


Figure 3.4 The energy as a function of volume for different crystal phases of $BaYO_3$

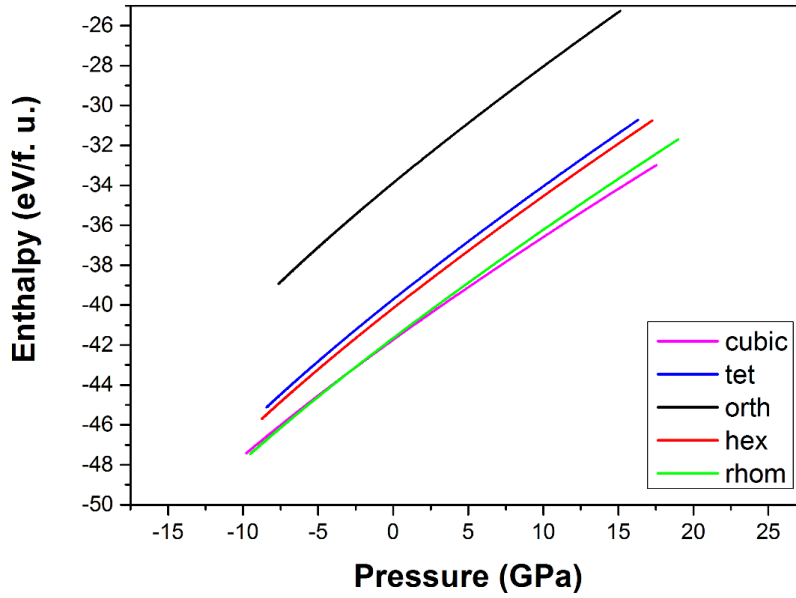


Figure 3.5 The enthalpy as a function of pressure for different crystal phases of $BaYO_3$

In order to determine the crystalline nature which plays a key role for the structural properties of materials, X-ray diffraction patterns are studied. Figure 3.6 shows the X-ray diffraction patterns for $BaScO_3$ orthorhombic phase and $BaYO_3$ cubic phase. These patterns have been obtained using VESTA program [53] with Cu $K\alpha$ source that has wavelength of 1.541 Å. Both compounds show polycrystalline property as can be deduced from the figure. In addition, $BaScO_3$ orthorhombic phase has 2θ value as 21.12° in (2 0 0) plane and $BaYO_3$ cubic phase has 2θ value as 28.48° in (-1 1 0) plane.

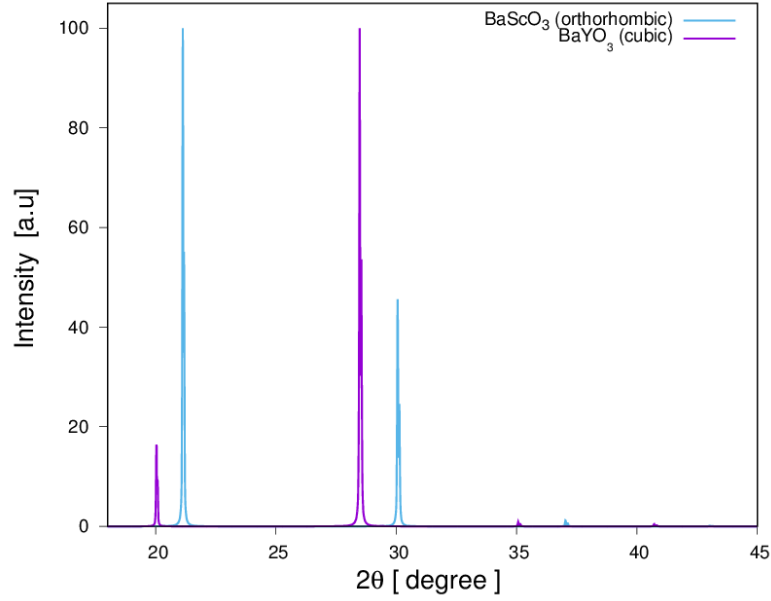


Figure 3.6 X-ray diffraction patterns for BaScO₃ orthorhombic phase and BaYO₃ cubic phase

3.2.2. Electronic Properties for BaXO₃

The band structures and corresponding partial density of states (PDOS) have been presented that were obtained along the high symmetry points in the first Brillouin zone. The results for the most stable phases have been presented here and the results for the remaining phases have been presented in Appendix A not to cover a lot of space in this section. Figure 3.7 shows the band structure and Figure 3.8 shows the PDOS for BaScO₃ orthorhombic phase. BaScO₃ orthorhombic phase shows semiconducting behavior as can be deduced from the figure and the band gap is 3.80 eV. Also, the most significant contribution to the PDOS above the Fermi level comes from the d states of Sc atoms.

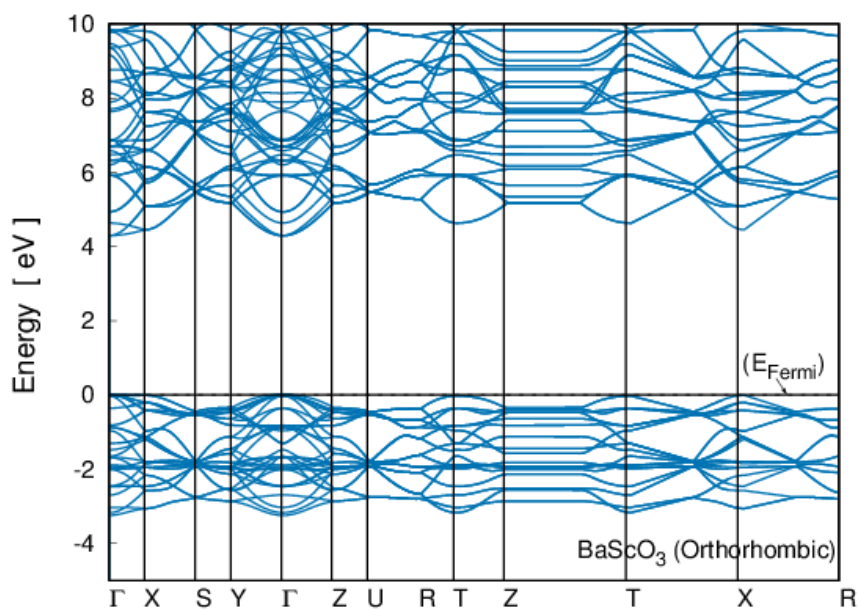


Figure 3.7 The band structure for BaScO₃ orthorhombic phase

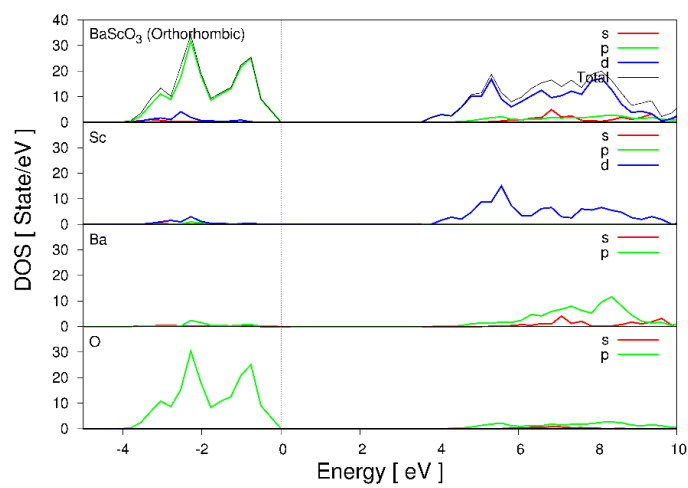


Figure 3.8 The partial density of states for BaScO₃ orthorhombic phase

Figure 3.9 shows the band structure for BaYO₃ cubic phase that shows semiconducting behavior with 4.30 eV band gap. Moreover, the PDOS for BaYO₃ cubic phase has been shown in Figure 3.10 and the most significant contribution to the PDOS above the Fermi level comes from the p states of Ba atom.

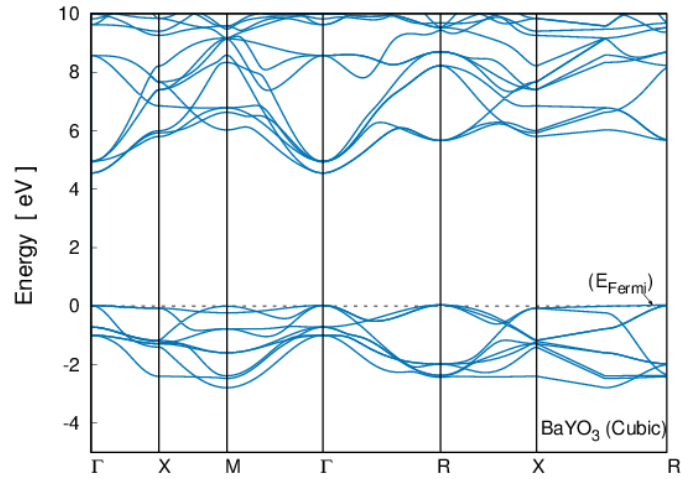


Figure 3.9 The band structure for BaYO₃ cubic phase

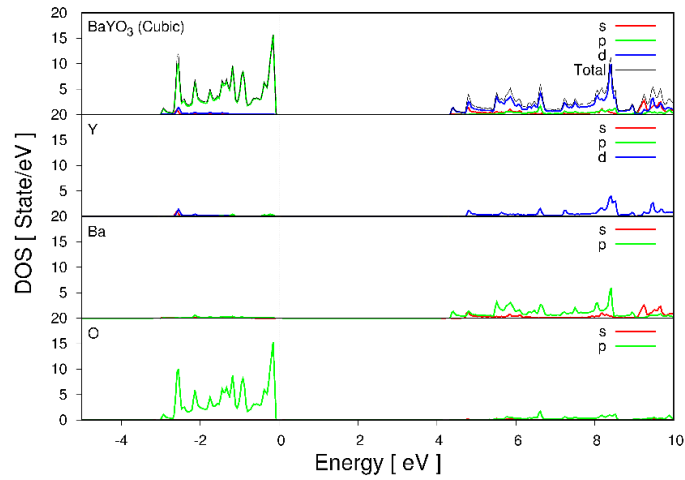


Figure 3.10 The partial density of states for BaYO₃ cubic phase

Figure 3.11a and Figure 3.11b show the electron-density distributions for BaScO₃ orthorhombic phase in (1 1 0) plane and BaYO₃ cubic phase in (1 0 0) plane, respectively. As can be seen from the figures, both compounds have ionic bonding. In addition, the Bader partial charge analysis were performed in order to determine the charge of each ion in the structure. If the Bader net charge is positive, the charge is transferred away from the atom. On the other hand, the charge is transferred to the atom when the Bader partial charge is negative. Table 3.2 lists the obtained Bader net partial charges for BaXO₃ where the total Bader net charges are zero. Also, the charge is transferred away from the O atoms while it is transferred to Sc/Y and Ba atoms. BaYO₃ cubic phase has one Ba atom, one Y atom and three O atoms in its unit cell, while BaScO₃ orthorhombic phase has four Ba atoms, four Sc atoms and twelve O atoms in its unit cell. So, the net charge for the same atom in these compounds differ.

Table 3.2 The Bader net charges (in units of e per unit cell) for BaXO₃

Ion	BaScO₃	BaYO₃
Ba	6.46	1.54
Sc or Y	8.00	1.99
O	-14.46	-3.53

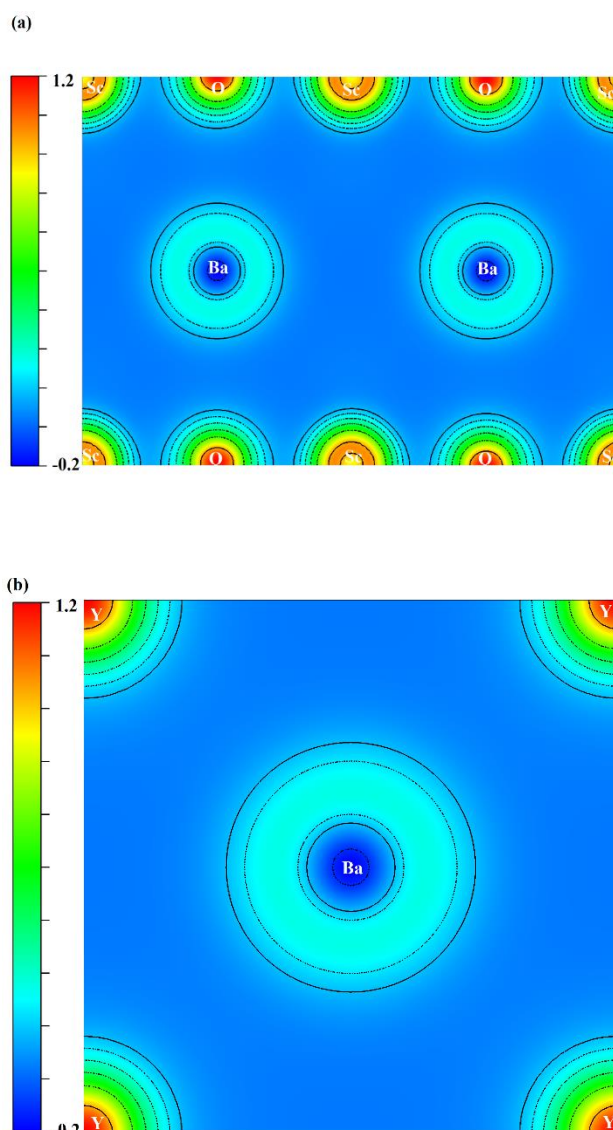


Figure 3.11 The electron-density distributions for (a) BaScO₃ orthorhombic phase and (b) BaYO₃ cubic phase

3.2.3. Mechanical Properties for BaXO₃

The elastic constants (C_{ij}) for BaXO₃ compounds were calculated using stress-strain method. Table 3.3 lists the obtained elastic constants for the five possible phases of BaXO₃. These elastic constants must satisfy the Born stability criteria and the details of these criteria have been presented in Chapter 2. The tetragonal and the cubic phases

of BaScO₃ compound have not satisfied these criteria so these phases are found to be mechanically unstable. In addition, only the orthorhombic phase is mechanically unstable for BaYO₃. The remaining structures for BaYO₃ are found to be mechanically stable. The further mechanical properties for the stable compounds could be obtained using these constants.

Table 3.3 The calculated elastic constants (C_{ij} in GPa) for BaXO₃

BaScO₃	C₁₁	C₁₂	C₁₃	C₂₂	C₂₃	C₃₃	C₄₄	C₅₅	C₆₆
Orthorhombic	217.30	63.90	64.20	185.20	96.80	185.70	78.20	44.20	44.20
Tetragonal	202.60	39.50	70.50			135.60	50.00		-4.50
Rhombohedral	114.97	81.08	73.71			110.67	26.07		0.54
Hexagonal	113.62	65.71	59.47			178.29	30.74		23.96
Cubic	76.90	55.90					-2.60		
BaYO₃	C₁₁	C₁₂	C₁₃	C₂₂	C₂₃	C₃₃	C₄₄	C₅₅	C₆₆
Orthorhombic	82.90	69.80	69.20	55.60	74.70	55.30	-14.10	-1.20	-0.50
Tetragonal	135.50	46.70	52.70			128.10	34.00		1.60
Rhombohedral	132.19	67.70	50.27			100.94	21.15		30.21
Hexagonal	135.97	98.56	38.09			76.91	23.07		18.71
Cubic	182.60	37.90					33.50		

Table 3.4 lists the obtained bulk modulus, shear modulus, Young's modulus, Poisson's ratio, G/B ratio and B/G ratio for orthorhombic, rhombohedral and hexagonal phases of BaScO₃ and tetragonal, rhombohedral, hexagonal and cubic phases of BaYO₃. The highest bulk modulus, shear modulus and Young's modulus belong to the orthorhombic phase of BaScO₃. All these phases have ionic bonding according to the results of the Poisson's ratio and G/B ratio that are consistent with the electron-density distributions. Also, these phases are ductile materials due to having B/G ratios higher than 1.75.

Table 3.4 Bulk modulus (B in GPa), Shear modulus (G in GPa), Young's modulus (E in GPa), Poisson's ratio (ν), G/B ratio and B/G ratio for the mechanically stable phases of $BaXO_3$

Phase	Compound	B	G	E	ν	G/B	B/G
Orthorhombic	BaScO ₃	115.30	55.40	143.20	0.29	0.48	2.08
Tetragonal	BaYO ₃	78.10	18.60	51.70	0.39	0.24	4.20
Rhombohedral	BaScO ₃	88.40	8.00	23.20	0.46	0.09	11.05
	BaYO ₃	76.60	26.60	71.40	0.33	0.35	2.90
Hexagonal	BaScO ₃	84.70	30.60	81.90	0.34	0.36	2.77
	BaYO ₃	70.80	23.40	63.20	0.35	0.33	3.03
Cubic	BaYO ₃	86.10	45.80	116.70	0.27	0.53	1.88

The anisotropic elastic properties have been studied and here only the results for the most stable phases for $BaXO_3$ will be presented. Figure 3.12 and Figure 3.13 show the direction dependent Young's modulus, linear compressibility, shear modulus and Poisson's ratio both in 2D and 3D for BaScO₃ orthorhombic phase and BaYO₃ cubic phase, respectively. When the material is isotropic, the direction dependent parameter has a shape of circle or sphere. If the material is anisotropic, then the shape is distorted from circle or sphere. Also, the blue curves in Figure 3.12 and Figure 3.13 show the maximum values, while the green ones show the minimum values of that parameter. For BaScO₃ orthorhombic phase, the linear compressibility is found as isotropic in all planes. Also, Young's modulus and Poisson's ratio are found as isotropic in yz plane. The remaining parameters are found as anisotropic for BaScO₃ orthorhombic phase. For BaYO₃, the linear compressibility is found as isotropic in all planes, while the Young's modulus, shear modulus and Poisson's ratio are found as anisotropic in all planes. In addition, the minimum and maximum values for these parameters have been listed in Table 3.5.

Table 3.5 The minimum and maximum values of Young's modulus (E in GPa), linear compressibility (β), shear modulus (G in GPa), and Poisson's ratio (ν) for $BaXO_3$

Compound	E		β		G		ν	
	E_{min}	E_{max}	β_{min}	β_{max}	G_{min}	G_{max}	ν_{min}	ν_{max}
BaScO ₃	117.60	188.44	2.87	2.87	44.15	78.22	0.09	0.47
BaYO ₃	88.97	169.57	3.87	3.87	33.50	72.35	0.10	0.51

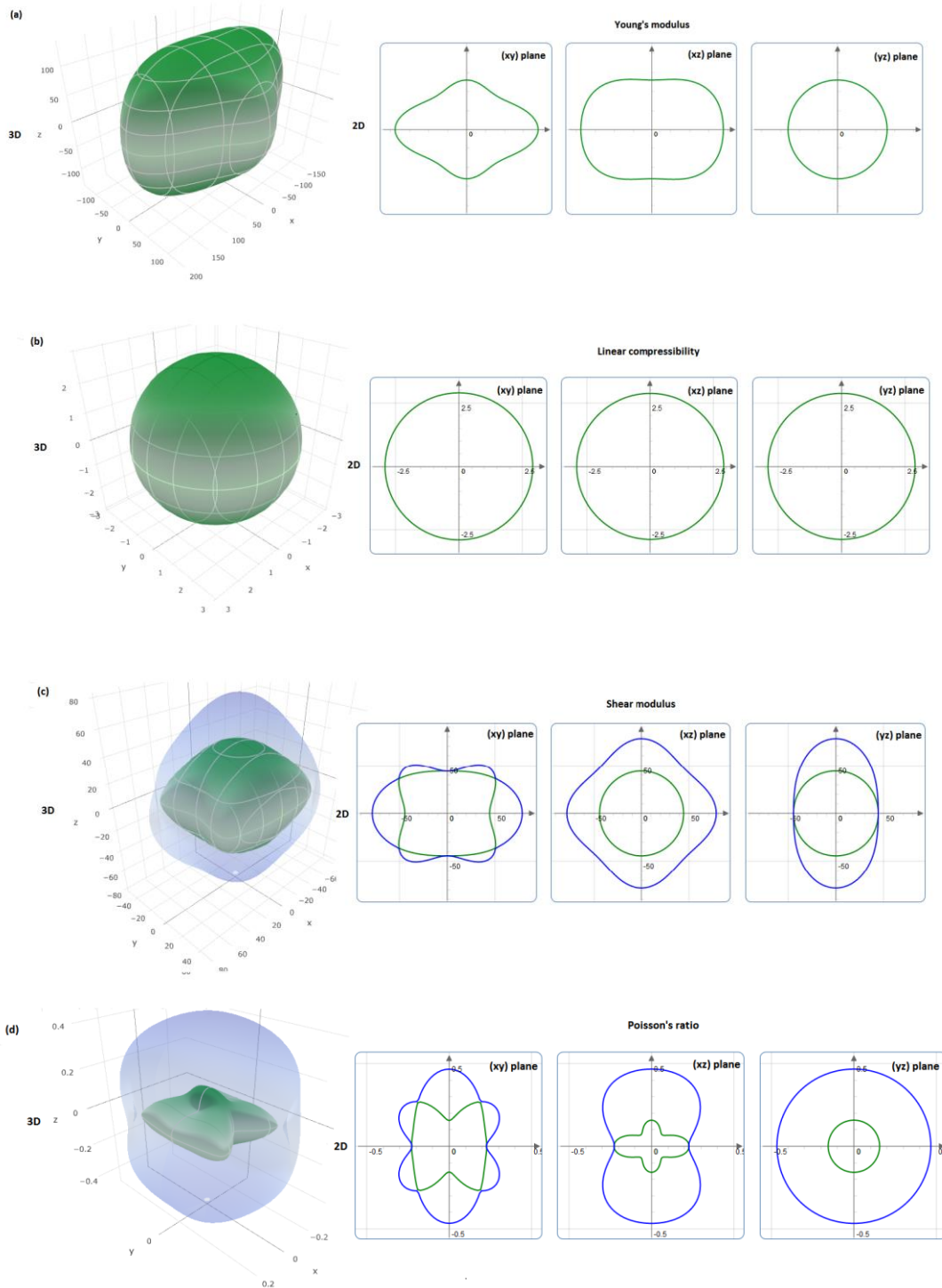


Figure 3.12 The direction dependent (a) Young's modulus, (b) linear compressibility, (c) shear modulus, and (d) Poisson's ratio both in 2D and 3D for BaScO_3 orthorhombic phase

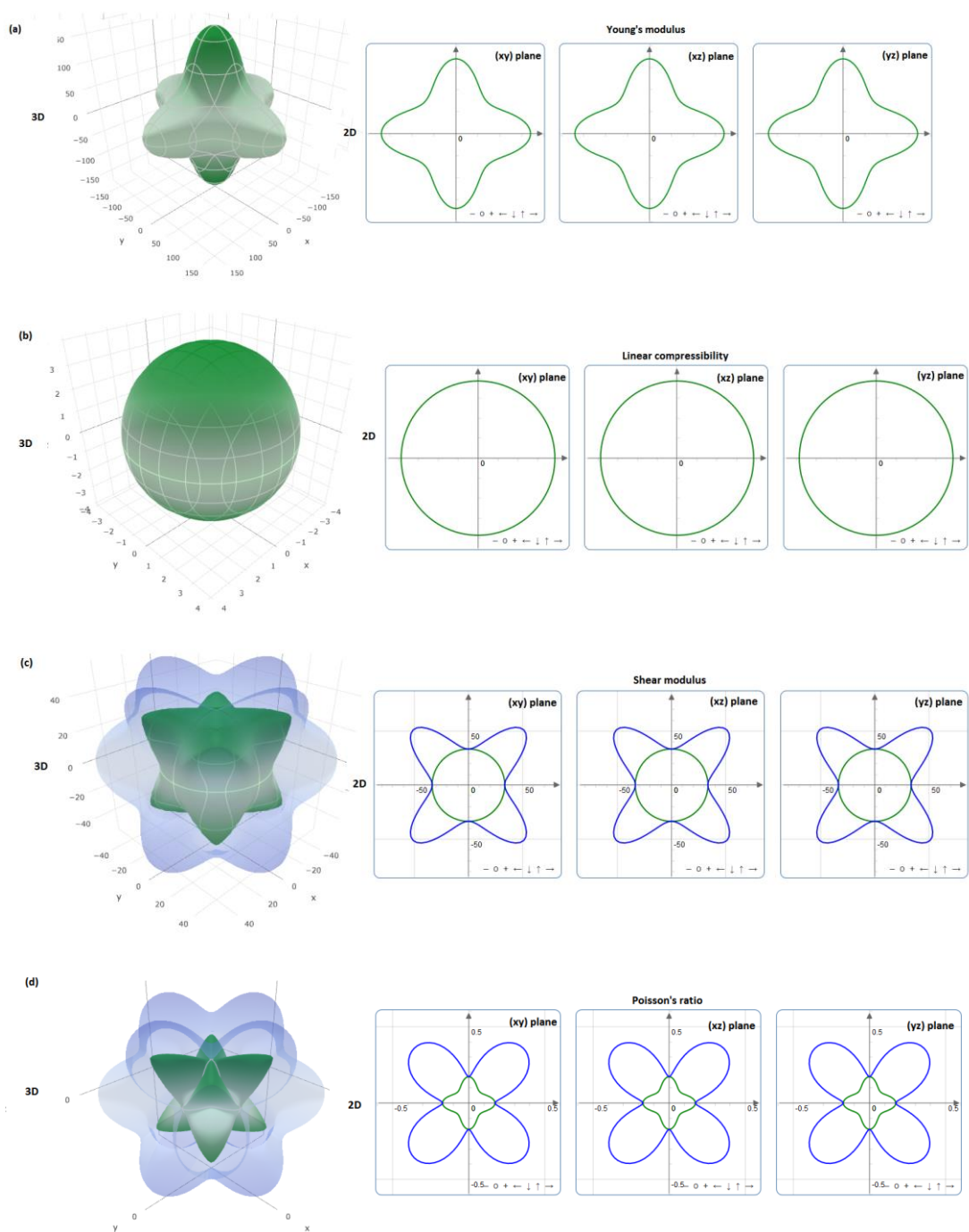


Figure 3.13 The direction dependent (a) Young's modulus, (b) linear compressibility, (c) shear modulus, and (d) Poisson's ratio both in 2D and 3D for BaYO_3 cubic phase

3.2.4. Vibrational Properties for BaXO₃

The vibrational stability is an important property for these materials. The vibrational properties were calculated using linear response method. The 2x1x2 supercell was generated using PHONOPY [94] software for BaScO₃ orthorhombic phase that employed to VASP. Figure 3.14 shows phonon dispersion curves and phonon density of states (PDOS) for BaScO₃ orthorhombic phase that has 20 atoms in its crystal structure. Therefore, there is 60 phonon branches in Figure 3.14 where three of them are optic branches and the remaining are acoustic ones. Moreover, BaScO₃ is dynamically stable because there is no soft mode as can be seen from Figure 3.14. Furthermore, Sc atoms give more contributions to the acoustic modes and Ba and Sc atoms give more contributions to the low optic modes.

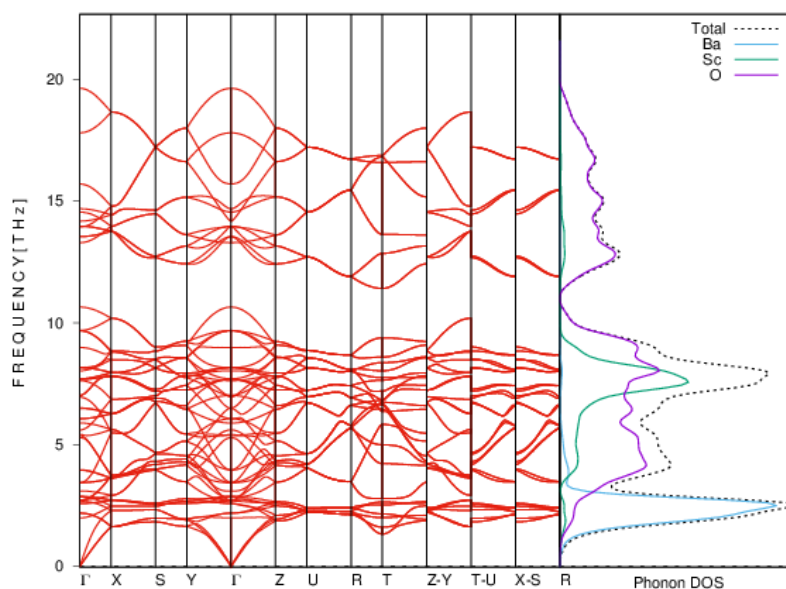


Figure 3.14 Phonon dispersion curve and phonon density of states for BaScO₃ orthorhombic phase

The phonon dispersion curves and corresponding PDOS were obtained using 2x2x2 supercell for BaYO₃ cubic phase as shown in Figure 3.15. BaYO₃ cubic phase has five atoms in its crystal structure, so there are fifteen phonon branches in the figure where

three of them are acoustic branches and the remaining of them are optic ones. As can be seen from the figure BaYO_3 cubic phase is found to be dynamically unstable compound with the soft modes.

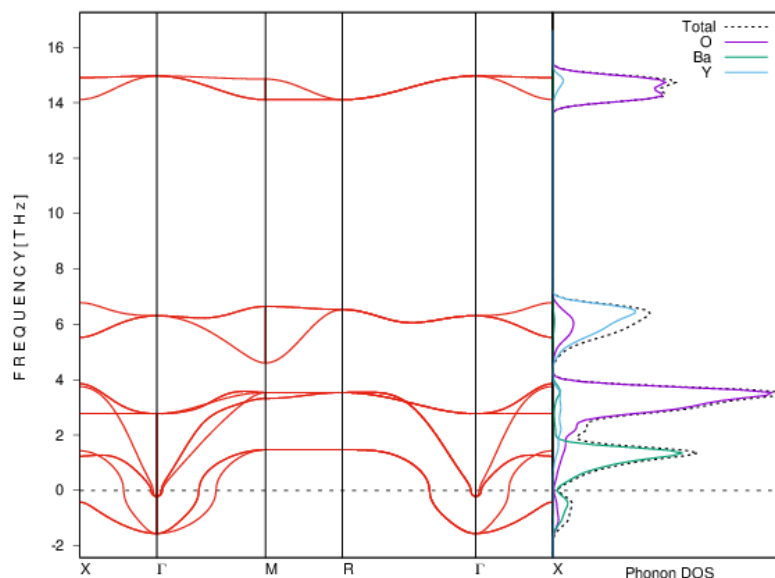


Figure 3.15 Phonon dispersion curve and phonon density of states for BaYO_3 cubic phase

3.2.5. Hydrogen Storage Studies for BaXO_3

The orthorhombic phase and the cubic phase are found to be the most stable phases for BaScO_3 and BaYO_3 , respectively. Hence, the hydrogen doping studies were only performed for these phases with the ordered crystal structures. For this purpose, the possible H positions should be determined. The orthorhombic phase of BaScO_3 belongs to 62 space group (Pbnm) where Ba atoms are at 4c, Sc atoms are at 4b and O atoms are at 4c and 8d Wyckoff positions. Two hydrogen atoms were doped at (0, 0, 0) and (0.5, 0.5, 0.5) positions. Addition of two hydrogen atoms provide to obtain $\text{BaScO}_3\text{H}_{0.5}$ chemical formula. Figure 3.16 shows the crystal structure for $\text{BaScO}_3\text{H}_{0.5}$.

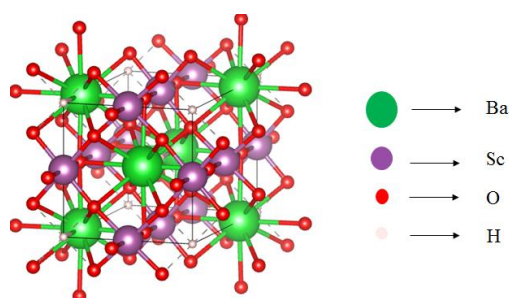


Figure 3.16 The crystal structure of $BaScO_3H_{0.5}$

For $BaYO_3$, the space group of the cubic phase is 221 (Pm-3m) where Ba atom is at the 1b, Y atom is at the 1a and O atoms are at the 3d Wyckoff positions. The possible hydrogen doping position was chosen as 3c Wyckoff position and doping of three hydrogen atoms provide to obtain $BaYO_3H_3$ chemical formula. After obtaining $BaYO_3H_3$, six more hydrogen atoms were doped at 6e Wyckoff position and $BaYO_3H_9$ has been obtained. The crystal structures for $BaYO_3H_3$ and $BaYO_3H_9$ have been shown in Figure 3.17a and Figure 3.17b, respectively.

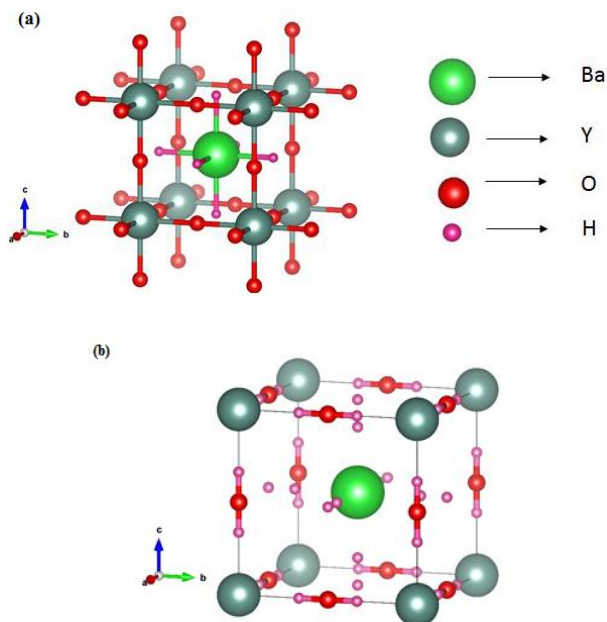


Figure 3.17 The crystal structures of (a) $BaYO_3H_3$ and (b) $BaYO_3H_9$

The obtained lattice parameters, the calculated formation energies and the atomic positions have been listed in Table 3.6 for BaScO₃ and BaYO₃ compounds. As can be seen from the table, the negative formation energies indicate that these compounds are energetically stable and synthesizable. On the other hand, BaYO₃H₉ is found to be energetically unstable due having positive formation energy. Also, it is found that the lattice constants enlarge with the increasing number of hydrogen atoms in the structure when the lattice constants are compared, .

Table 3.6 The optimized lattice parameters (a, b, c in Å), the calculated formation energies (ΔE_{For} in eV/atom) and atomic positions for BaScO₃H_{0.5}, BaYO₃H₃, and BaYO₃H₉

Compound	a	b	c	ΔE_{For}	Atomic Positions
BaScO ₃ H _{0.5}	5.84	8.76	5.85	-2.40	Ba: 4c (0.500, 0.280, 0.501) Sc: 4b (0.500, 0.000, 0.000) O ₁ : 4c (0.500, 0.250, 0.030) O ₂ : 8d (0.735, 0.501, 0.264) H ₁ : (0.000, 0.000, 0.000) H ₂ : (0.500, 0.500, 0.500)
BaYO ₃ H ₃	4.55	-	-	-0.81	Ba: 1a (0.000, 0.000, 0.000) Y: 1b (0.500, 0.500, 0.500) O: 3d (0.500, 0.000, 0.000) H ₃ : 3c (0.000, 0.500, 0.500)
BaYO ₃ H ₉	5.97	-	-	0.35	Ba: 1a (0.000, 0.000, 0.000) Y: 1b (0.500, 0.500, 0.500) O: 3d (0.500, 0.000, 0.000) H ₁ : 3c (0.000, 0.500, 0.500) H ₂ : 6e (0.333, 0.000, 0.000)

The X-ray diffraction patterns were obtained for energetically stable compounds as can be shown in Figure 3.18. The compounds show polycrystalline nature as deduced from the figure. Also, BaScO₃H_{0.5} has 2 θ value as 20.25° in (2 0 0) plane and BaYO₃H₃ has 27.69° in (-1 1 0) plane.

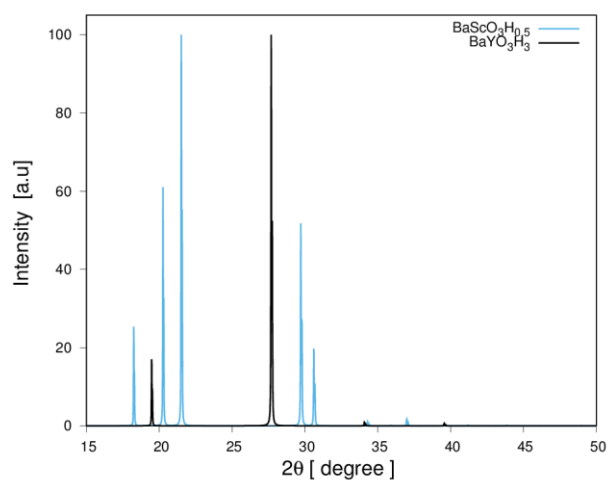


Figure 3.18 X-ray diffraction patterns for $BaScO_3H_{0.5}$ and $BaYO_3H_3$

The electronic properties have been studied for these compounds. Figure 3.19 and Figure 3.20 show the band structures and corresponding density of states for $BaScO_3H_{0.5}$, respectively. $BaScO_3H_{0.5}$ has a narrow band gap of 0.57 eV as can be deduced from Figure 3.19 where, the band gap of $BaScO_3$ decreases from 3.80 eV to 0.57 eV after the hydrogen atoms are bonded. In addition, it can be seen that the most significant contribution to the PDOS below the Fermi level comes from O and Ba atoms for both compounds from Figure 3.20.

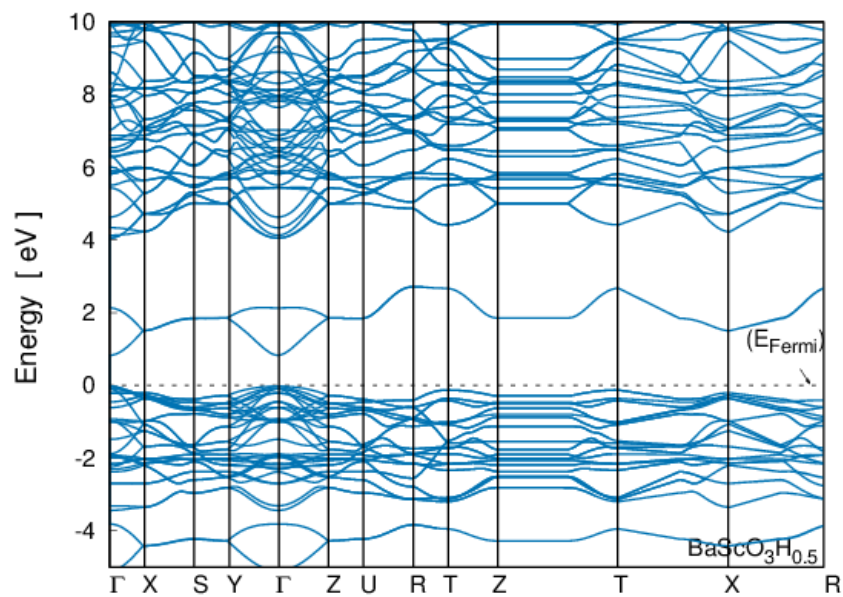


Figure 3.19 The band structure for BaScO₃H_{0.5}

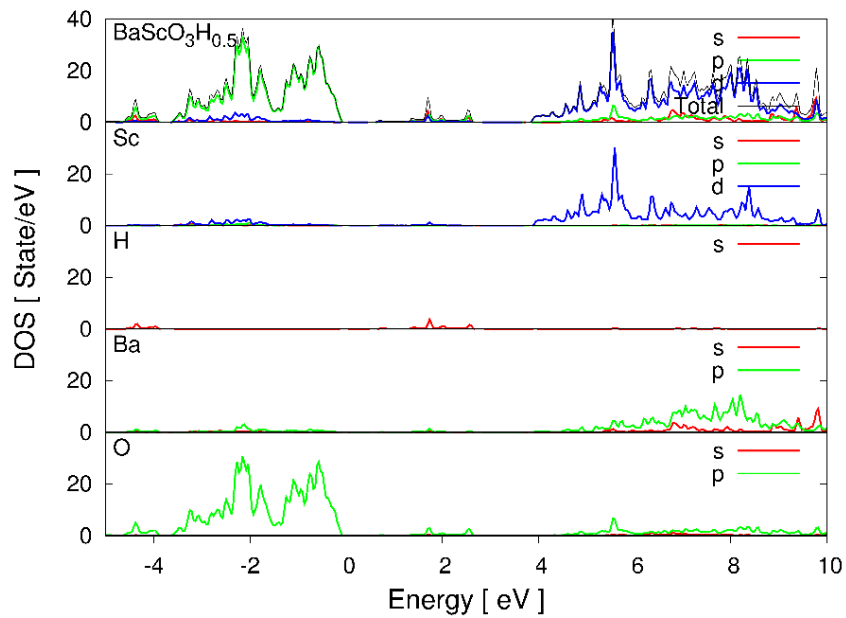


Figure 3.20 The partial density of states for BaScO₃H_{0.5}

Figure 3.21 and Figure 3.22 show the band structure and corresponding PDOS for BaYO_3H_3 that is the only stable compound for the hydrogen bonded BaYO_3 . These figures show that this compound has metallic character and the most significant contribution to the PDOS comes from the p states of O atoms below the Fermi level. After the hydrogen atoms are bonded to BaYO_3 , the semiconducting character of BaYO_3 changes to the metallic character.

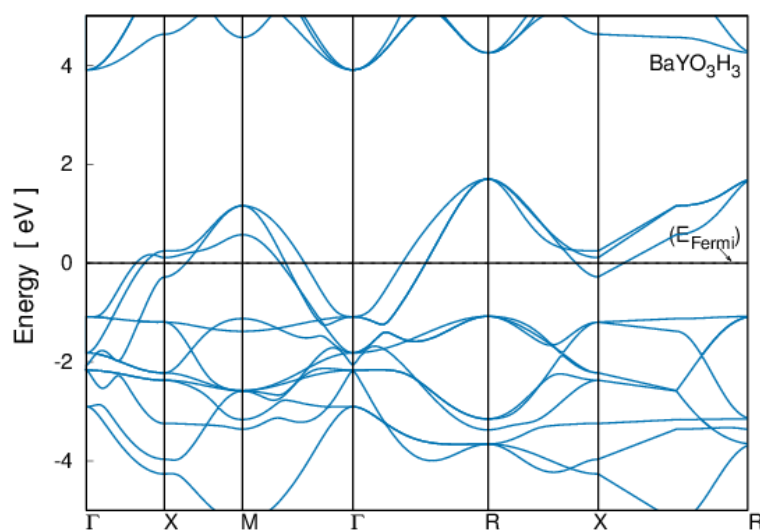


Figure 3.21 The band structure for BaYO_3H_3

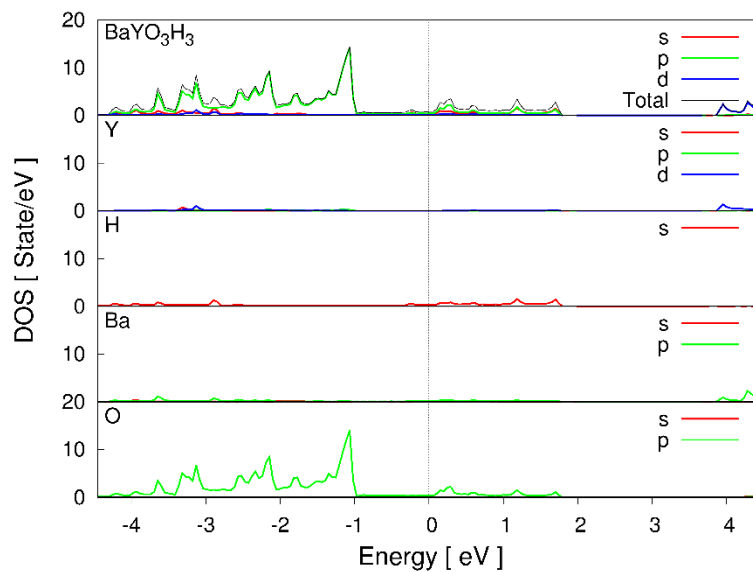


Figure 3.22 The partial density of states for BaYO₃H₃

Figure 3.23a and Figure 3.23b show the electron-density distributions for BaScO₃H_{0.5} and BaYO₃H₃, respectively. The effect of the H atoms to the electron-density distributions can be seen in the figures. Furthermore, the Bader partial charge analysis were performed. The Bader net partial charges of these compounds have been listed in Table 3.7. As can be concluded from the table, the total Bader net charges are zero for both compounds. For BaScO₃H_{0.5}, the charge is transferred to O atoms while it is transferred to Ba, Sc and H atoms. For BaYO₃H₃, the charge is transferred away from Ba and Y atoms while it is transferred to O and H atoms.

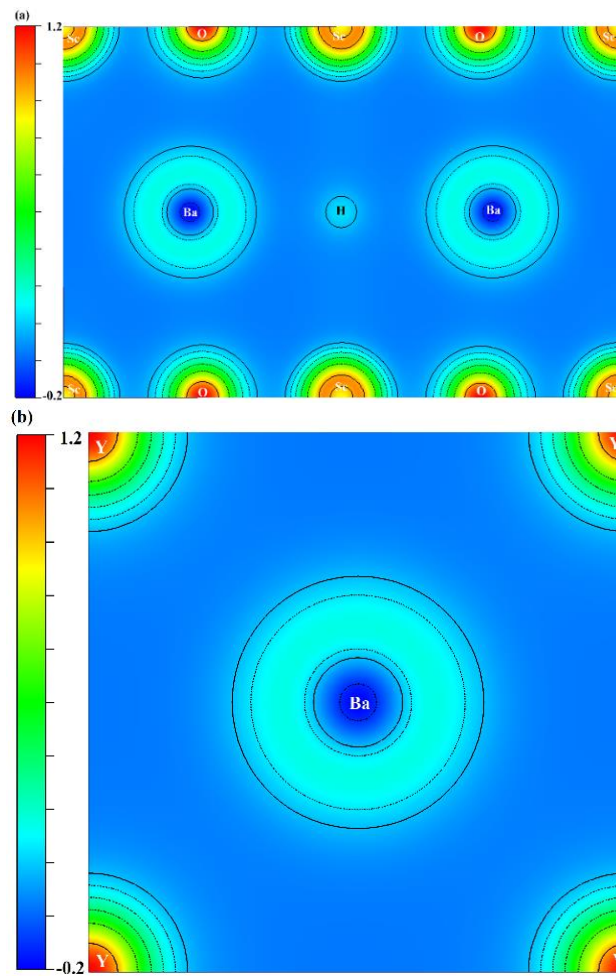


Figure 3.23 The electron-density distributions for (a) $\text{BaScO}_3\text{H}_{0.5}$ and (b) BaYO_3H_3

Table 3.7 The Bader net charges (in units of e per unit cell) for $\text{BaScO}_3\text{H}_{0.5}$ and BaYO_3H_3

Ion	$\text{BaScO}_3\text{H}_{0.5}$	BaYO_3
Ba	6.39	1.46
Sc or Y	8.00	2.09
O	-14.85	-3.22
H	0.45	-0.33

The mechanical properties were investigated for the H bonded compounds. Table 3.8 lists the calculated elastic constants for BaScO₃H_{0.5} and BaYO₃H₃ compounds which satisfy the Born stability criteria. So, these compounds are also mechanically stable. Using the calculated elastic constants, the mechanical properties including bulk modulus, shear modulus, etc. were obtained and have been given in Table 3.9. BaScO₃H_{0.5} has higher bulk modulus, shear modulus and Young's modulus than BaYO₃H₃. These compounds have ionic bonding concluded from the results of Poisson's ratio and G/B ratio that is consistent with the electron-density distributions. It is deduced that BaScO₃H_{0.5} and BaYO₃H₃ are ductile materials.

Table 3.8 The calculated elastic constants (C_{ij} in GPa) for BaScO₃H_{0.5} and BaYO₃H₃

Compound	C ₁₁	C ₁₂	C ₁₃	C ₂₂	C ₂₃	C ₃₃	C ₄₄	C ₅₅	C ₆₆
BaScO ₃ H _{0.5}	174.90	65.60	66.20	220.70	86.80	221.30	38.70	48.40	48.30
BaYO ₃ H ₃	94.40	85.20					25.50		

Table 3.9 Bulk modulus (B in GPa), Shear modulus (G in GPa), Young's modulus (E in GPa), Poisson's ratio (ν), G/B ratio and B/G ratio for BaScO₃H_{0.5} and BaYO₃H₃

Compound	B	G	E	ν	G/B	B/G
BaScO ₃ H _{0.5}	115.80	52.40	136.50	0.30	0.45	2.21
BaYO ₃ H ₃	88.20	13.00	37.10	0.43	0.15	6.78

The anisotropic elastic properties for these compounds have been determined and to save space in this chapter only the results in 3D have been presented. Figure 3.24 shows the direction dependent Young's modulus, linear compressibility, shear modulus, and Poisson's ratio for BaScO₃H_{0.5} and BaYO₃H₃. Only the linear compressibility of BaYO₃H₃ is isotropic and the remaining parameters are anisotropic. Furthermore, the minimum and maximum values for these parameters are listed in Table 3.10.

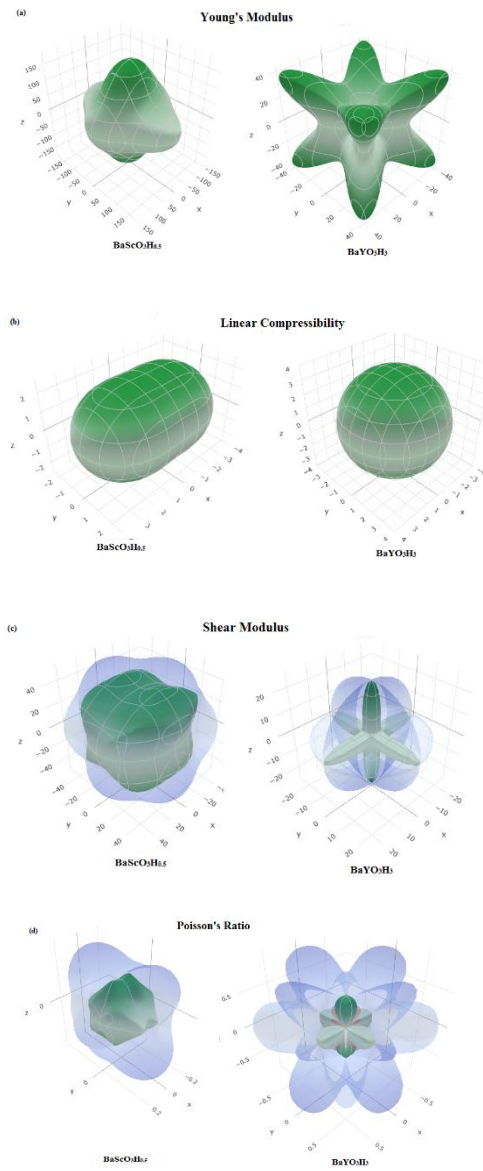


Figure 3.24 The direction dependent (a) Young's modulus, (b) linear compressibility, (c) shear modulus, and (d) Poisson's ratio in 3D for $\text{BaScO}_3\text{H}_{0.5}$ and BaYO_3H_3

Table 3.10 The minimum and maximum values of Young's modulus (E in GPa), linear compressibility (β), shear modulus (G in GPa), and Poisson's ratio(ν) for BaScO₃H_{0.5} and BaYO₃H₃

Compound	E		β		G		ν	
	E _{min}	E _{max}	β _{min}	β _{max}	G _{min}	G _{max}	ν _{min}	ν _{max}
BaScO ₃ H _{0.5}	117.80	176.66	2.40	3.90	38.70	67.10	0.17	0.54
BaYO ₃ H ₃	13.56	69.78	3.78	3.78	4.60	25.50	-0.33	1.20

After the investigation of main physical properties for BaScO₃H_{0.5} and BaYO₃H₃ compounds, the gravimetric hydrogen storage capacity and the hydrogen desorption temperature have been studied which the details of these parameters have been presented in Chapter 2. The gravimetric hydrogen storage capacities were calculated as 0.22 wt.% and 1.09 wt.% for BaScO₃H_{0.5} and BaYO₃H₃, respectively. Furthermore, when the hydrogen is bonded to a material, the desorption temperature is important for the applications of that material. The hydrogen desorption temperatures were determined as 1769.7 K and 599.2 K for BaScO₃H_{0.5} and BaYO₃H₃, respectively.

The presented studies for BaXO₃ compounds show that the crystal structure affects the number of stored H atoms. Even Y is heavier than Sc, BaYO₃H₃ has more gravimetric hydrogen storage capacity and lower hydrogen desorption temperature than BaScO₃H_{0.5} compound.

3.3. Studies for XTiO₃ (X = Mg or Ca)

3.3.1. Structural Optimization for XTiO₃

The studies with BaXO₃ has concluded that the cubic crystal structure provides to store more H atoms. Therefore, XTiO₃ (where X is Mg or Ca) have been investigated in cubic crystal structure as shown in Figure 3.25. The obtained lattice constants have been listed in Table 3.11 with the available literature results. The obtained lattice constants are consistent with the literature. Ca atom has larger atomic radius than Mg

atom, so the lattice constant for CaTiO_3 is larger than MgTiO_3 . In addition, the negative formation energies imply that these compounds are energetically stable and synthesizable. CaTiO_3 has more negative formation energy than MgTiO_3 indicating more stability.

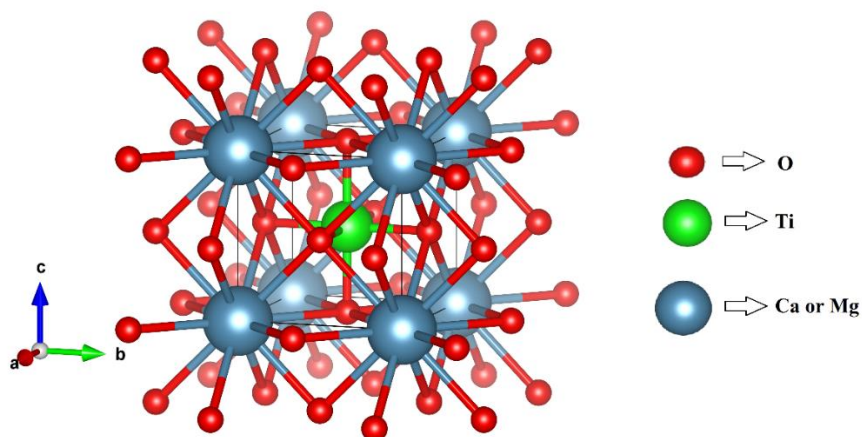


Figure 3.25 The crystal structure of XTiO_3 ($X = \text{Mg}$ or Ca)

Table 3.11 The optimized lattice parameters (a in \AA), the calculated formation energies (ΔE_{For} in eV/atom) and the atomic positions for XTiO_3

Compound	a	ΔE_{For}	Atomic Positions
MgTiO_3	3.73 3.84 ^[95]	-1.37	Mg: 1a (0.00, 0.00, 0.00) Ti: 1b (0.50, 0.50, 0.50) O: 3c (0.00, 0.50, 0.50)
CaTiO_3	3.88 3.89 ^[96] 3.81 ^[97]	-4.53	Ca: 1a (0.00, 0.00, 0.00) Ti: 1b (0.50, 0.50, 0.50) O: 3c (0.00, 0.50, 0.50)

The X-ray diffraction patterns have been given in Figure 3.26 for MgTiO_3 and CaTiO_3 compounds. Both compounds show polycrystalline nature. Moreover, 2θ value of MgTiO_3 is 33.98° in $(-1\ 1\ 0)$ plane and it is 22.92° for CaTiO_3 in $(-1\ 0\ 0)$ plane.

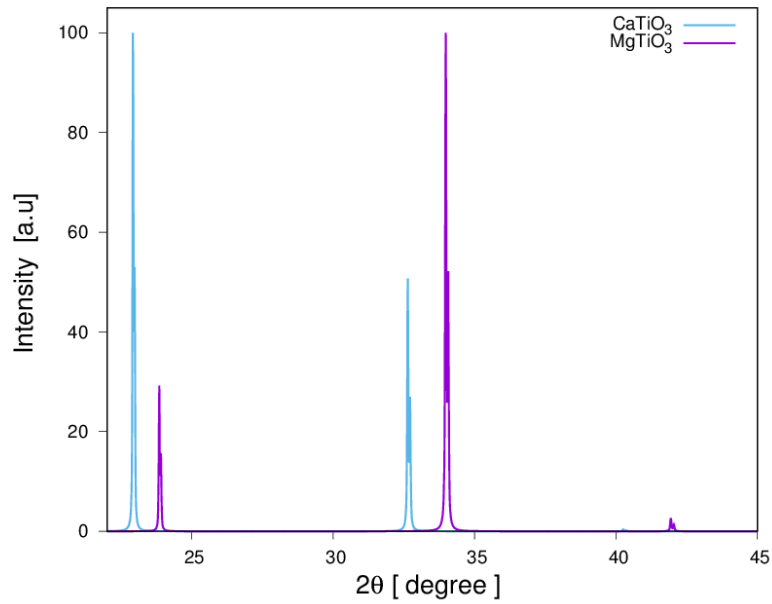


Figure 3.26 X-ray diffraction patterns for $MgTiO_3$ and $CaTiO_3$

3.3.2. Electronic Properties for $XTiO_3$

The band structures and corresponding PDOS have been obtained and shown in Figure 3.27 and Figure 3.28 for $MgTiO_3$. $MgTiO_3$ shows metallic behavior as can be seen from Figure 3.27 and the most significant contribution to the PDOS below the Fermi level comes from the p states of O atoms as can be deduced from Figure 3.28. Unlike from $MgTiO_3$, $CaTiO_3$ has an indirect band gap of 1.89 eV as can be seen from Figure 3.29. Also, Figure 3.30 shows that the most significant contribution to the PDOS below the Fermi level comes from the p states of O atoms similar to $MgTiO_3$.

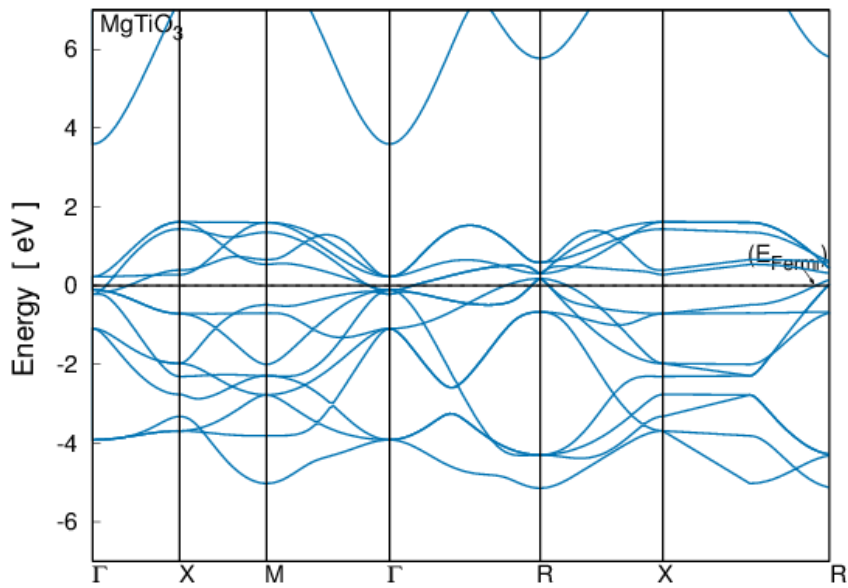


Figure 3.27 The band structure for MgTiO₃

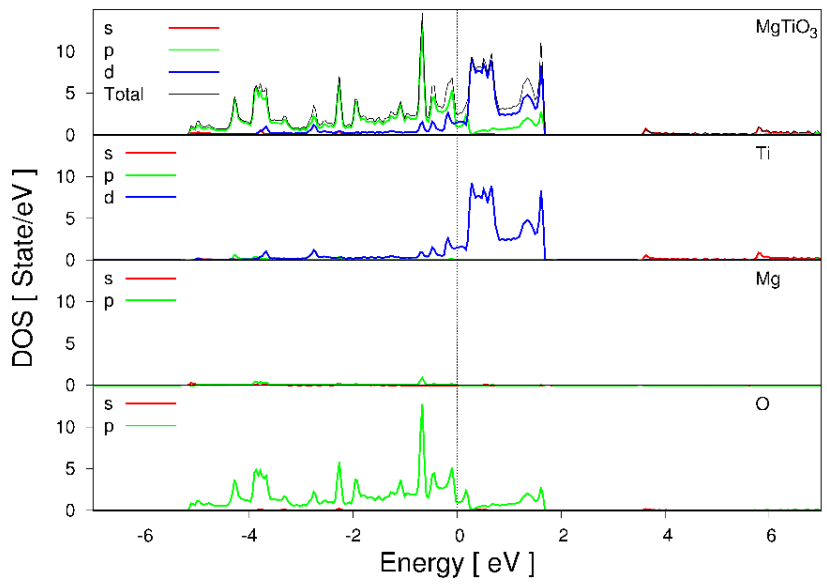


Figure 3.28 The partial density of states for MgTiO₃

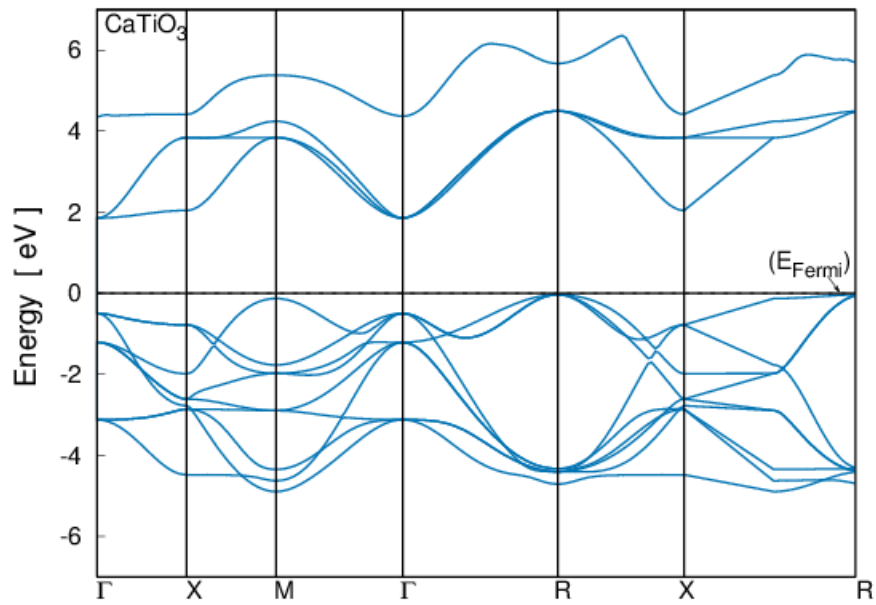


Figure 3.29 The band structure for CaTiO₃

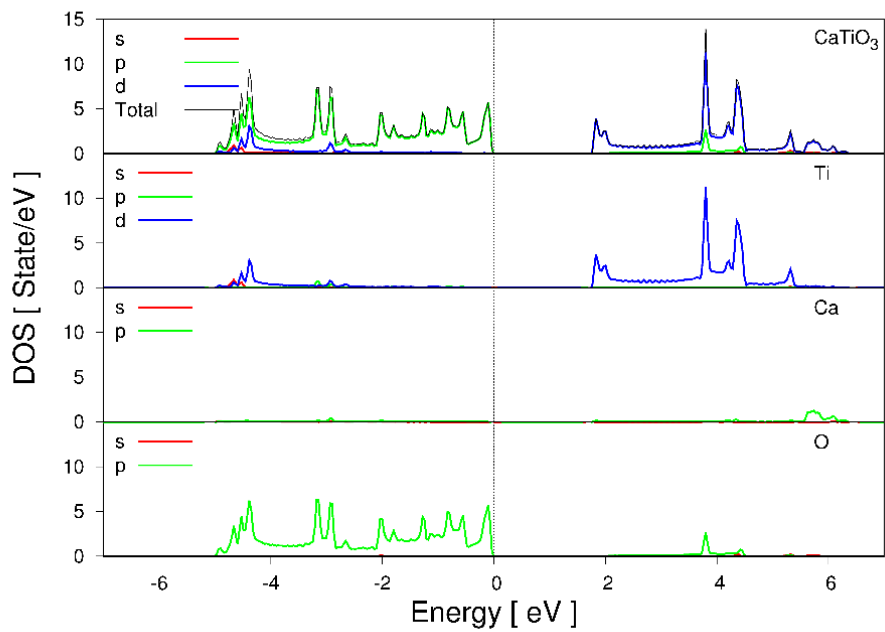


Figure 3.30 The partial density of states for CaTiO₃

The electron-density distributions in (1 0 0) and (1 1 1) planes were obtained for CaTiO₃ as shown in Figure 3.31a and Figure 3.31b, respectively. Also, Table 3.12 lists the Bader partial charges for MgTiO₃ and CaTiO₃ compounds. The charge is transferred away from Mg/Ca atoms and Ti atoms while it is transferred to O atoms. The total Bader net charges are zero for both compounds.

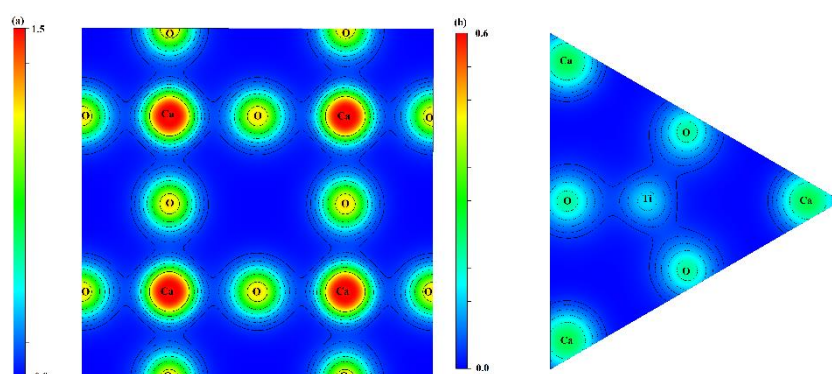


Figure 3.31 The electron-density distributions for CaTiO₃ (a) in (1 0 0) plane and (b) in (1 1 1) plane

Table 3.12 The Bader net charges (in units of *e* per unit cell) for XTiO₃

Ion	MgTiO ₃	CaTiO ₃
Mg or Ca	1.87	1.59
Ti	2.12	2.08
O	-3.99	-3.67

3.3.3. Mechanical Properties for XTiO₃

The elastic constants (C_{ij}) were calculated and have been listed in Table 3.13 for MgTiO₃ and CaTiO₃ compounds. Both compounds are mechanically stable and the obtained results are consistent with the available literature results that are also listed in Table 3.13.

Table 3.13 The calculated elastic constants (C_{ij} in GPa) for $XTiO_3$

Compound	C_{11}	C_{12}	C_{44}
$MgTiO_3$	354.70	53.00	27.90
	339.00 ^[98]	102.00 ^[98]	72.00 ^[98]
$CaTiO_3$	337.20	98.60	97.90
	342.13 ^[96]	93.27 ^[96]	94.47 ^[96]
	356.00 ^[98]	103.00 ^[98]	98.00 ^[98]

Using obtained elastic constants, bulk modulus, shear modulus, Young's modulus, Poisson's ratio, G/B ratio and B/G ratio have been determined for $XTiO_3$ compounds as listed in Table 3.14. The obtained results for $CaTiO_3$ is consistent with the literature while there is no study for $MgTiO_3$ in order to compare the results. $CaTiO_3$ has higher bulk modulus, shear modulus and Young's modulus than $MgTiO_3$. Also, both compounds have ionic bonding. Moreover, $MgTiO_3$ is a ductile material while $CaTiO_3$ is a brittle material.

Table 3.14 Bulk modulus (B in GPa), Shear modulus (G in GPa), Young's modulus (E in GPa), Poisson's ratio (ν), G/B ratio and B/G ratio for $XTiO_3$

Compound	B	G	E	ν	G/B	B/G
$MgTiO_3$	153.50	59.10	157.10	0.33	0.39	2.60
$CaTiO_3$	178.10	105.30	263.80	0.25	0.59	1.69
	176.20 ^[97]	105.50 ^[97]	263.80 ^[97]	0.25 ^[97]	0.60 ^[97]	1.67 ^[97]

The anisotropic elastic properties have been studied and Figure 3.32 and Figure 3.33 show the direction dependent Young's modulus, linear compressibility, shear modulus and Poisson's ratio for $MgTiO_3$ and $CaTiO_3$, respectively. For these compounds, the linear compressibility is found to be isotropic, while the remaining properties are found to be anisotropic. In addition, the minimum and maximum values for these properties have been listed in Table 3.15.

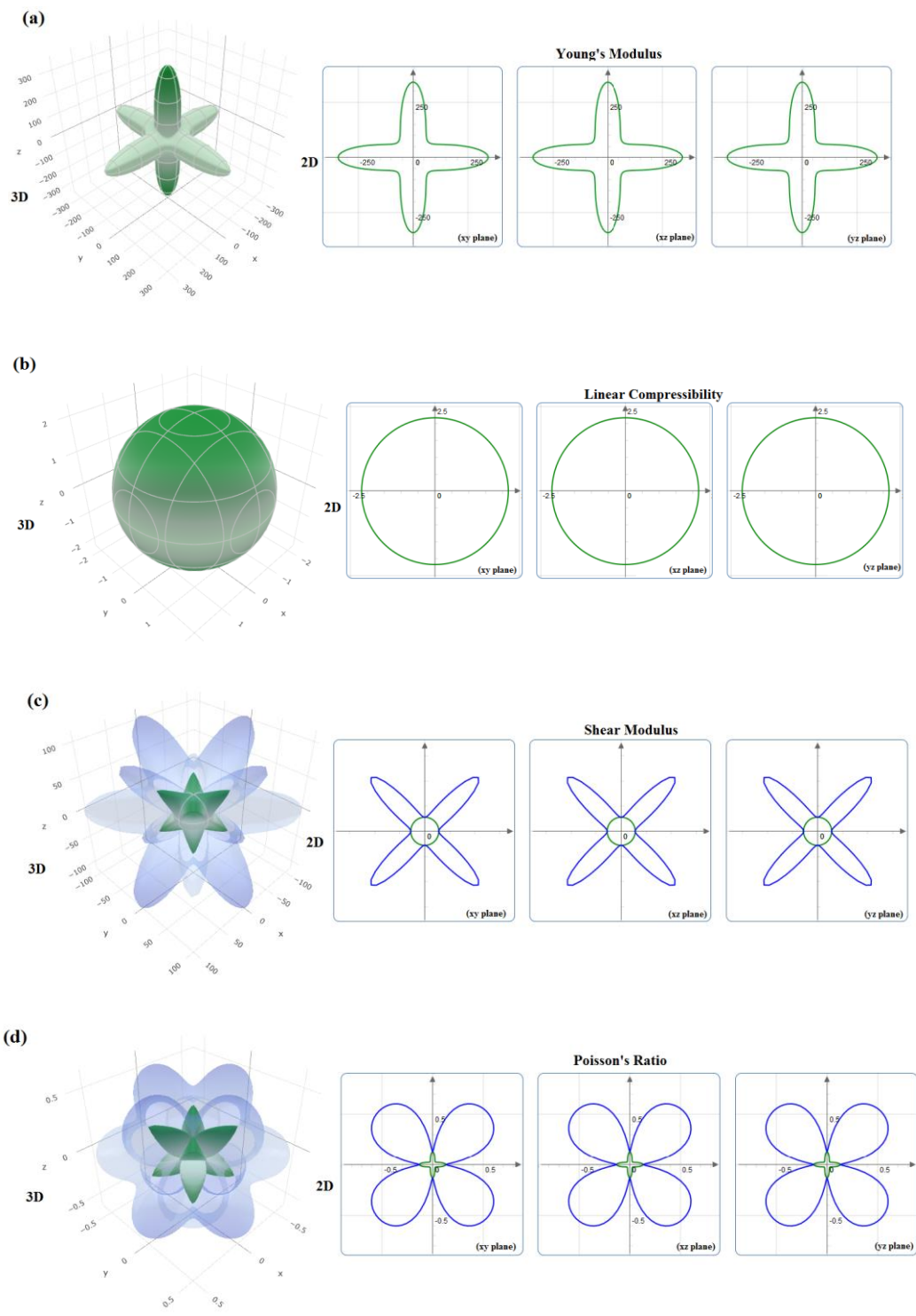


Figure 3.32 The direction dependent (a) Young's modulus, (b) linear compressibility, (c) shear modulus, and (d) Poisson's ratio in 3D for $MgTiO_3$

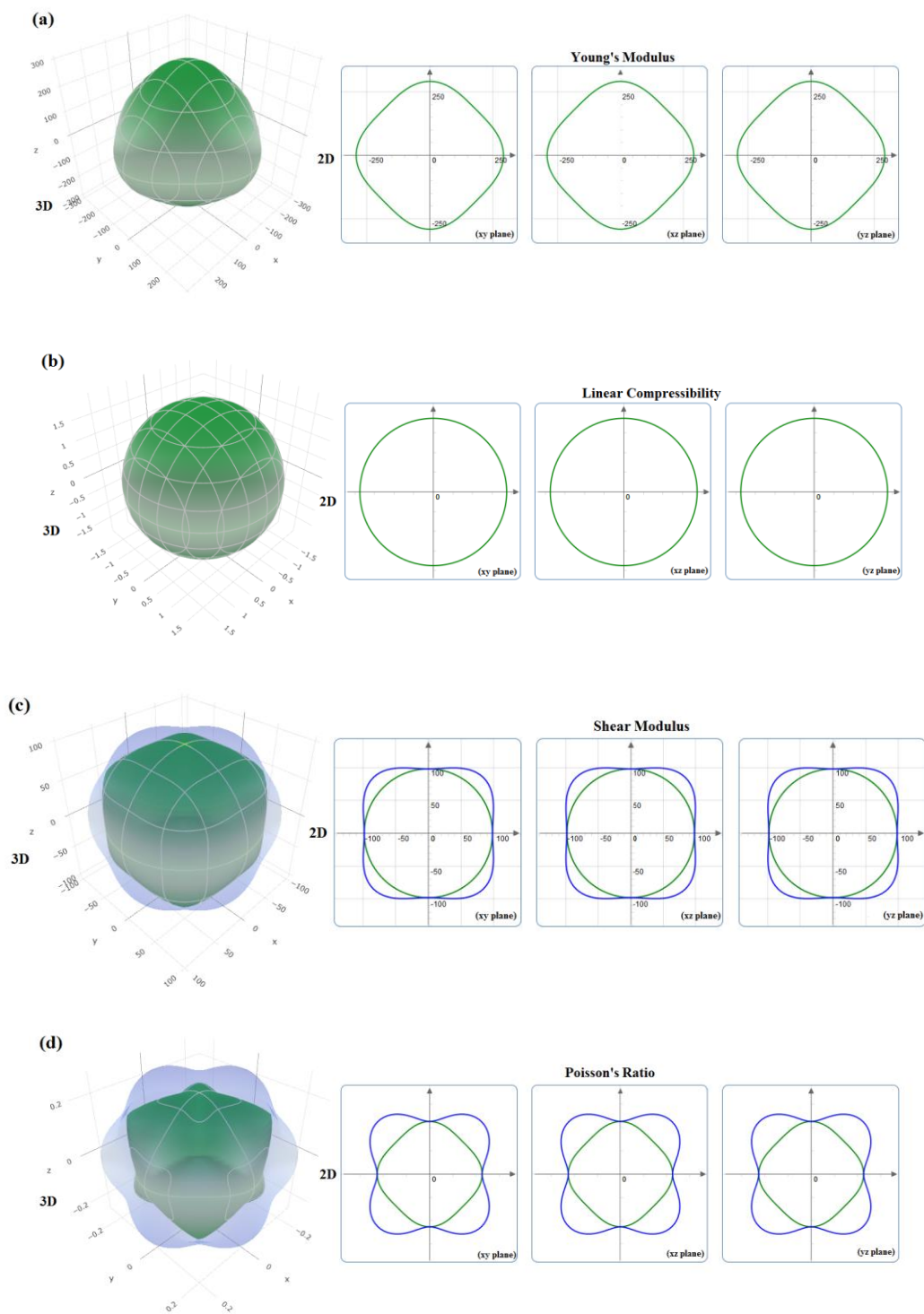


Figure 3.33 The direction dependent (a) Young's modulus, (b) linear compressibility, (c) shear modulus, and (d) Poisson's ratio in 3D for CaTiO_3

Table 3.15 The maximum and minimum values of Young's modulus (E in GPa), linear compressibility (β), shear modulus (G in GPa), and Poisson's ratio (ν) for $XTiO_3$

Compound	E		β		G		ν	
	E_{\min}	E_{\max}	β_{\min}	β_{\max}	G_{\min}	G_{\max}	ν_{\min}	ν_{\max}
MgTiO ₃	78.92	340.92	2.17	2.17	27.90	150.85	0.05	0.75
CaTiO ₃	248.23	292.58	1.87	1.87	97.90	119.30	0.20	0.32

3.3.4. Hydrogen Storage Studies for $XTiO_3$

$XTiO_3$ belongs to space group 221 (Pm-3m) and Mg/Ca atom is at the 1a, Ti atom is at the 1b and O atoms are at the 3c Wyckoff positions. The hydrogen doping positions have been determined as 3d, 6f and 8g for MgTiO₃ and 3d, 6e and 8g for CaTiO₃. Figure 3.34 shows the crystal structures for $XTiO_3H_3$, $XTiO_3H_6$ and $XTiO_3H_8$ compounds. Table 3.16 lists the optimized lattice parameters, the calculated formation energies and the atomic positions. MgTiO₃H₆ and MgTiO₃H₈ are energetically unstable while the remaining of them are stable. Similar to CaTiO₃, the hydrogen bonded structures of CaTiO₃H_x are found to be more stable than MgTiO₃H_x. In addition, the lattice constant enlarges with the increasing number of H atoms in the structures.

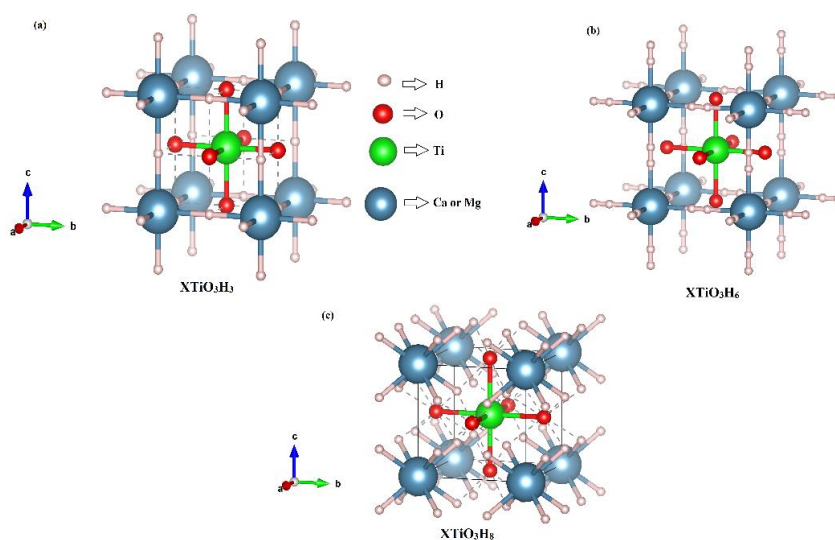


Figure 3.34 The crystal structures of (a) $XTiO_3H_3$, (b) $XTiO_3H_6$ and (c) $XTiO_3H_8$

Table 3.16 The optimized lattice parameters (a in Å), the calculated formation energies (ΔE_{For} in eV/atom) and the atomic positions for $XTiO_3H_x$

Compound	a	ΔE_{For}	Atomic Positions
MgTiO ₃ H ₃	3.93	-0.34	Mg: 1a (0.000, 0.000, 0.000) Ti: 1b (0.500, 0.500, 0.500) O: 3c (0.000, 0.500, 0.500) H: 3d (0.500, 0.000, 0.000)
MgTiO ₃ H ₆	4.31	0.08	Mg: 1a (0.000, 0.000, 0.000) Ti: 1b (0.500, 0.500, 0.500) O: 3c (0.000, 0.500, 0.500) H: 6f (0.088, 0.500, 0.500)
MgTiO ₃ H ₈	4.44	0.49	Mg: 1a (0.000, 0.000, 0.000) Ti: 1b (0.500, 0.500, 0.500) O: 3c (0.000, 0.500, 0.500) H: 8g (0.267, 0.267, 0.267)
CaTiO ₃ H ₃	4.07	-1.68	Ca: 1a (0.00, 0.000, 0.000) Ti: 1b (0.500, 0.500, 0.500) O: 3c (0.000, 0.500, 0.500) H: 3d (0.500, 0.000, 0.000)
CaTiO ₃ H ₆	4.35	-1.12	Ca: 1a (0.000, 0.000, 0.000) Ti: 1b (0.500, 0.500, 0.500) O: 3c (0.000, 0.500, 0.500) H: 6e (0.421, 0.000, 0.000)
CaTiO ₃ H ₈	4.56	-0.13	Ca: 1a (0.000, 0.000, 0.000) Ti: 1b (0.500, 0.500, 0.500) O: 3c (0.000, 0.500, 0.500) H: 8g (0.270, 0.270, 0.270)

The X-ray diffraction patterns for the energetically stable compounds (MgTiO₃H₃, CaTiO₃H₃, CaTiO₃H₆, and CaTiO₃H₈) have been studied and shown in Figure 3.35. As can be seen from the figure, all compounds show polycrystalline nature. The 2θ value of MgTiO₃H₃ is 32.21° in (-1 -1 0) plane. Also, the 2θ values in (-1, 0, 0) plane are 21.80°, 20.39° and 19.46° for CaTiO₃H₃, CaTiO₃H₆, and CaTiO₃H₈, respectively. As the number of bonded hydrogen atoms increases, the 2θ value decreases for CaTiO₃H_x compounds.

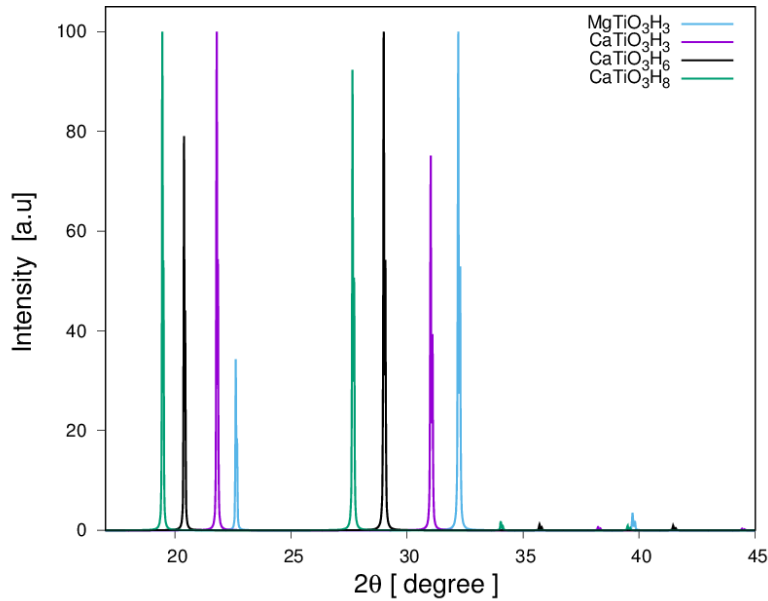


Figure 3.35 X-ray diffraction patterns for $MgTiO_3H_3$, $CaTiO_3H_3$, $CaTiO_3H_6$, and $CaTiO_3H_8$

The band structure and corresponding PDOS have been studied for the energetically stable compounds. Figure 3.36 and Figure 3.37 show the band structure and corresponding PDOS for $MgTiO_3H_3$ that shows metallic character. Also, the most significant contribution to the PDOS above the Fermi level comes from the d states of Ti as can be seen from Figure 3.37. For $CaTiO_3H_x$ compounds, the band structure for $CaTiO_3H_6$ has been shown in Figure 3.38 that has an indirect band gap of 1.23 eV. In addition, Figure 3.39 shows the partial density of states for $CaTiO_3H_x$ compounds and this figure clearly shows that $CaTiO_3H_3$ and $CaTiO_3H_8$ show metallic character while $CaTiO_3H_6$ show semiconducting character.

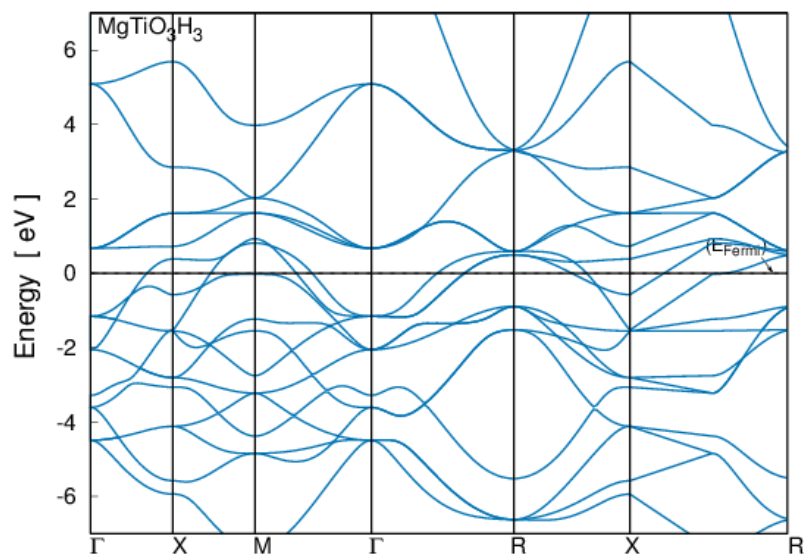


Figure 3.36 The band structure for MgTiO₃H₃

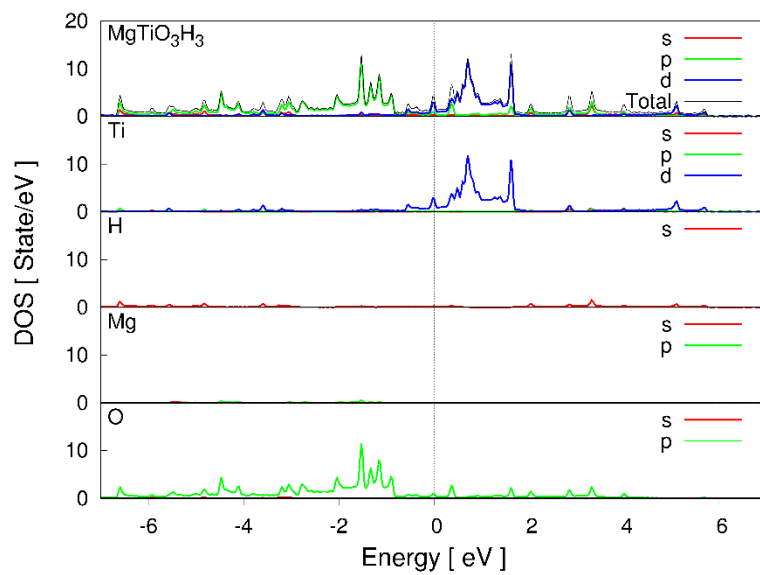


Figure 3.37 The partial density of states for MgTiO₃H₃

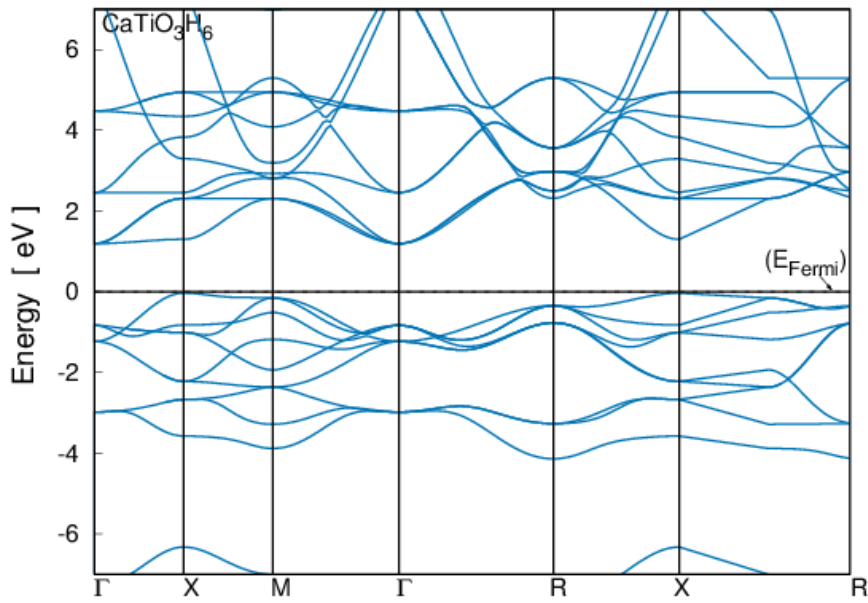


Figure 3.38 The band structure for CaTiO_3H_6

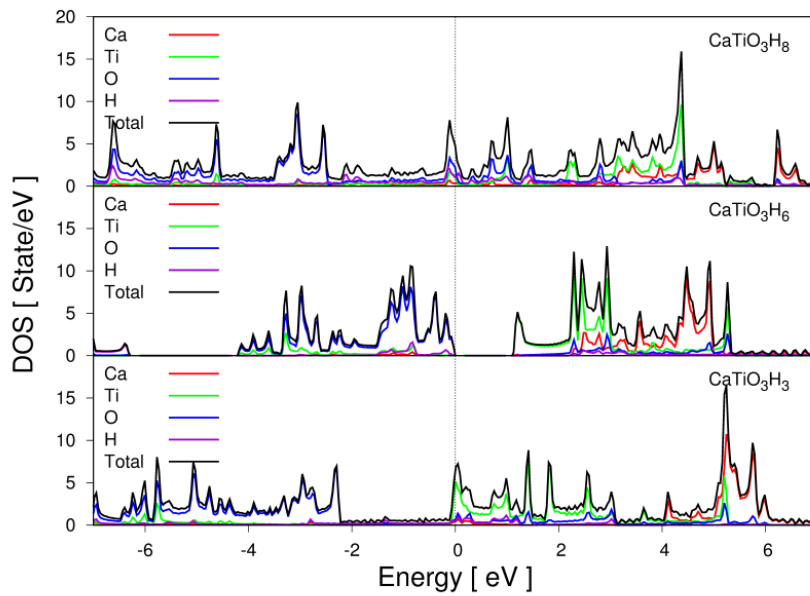


Figure 3.39 The partial density of states for CaTiO_3H_3 , CaTiO_3H_6 and CaTiO_3H_8

The electron-density distributions for CaTiO_3H_3 , CaTiO_3H_6 and CaTiO_3H_8 were obtained in (1 0 0) plane and in (1 1 1) plane and have been given in Figure 3.40. As can be seen from the figures, the H atoms affect the bonding in these compounds. In addition, the Bader net charges have been listed in Table 3.17. All the total Bader net charges are found to be zero. Similar to XTiO_3 compounds, the charge is transferred away from Mg/Ca and Ti atoms while it is transferred to O and also H atoms.

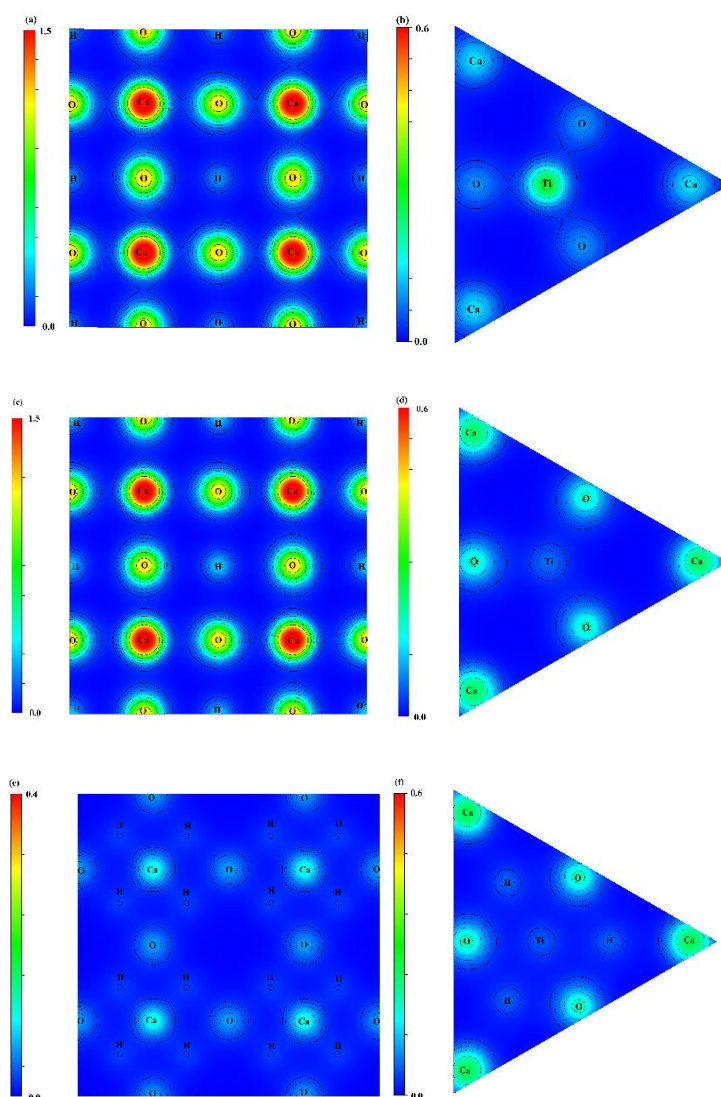


Figure 3.40 The electron-density distributions for CaTiO_3H_3 (a) in (1 0 0) plane and (b) in (1 1 1) plane, for CaTiO_3H_6 (c) in (1 0 0) plane and (d) in (1 1 1) plane, for CaTiO_3H_8 (e) in (1 0 0) plane and (f) in (1 1 1) plane

Table 3.17 The Bader net charges (in units of e per unit cell) for $XTiO_3H_x$

Ion	MgTiO ₃ H ₃	CaTiO ₃ H ₃	CaTiO ₃ H ₆	CaTiO ₃ H ₈
Mg or Ca	1.90	1.44	1.43	1.40
Ti	2.12	2.16	2.06	1.69
O	-3.23	-3.17	-3.46	-2.37
H	-0.79	-0.43	-0.03	-0.72

The elastic constants (C_{ij}) were calculated to determine the mechanical stability of these compounds. Table 3.18 lists the obtained values and as can be deduced from the table, only CaTiO₃H₆ compound is found to be as mechanically stable. In addition, the mechanical properties including bulk modulus, shear modulus, etc. have been determined as listed in Table 3.19. CaTiO₃H₆ has ionic bonding and it is a ductile material.

Table 3.18 The calculated elastic constants (C_{ij} in GPa) for $XTiO_3H_x$

Compound	C ₁₁	C ₁₂	C ₄₄
MgTiO ₃ H ₃	117.90	150.60	22.70
CaTiO ₃ H ₃	53.20	183.40	14.20
CaTiO ₃ H ₆	261.50	22.50	33.60
CaTiO ₃ H ₈	40.90	103.30	-16.20

Table 3.19 Bulk modulus (B in GPa), Shear modulus (G in GPa), Young's modulus (E in GPa), Poisson's ratio (ν), G/B ratio and B/G ratio for CaTiO₃H₆

B	G	E	ν	G/B	B/G
102.10	57.50	145.20	0.26	0.56	1.78

The anisotropic elastic properties for CaTiO₃H₆ were obtained and have been shown in Figure 3.41 for Young's modulus, linear compressibility, shear modulus and Poisson's ratio. Only linear compressibility is isotropic and the other properties are anisotropic for CaTiO₃H₆. In addition, the minimum and maximum values for these parameters have been listed in Table 3.20.

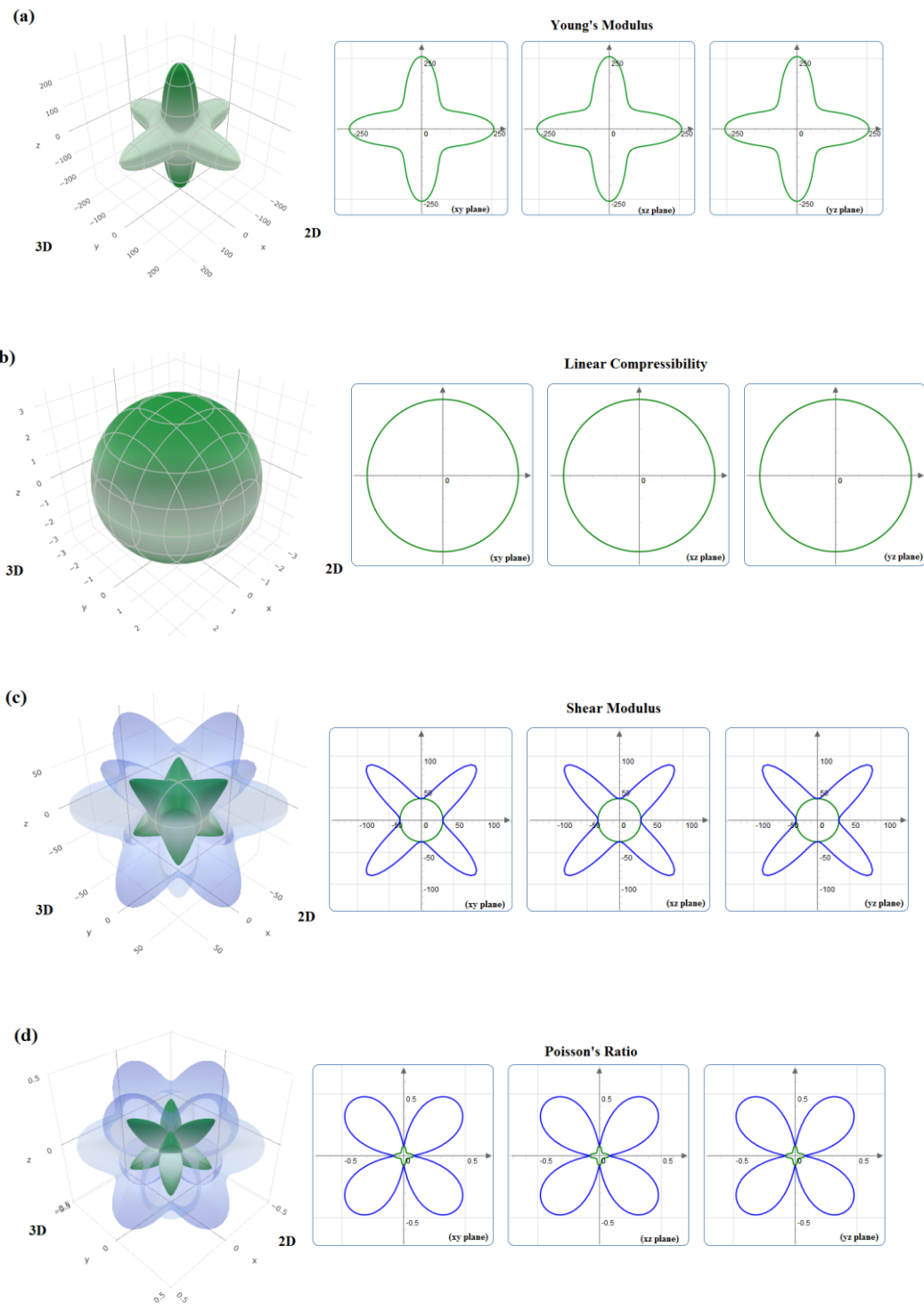


Figure 3.41 The direction dependent (a) Young's modulus, (b) linear compressibility, (c) shear modulus, and (d) Poisson's ratio in 3D for CaTiO_3H_6

Table 3.20 The minimum and maximum values of Young's modulus (E in GPa), linear compressibility (β), shear modulus (G in GPa), and Poisson's ratio (ν) for CaTiO_3H_6

E		β		G		ν	
E_{min}	E_{max}	β_{min}	β_{max}	G_{min}	G_{max}	ν_{min}	ν_{max}
90.83	257.93	3.27	3.27	33.60	119.37	0.03	0.61

The hydrogen storage studies for XTiO_3 compounds have been started with six compounds and the energetically and mechanical stability conditions have eliminated five of them. The gravimetric hydrogen storage capacity has been calculated as 4.27 wt.% and the hydrogen desorption temperature has been determined as 827.1 K for CaTiO_3H_6 compound. As a conclusion of these studies, it has been deduced that the cubic crystal structure provides to store more hydrogen atoms and choosing light weight elements increases the gravimetric hydrogen storage capacity.

CHAPTER 4

HYDROGEN STORAGE STUDIES FOR ANTI-PEROVSKITE MATERIALS

4.1. Introduction

The anti-perovskite materials having X_3AB formula, generally crystallize in the cubic crystal structure [99] which is the preferred structure as concluded in Chapter 3 due to storing more hydrogen atoms. Ca_3XH where X is C or N anti-perovskite compounds have been studied for structural, electronic, mechanical and hydrogen storage properties and these studies will be presented in this chapter. In addition, more hydrogen atoms have been bonded to these structures to enhance their hydrogen storage capacities. Some part of the studies for Ca_3XH have been prepared to submit to Journal of Physics: Condensed Matter with the title of “Investigation of Ca_3CH_x ($x=1, 4, 7$) Anti-Perovskite Compounds for Hydrogen Storage Applications”.

4.2. Studies for Ca_3XH (X= C or N)

4.2.1. Structural Optimization for Ca_3XH

In Ca_3XH compounds, Ca atoms are anions while X and H atoms are cations. Figure 4.1 shows the crystal structure for Ca_3XH and Table 4.1 lists the obtained lattice constants and the formation energies. Ca_3XH compounds are hypothetical and there is no study to compare the obtained results. As the atomic radius of C is larger than the atomic radius of N, the lattice constant for Ca_3CH is larger than Ca_3NH . Moreover, Ca_3NH has more negative formation energy, so it is more stable than Ca_3CH .

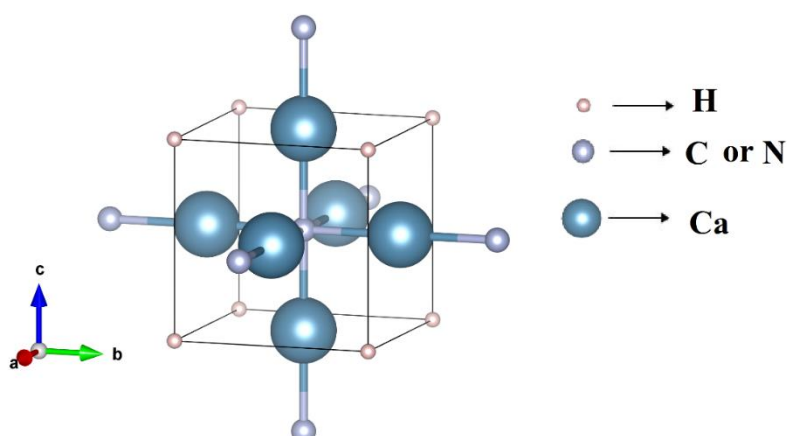


Figure 4.1 The crystal structure of Ca_3XH

Table 4.1 The lattice constants (a in \AA), the calculated formation energies (ΔE_{For} in eV/atom) and the atomic positions for Ca_3XH

Compound	a	ΔE_{For}	Atomic Positions
Ca_3CH	5.02	-2.56	Ca: 3c (0.000, 0.500, 0.500) C: 1b (0.500, 0.500, 0.500) H: 1a (0.000, 0.000, 0.000)
Ca_3NH	4.84	-4.00	Ca: 3c (0.000, 0.500, 0.500) N: 1b (0.500, 0.500, 0.500) H: 1a (0.000, 0.000, 0.000)

Before further present the physical properties of these compounds, hydrogen doping studies will be detailed here. Ca_3XH belong to 221 (Pm-3m) space group where Ca atoms are at 3c, X atom is at 1b and H atom is at 1a Wyckoff positions. The possible hydrogen doping positions were determined as 3d, 6e, 8g and 3d+6e. Using these determined positions, Ca_3XH_4 , Ca_3XH_7 , Ca_3XH_9 , and $\text{Ca}_3\text{XH}_{10}$ have been obtained and the crystal structures for these compounds have been shown in Figure 4.2. The optimized lattice parameters, the calculated formation energies and the atomic positions have been listed in Table 4.2. All these compounds have negative formation energies, so they are energetically stable compounds. Except $\text{Ca}_3\text{XH}_{10}$, the formation energy has more positive values with the increasing number of hydrogen atoms in the

structure. Moreover, the lattice constant enlarges with the increasing number of hydrogen atoms except $\text{Ca}_3\text{CH}_{10}$.

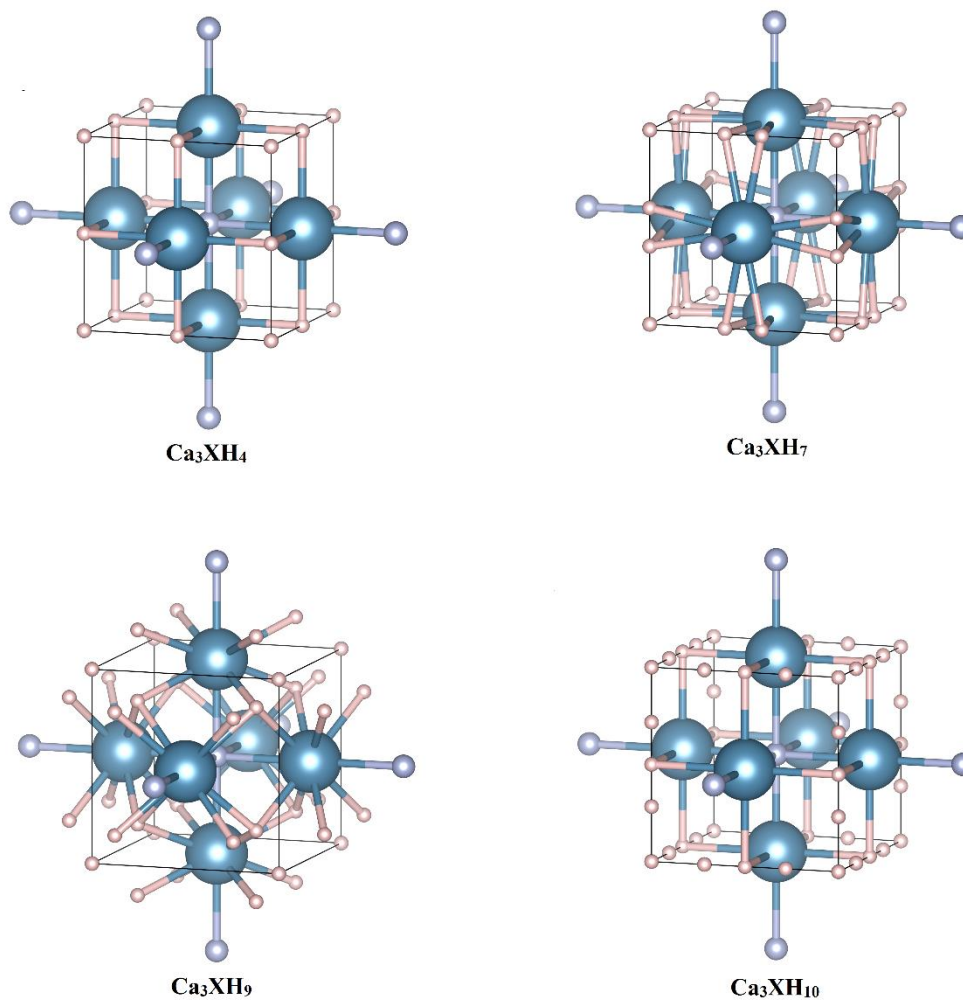


Figure 4.2 The crystal structures for Ca_3XH_4 , Ca_3XH_7 , Ca_3XH_9 , and $\text{Ca}_3\text{XH}_{10}$ compounds

Table 4.2 The lattice constants (a in \AA), the calculated formation energies (ΔE_{For} in eV/atom) and the atomic positions for Ca_3XH_4 , Ca_3XH_7 , Ca_3XH_9 , and $\text{Ca}_3\text{XH}_{10}$

Compound	a	ΔE_{For}	Atomic Positions
Ca_3CH_4	4.92	-1.60	Ca: 3c (0.000, 0.500, 0.500) C: 1b (0.500, 0.500, 0.500) H ₁ : 1a (0.000, 0.000, 0.000) H ₂ : 3d (0.500, 0.000, 0.000)
Ca_3CH_7	5.04	-1.11	Ca: 3c (0.000, 0.500, 0.500) C: 1b (0.500, 0.500, 0.500) H ₁ : 1a (0.000, 0.000, 0.000) H ₂ : 6e (0.584, 0.000, 0.000)
Ca_3CH_9	5.40	-0.63	Ca: 3c (0.000, 0.500, 0.500) C: 1b (0.500, 0.500, 0.500) H ₁ : 1a (0.000, 0.000, 0.000) H ₂ : 8g (0.294, 0.294, 0.294)
$\text{Ca}_3\text{CH}_{10}$	5.06	-0.72	Ca: 3c (0.000, 0.500, 0.500) C: 1b (0.500, 0.500, 0.500) H ₁ : 1a (0.000, 0.000, 0.000) H ₂ : 3d (0.500, 0.000, 0.000) H ₃ : 6e (0.708, 0.000, 0.000)
Ca_3NH_4	4.81	-1.94	Ca: 3c (0.000, 0.500, 0.500) N: 1b (0.500, 0.500, 0.500) H ₁ : 1a (0.000, 0.000, 0.000) H ₂ : 3d (0.500, 0.000, 0.000)
Ca_3NH_7	4.83	-1.72	Ca: 3c (0.000, 0.500, 0.500) N: 1b (0.500, 0.500, 0.500) H ₁ : 1a (0.000, 0.000, 0.000) H ₂ : 6e (0.402, 0.000, 0.000)
Ca_3NH_9	4.95	-1.12	Ca: 3c (0.000, 0.500, 0.500) N: 1b (0.500, 0.500, 0.500) H ₁ : 1a (0.000, 0.000, 0.000) H ₂ : 8g (0.817, 0.817, 0.817)
$\text{Ca}_3\text{NH}_{10}$	4.96	-1.22	Ca: 3c (0.000, 0.500, 0.500) N: 1b (0.500, 0.500, 0.500) H ₁ : 1a (0.000, 0.000, 0.000) H ₂ : 3d (0.500, 0.000, 0.000) H ₃ : 6e (0.717, 0.000, 0.000)

The X-ray diffraction patterns for these anti-perovskite structures were obtained and have been given in Figure 4.3 for Ca_3CH_x compounds and in Figure 4.4 for Ca_3NH_x compounds. For both C and N containing anti-perovskite structures, the bonded hydrogen atoms do not change the pattern significantly.

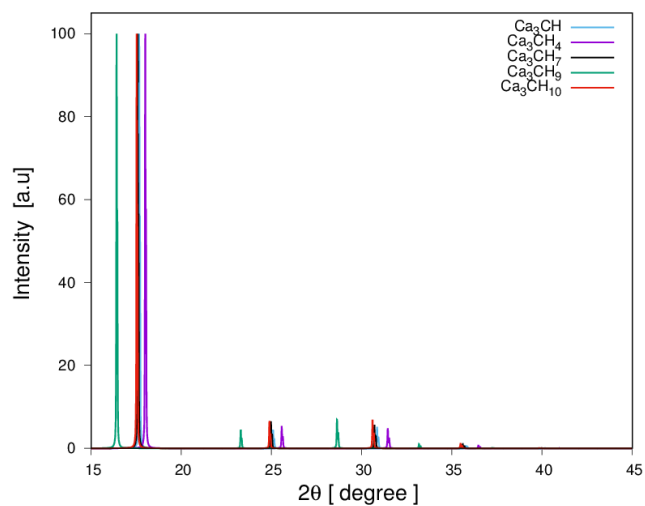


Figure 4.3 X-ray diffraction patterns for Ca_3CH_x ($X= 1, 4, 7, 9, 10$)

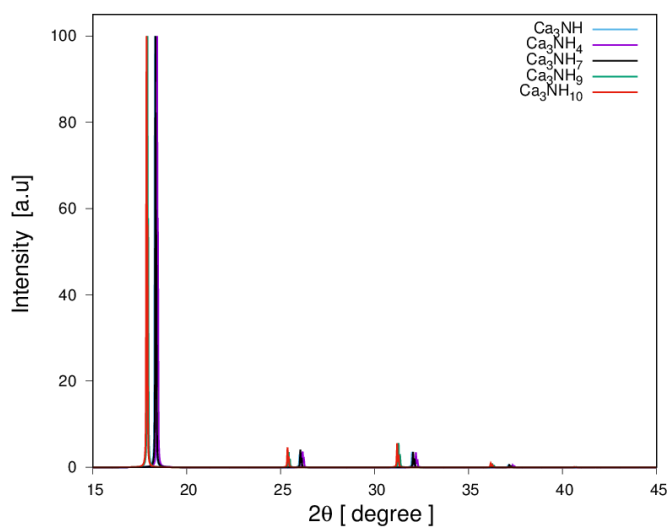


Figure 4.4 X-ray diffraction patterns for Ca_3NH_x ($X= 1, 4, 7, 9, 10$)

The gravimetric hydrogen storage capacities and the hydrogen desorption temperature for these compounds have been obtained and listed in Table 4.3. The C and N containing compounds have similar gravimetric hydrogen storage capacities where these structures have higher capacities with the increasing number of H atoms in the structures. Moreover, the lowest hydrogen desorption temperature has been obtained for Ca_3CH_9 compound as 468.4 K.

Table 4.3 The gravimetric hydrogen capacities (Cwt%) and the hydrogen desorption temperatures (T in K) for Ca_3XH , Ca_3XH_4 , Ca_3XH_7 , Ca_3XH_9 , and $\text{Ca}_3\text{XH}_{10}$

Compound	C_{wt%}	T
Ca_3CH	0.76	1890.8
Ca_3CH_4	2.96	1183.7
Ca_3CH_7	5.08	817.8
Ca_3CH_9	6.43	468.4
$\text{Ca}_3\text{CH}_{10}$	7.10	534.0
Ca_3NH	0.75	2952.2
Ca_3NH_4	2.92	1432.6
Ca_3NH_7	5.00	1269.7
Ca_3NH_9	6.34	825.4
$\text{Ca}_3\text{NH}_{10}$	7.00	899.5

4.2.2. Mechanical Properties for Ca_3XH

The elastic constants (C_{ij}) for Ca_3XH and their hydrides have been calculated to determine the mechanical stability of these compounds as listed in Table 4.4. As can be deduced from the table, the mechanically stable compounds are as follows: Ca_3CH , Ca_3CH_4 , Ca_3CH_7 , Ca_3NH , and Ca_3NH_4 . So, the mechanical stability conditions eliminate five of these structures.

Table 4.4 The elastic constants (C_{ij} in GPa) for Ca_3XH , Ca_3XH_4 , Ca_3XH_7 , Ca_3XH_9 , and Ca_3XH_{10}

Compound	C_{11}	C_{12}	C_{44}
Ca_3CH	89.00	11.00	17.20
Ca_3CH_4	56.30	44.80	29.30
Ca_3CH_7	78.40	26.10	21.00
Ca_3CH_9	62.20	15.60	-3.00
Ca_3CH_{10}	44.20	61.50	16.00
Ca_3NH	82.00	21.90	11.70
Ca_3NH_4	117.20	28.40	37.80
Ca_3NH_7	50.20	53.30	27.20
Ca_3NH_9	71.80	56.00	-13.40
Ca_3NH_{10}	-389.10	282.60	-32.80

Using calculated elastic constants, some mechanical properties including bulk modulus, shear modulus, etc. were determined and have been listed in Table 4.5. Ca_3NH_4 has the highest bulk modulus, shear modulus and Young's modulus among the mechanically stable compounds. In addition, these compounds have ionic bonding according to the results of the Poisson's ratio and G/B ratio. Also, Ca_3CH_4 , Ca_3CH_7 and Ca_3NH are ductile while Ca_3NH_4 and Ca_3CH and are brittle materials.

Table 4.5 Bulk modulus (B in GPa), Shear modulus (G in GPa), Young's modulus (E in GPa), Poisson's ratio (ν), G/B ratio and B/G ratio for Ca_3XH , Ca_3XH_4 , and Ca_3XH_7

Compound	B	G	E	ν	G/B	B/G
Ca_3CH	37.00	24.00	59.20	0.23	0.65	1.54
Ca_3CH_4	48.60	15.40	41.70	0.36	0.32	3.16
Ca_3CH_7	45.30	22.80	58.20	0.28	0.52	1.91
Ca_3NH	41.90	17.20	45.30	0.32	0.41	2.44
Ca_3CH_4	58.00	40.20	97.90	0.22	0.69	1.44

The anisotropic elastic properties have been studied and the direction dependent Young's modulus, linear compressibility, shear modulus and Poisson's ratio have been shown in Figure 4.5 and Figure 4.6 for Ca_3CH_x and Ca_3NH_x compounds, respectively. In order to save space in this section, only the 3D figures have been

presented. The linear compressibility is found to be isotropic while the remaining properties are anisotropic for all compounds. Moreover, Table 4.6 list the minimum and maximum values for these parameters.

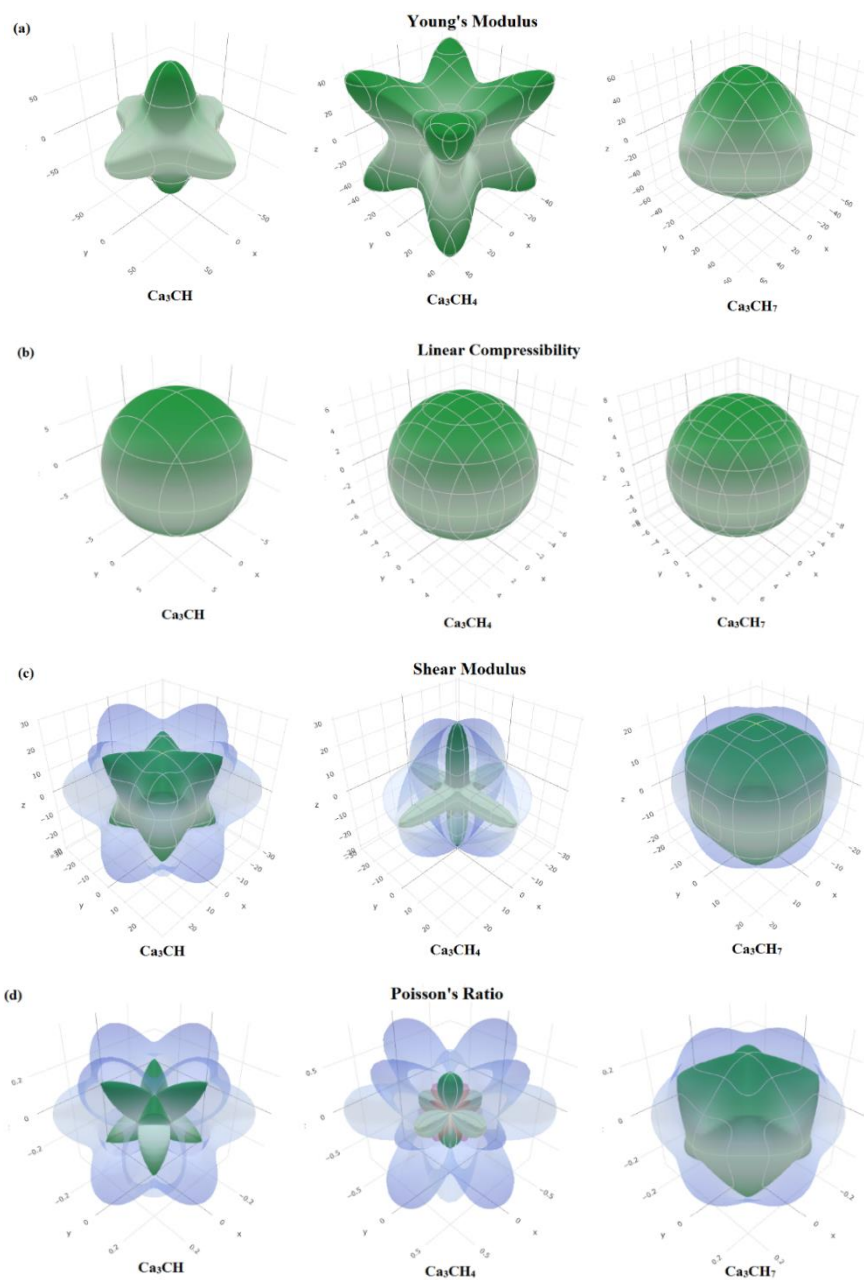


Figure 4.5 The direction dependent (a) Young's modulus, (b) linear compressibility, (c) shear modulus, and (d) Poisson's ratio in 3D for Ca_3CH , Ca_3CH_4 and Ca_3CH_7

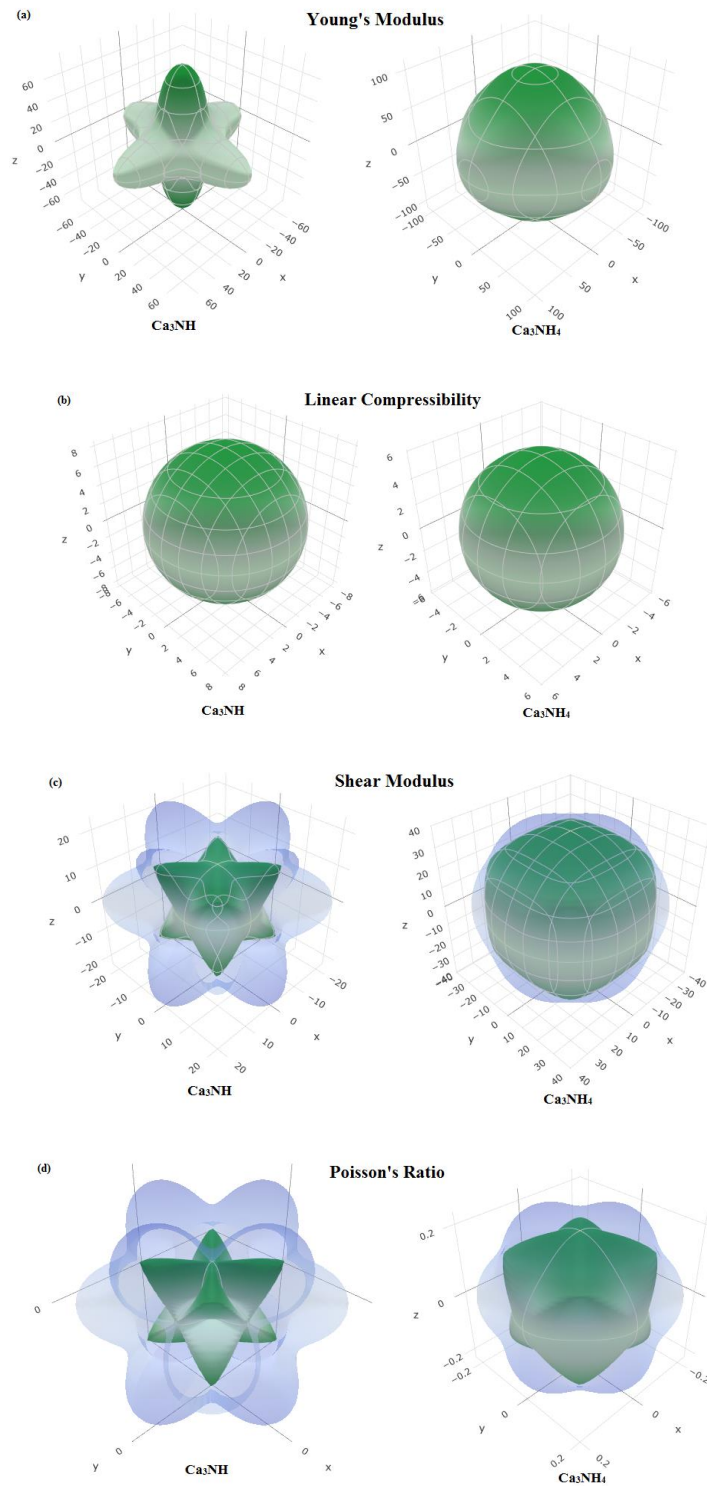


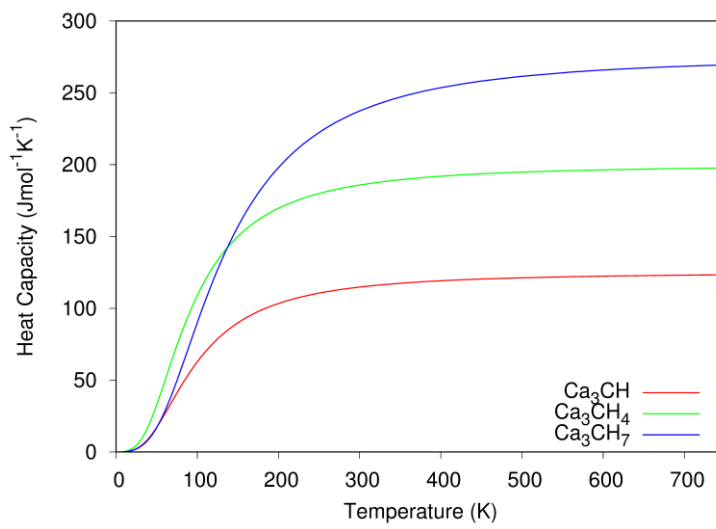
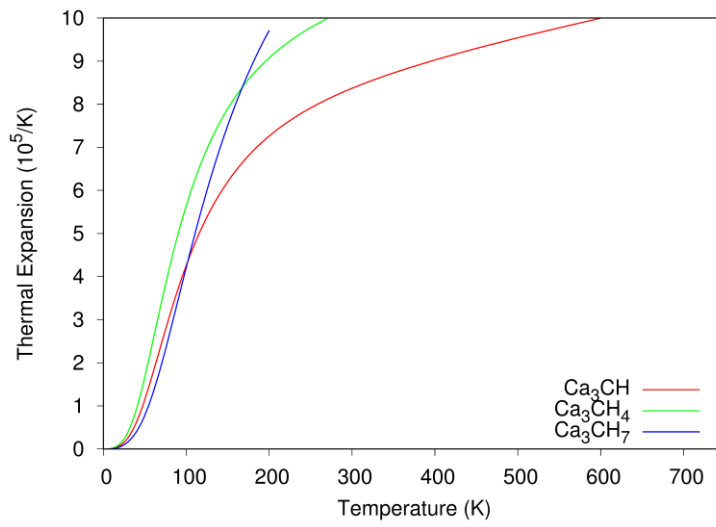
Figure 4.6 The direction dependent (a) Young's modulus, (b) linear compressibility, (c) shear modulus, and (d) Poisson's ratio in 3D for Ca_3NH and Ca_3NH_4

Table 4.6 The minimum and maximum values of Young's modulus (E in GPa), linear compressibility (β), shear modulus (G in GPa), and Poisson's ratio (ν) for Ca_3XH , Ca_3XH_4 , and Ca_3XH_7

Compound	E		β		G		ν	
	E_{min}	E_{max}	β_{min}	β_{max}	G_{min}	G_{max}	ν_{min}	ν_{max}
Ca_3CH	44.68	86.58	9.01	9.01	12.70	39.00	-0.33	1.06
Ca_3CH_4	16.60	73.20	6.85	6.85	5.75	29.30	0.17	0.26
Ca_3CH_7	54.27	65.36	7.66	7.66	21.00	26.15	0.22	0.35
Ca_3NH	32.11	72.77	7.95	7.95	11.70	30.05	0.11	0.60
Ca_3NH_4	93.16	106.12	5.74	5.74	37.80	44.40	0.18	0.27

4.2.3. Thermo-elastic Properties for Ca_3XH

The thermal properties for Ca_3XH , Ca_3XH_4 and Ca_3XH_7 have been studied using Quasi-harmonic Debye model [77]. Figure 4.7 and Figure 4.8 show the thermal expansion, heat capacity at constant volume, entropy and free energy at 0 GPa pressure for Ca_3CH_x and Ca_3NH_x , respectively. As can be seen from the figures, the thermal expansion, heat capacity and entropy increase while free energy decreases with the increasing temperature. For the heat capacity, it reaches a constant called Dulong-Petit limit at high temperatures. The Dulong-Petit limit equals to $3nR$ where n is number of atoms in the structure and R is the ideal gas constant, so the Dulong-Petit limits are different for different structures in the figures. In literature, there is no study for these properties. Therefore, the obtained results could not be compared.



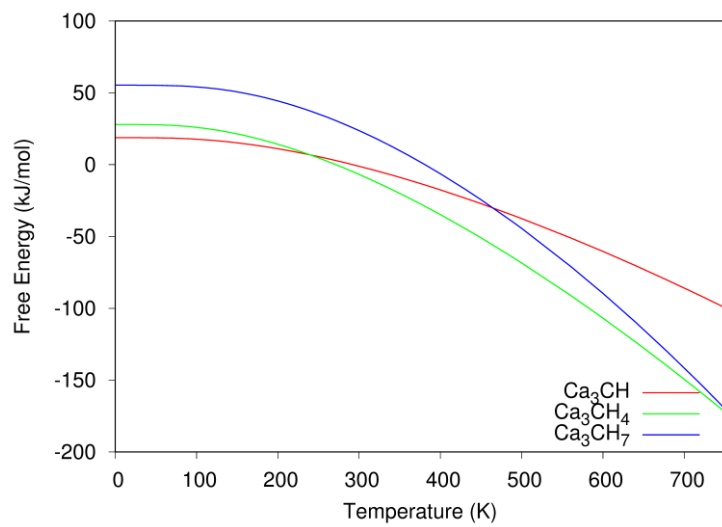
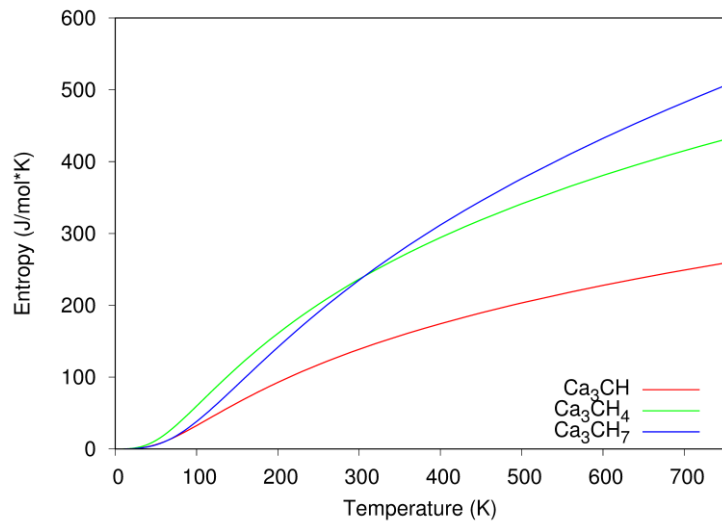
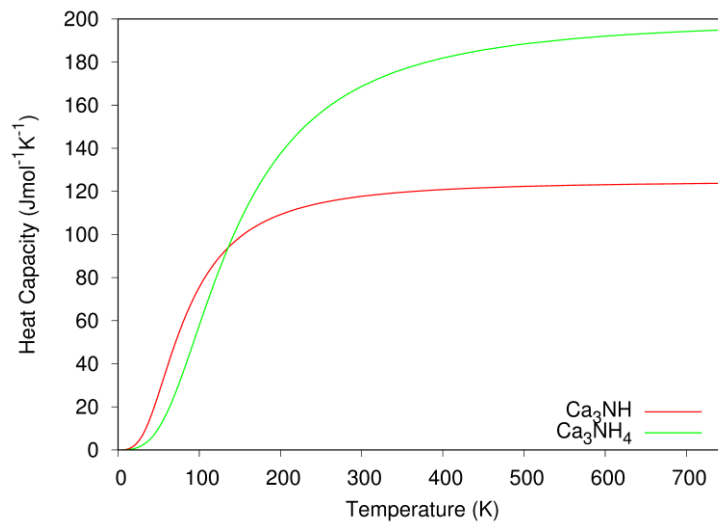
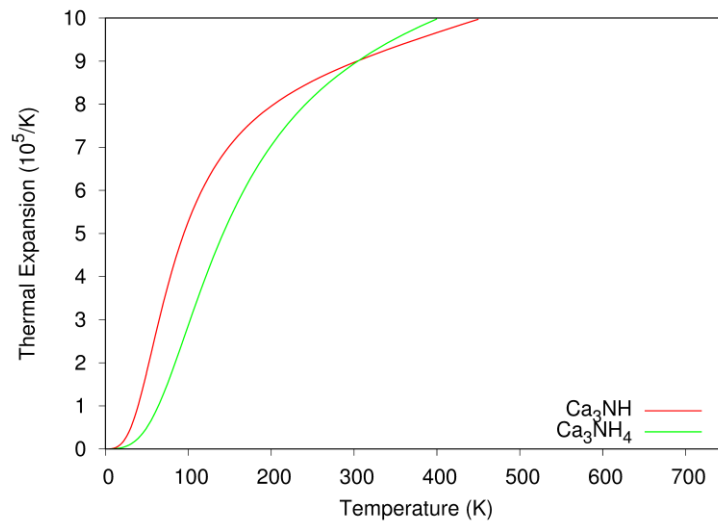


Figure 4.7 The thermal expansion, heat capacity at constant volume, entropy and free energy as a function of temperature at 0 GPa pressure for Ca_3CH_x



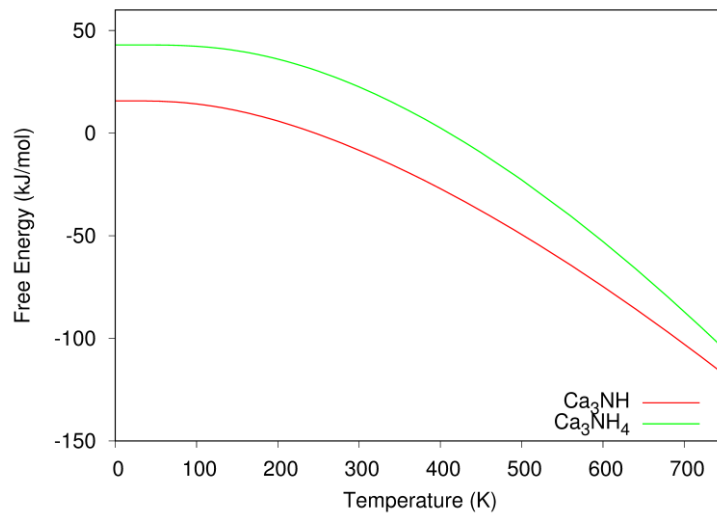
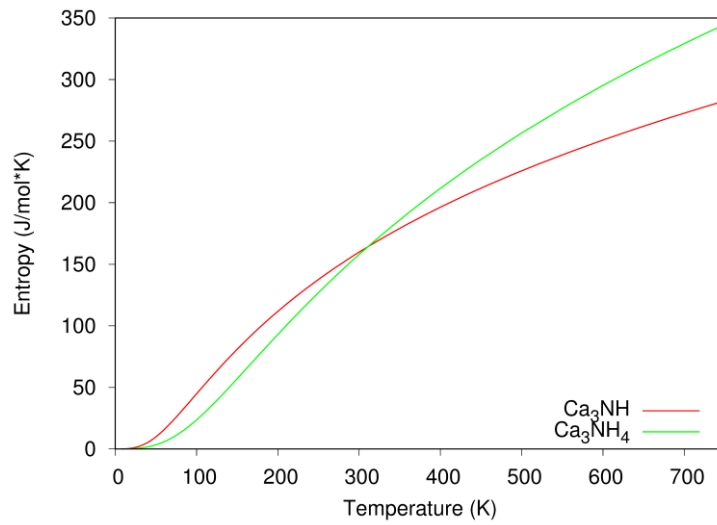


Figure 4.8 The thermal expansion, heat capacity at constant volume, entropy and free energy as a function of temperature at 0 GPa pressure for Ca_3NH_x

In addition to the temperature dependent thermal properties, the Debye temperature (Θ_D), the longitudinal wave velocity (V_l), the transverse wave velocity (V_t), the

average wave velocity (V_m), the Zener anisotropic factor (A), the anisotropic factor in shear (A_G) and compression (A_B) and the universal anisotropic factor (A^U) have been determined and listed in Table 4.7. Ca_3NH_4 has the highest Debye temperature among these compounds. It is found that, Ca_3NH_4 has the highest Debye temperature among these compounds. If A is one, this situation reveals the completely isotropy. On the other hand, the case in which A is different than one means completely anisotropy. Table 4.7 indicates that all studied compounds are elastically anisotropic. Furthermore, having zero value of A_G , A_B and A^U means elastic isotropy while the value having different than zero indicates elastic anisotropy. The A_G , A_B and A^U values indicates that these compounds are elastically isotropic in compression while they are anisotropic in shear and universal anisotropic index.

Table 4.7 The Debye temperature (Θ_D in K), the longitudinal wave velocity (V_l in m/s), the transverse wave velocity (V_t in m/s), the average wave velocity (V_m in m/s), the Zener anisotropic factor (A), the anisotropic factor in shear (A_G) and compression (A_B) and the universal anisotropic factor (A^U) for Ca_3XH , Ca_3XH_4 , and Ca_3XH_7

Compound	Θ_D	V_l	V_t	V_m	A	A_G	A_B	A^U
Ca_3CH	416.00	6272	3699	4099	0.44	7.92	0.00	0.85
Ca_3CH_4	387.70	6038	2849	3206	5.10	28.16	0.00	3.95
Ca_3CH_7	568.60	7002	3886	4328	0.80	0.66	0.00	0.06
Ca_3NH	347.00	5725	2948	3301	0.39	10.46	0.00	1.15
Ca_3NH_4	604.60	7360	4417	4886	0.85	0.37	0.00	0.03

The minimum thermal conductivities have been calculated using two models: Clarke model [72] and Cahill model [73]. Table 4.8 lists the obtained minimum thermal conductivities, average mass per atom and density of number of atoms per volume for Ca_3XH , Ca_3XH_4 , and Ca_3XH_7 compounds. As the number of H atoms increases in the compounds, the minimum thermal conductivities and the density of number of atoms per volume increase while the average mass per atom decreases as can be deduced from Table 4.8.

Table 4.8 The minimum thermal conductivities (λ_{min} in $Wm^{-1}K^{-1}$), the average mass per atom (M_a in 10^{-26} kg) for Clarke model and the density of number of atoms per volume (n in 10^{28} m^{-3}) for Cahill model for Ca_3XH , Ca_3XH_4 , and Ca_3XH_7

Compounds	Clarke Model		Cahill Model	
	M_a	λ_{min}	n	λ_{min}
Ca_3CH	4.43	0.81	3.90	0.88
Ca_3CH_4	2.83	0.93	6.70	1.08
Ca_3CH_7	2.10	1.33	8.50	1.46
Ca_3NH	4.49	0.72	4.40	0.81
Ca_3NH_4	2.87	1.43	7.10	1.56

4.2.4. Electronic Properties for Ca_3XH

The band structure and corresponding partial density of states (PDOS) were obtained and it has been found that all these structures have metallic character. Figure 4.9 shows the band structure for Ca_3CH_7 to show this character and the remaining band structures will not be presented here. The corresponding partial density of states also have been presented in Figure 4.9 and as can be seen from DOS plot, the most contribution to the DOS above the Fermi level comes from Ca atoms. In addition, the C atoms give more contribution to the DOS below Fermi level. Figure 4.10 and Figure 4.11 show the partial density of states for Ca_3CH_x and Ca_3NH_x compounds, respectively. As can be deduced from these figures, the contribution from Ca atoms to the PDOS is decreased while the contribution from H atoms is increased with the increasing number of H atoms in the structures. In addition, the number of electrons at the Fermi level has been obtained as 0.32, 1.30 and 0.13 for Ca_3CH , Ca_3CH_4 and Ca_3CH_7 , respectively. As the number of electrons at the Fermi level are compared, it has been found that Ca_3CH_4 has the highest number of electrons implying the electronic unstability of this compound.

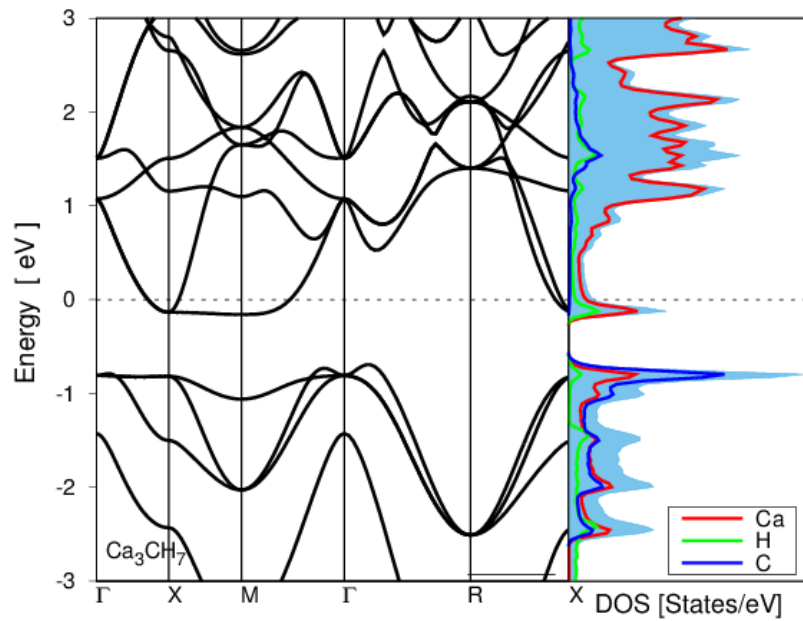


Figure 4.9 The band structure for Ca_3CH_7

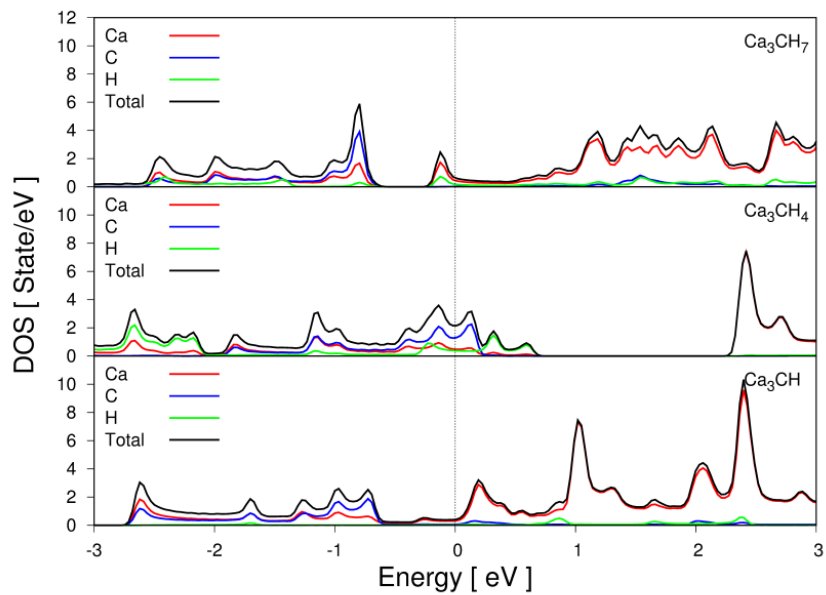


Figure 4.10 The partial density of states for Ca_3CH , Ca_3CH_4 and Ca_3CH_7

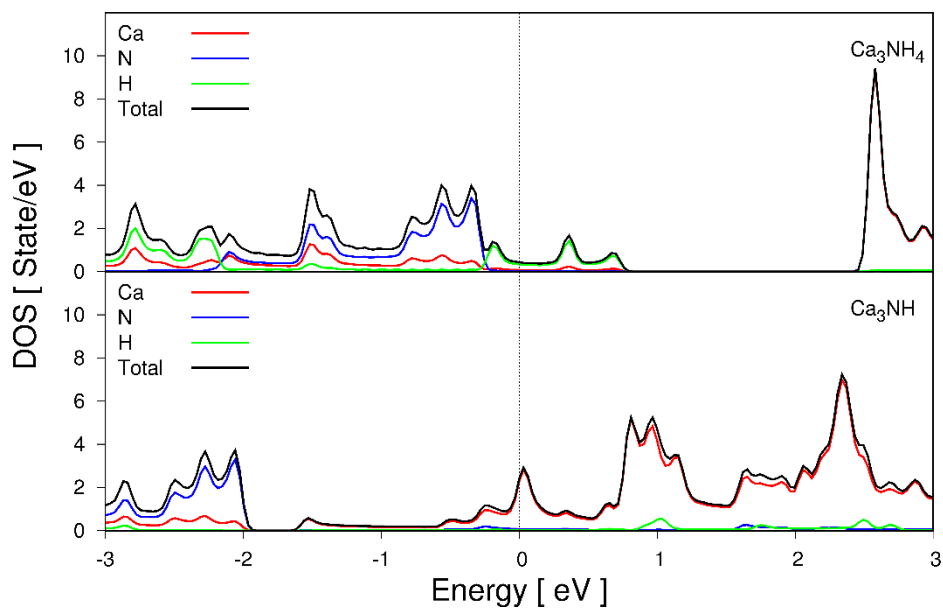


Figure 4.11 The partial density of states for Ca_3NH and Ca_3NH_4

Figure 4.12 shows the electron-density distribution for Ca_3CH , Ca_3CH_4 and Ca_3CH_7 compounds in (1 0 0) plane but Ca_3NH and Ca_3NH_4 are not presented here due having similar distributions. The contribution from H atoms to the charge density distribution increases with the increasing number of H atoms in the structure. In addition, the Bader net partial charges have been calculated and listed in Table 4.9. The charge is transferred away from Ca atom, while it is transferred to C/N and H atoms and the total Bader net charges are found to be zero for both compounds. Also, Ca and H atoms in Ca_3CH_4 have large Bader partial charges that results from the electronic instability of this compound.

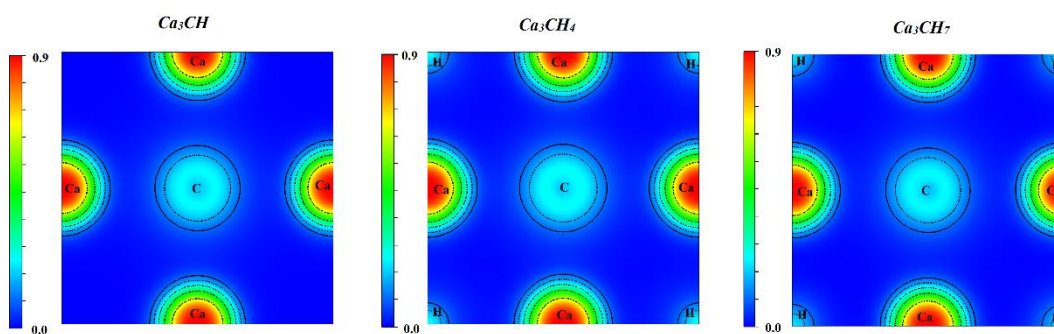


Figure 4.12 The electron-density distributions for Ca_3CH , Ca_3CH_4 and Ca_3CH_7

Table 4.9 The Bader net charges (in units of e per unit cell) for Ca_3CH , Ca_3CH_4 , Ca_3CH_7 , Ca_3NH , and Ca_3NH_4

Ion	Ca_3CH	Ca_3CH_4	Ca_3CH_7	Ca_3NH	Ca_3NH_4
Ca	3.45	15.73	3.83	2.99	4.16
C or N	-2.55	-2.80	-2.35	-2.04	-1.86
H	-0.90	-12.93	-1.48	-0.96	-2.30

Consequently, among the energetically and mechanically stable Ca_3XH compounds, Ca_3CH_7 has the highest gravimetric storage capacity as 5.08 wt.% with the hydrogen desorption temperature of 817.8 K.

CHAPTER 5

HYDROGEN STORAGE STUDIES FOR PEROVSKITE TYPE HYDRIDES

5.1. Introduction

In this chapter, structural, electronic, mechanic, vibrational and hydrogen storage properties of $XNiH_3$ (where X is Li, Na or K) perovskite type hydrides have been investigated. These studies have been in press in International Journal of Hydrogen Energy with the title of “Investigation of structural, electronic and lattice dynamical properties of $XNiH_3$ (X=Li, Na and K) Perovskite Type Hydrides and their Hydrogen Storage Applications” and it is under review.

5.2. Structural Optimization for $XNiH_3$

$XNiH_3$ where X is Li, Na or K belong to space group 221 (Pm-3m) as shown in Figure 5.1. In the literature, $LiNiH_3$ perovskite type hydride was synthesized and investigated using in situ synchrotron X-ray diffraction [100] and also studied with theoretical modeling [101]. The optimized lattice parameters, the calculated formation energies and the atomic positions have been listed in Table 5.1 with the available literature results for $LiNiH_3$. The lattice constant for $LiNiH_3$ is found to be consistent with the literature. In addition, the lattice constant increases from $LiNiH_3$ to $KNiH_3$. The calculated negative formation energies imply that these compounds are energetically stable and synthesizable. Furthermore, the order of the stability of these compounds are as follows: $LiNiH_3 > NaNiH_3 > KNiH_3$. Table 5.1 also lists the gravimetric hydrogen storage capacities and the hydrogen desorption temperatures for $XNiH_3$ compounds. $LiNiH_3$ has the highest hydrogen storage capacity while $KNiH_3$ has the highest hydrogen desorption temperature among the studied compounds.

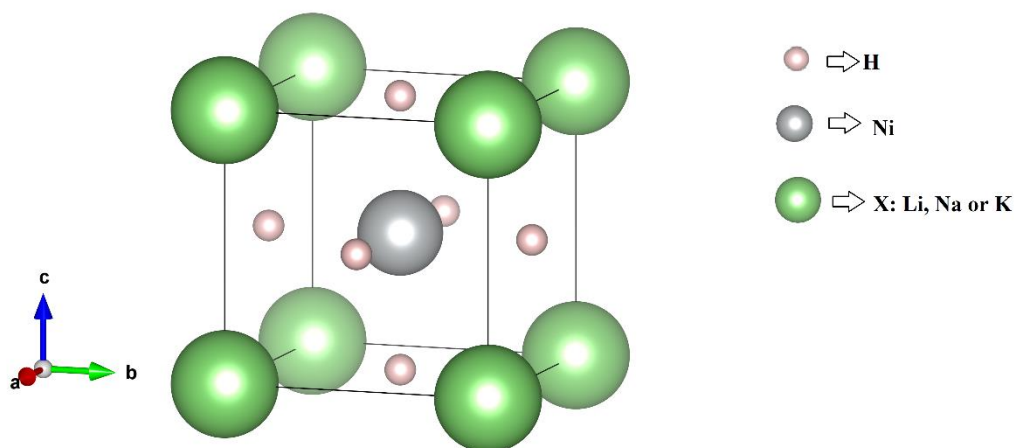


Figure 5.1 The crystal structure for $XNiH_3$

Table 5.1 The optimized lattice constants (a in \AA), the calculated formation energies (ΔE_{For} in eV/atom), the atomic positions, the gravimetric hydrogen storage capacities ($C_{wt\%}$) and the hydrogen desorption temperatures (T in K) for $XNiH_3$

Compound	a	ΔE_{For}	Atomic Positions	$C_{wt\%}$	T
LiNiH ₃	3.23	-0.73	Li: 1a (0.000, 0.000, 0.000)	4.40	537.9
	3.21 ^[100]		Ni: 1b (0.500, 0.500, 0.500)		
	3.25 ^[101]		H: 3c (0.000, 0.500, 0.500)		
NaNiH ₃	3.28	-0.69	Na: 1a (0.000, 0.000, 0.000) Ni: 1b (0.500, 0.500, 0.500) H: 3c (0.000, 0.500, 0.500)	3.57	511.9
KNiH ₃	3.62	-0.61	K: 1a (0.000, 0.000, 0.000) Ni: 1b (0.500, 0.500, 0.500) H: 3c (0.000, 0.500, 0.500)	3.30	447.1

The X-ray diffraction patterns for these hydrides have been shown in Figure 5.2. Both compounds show polycrystalline nature. Also, the 2θ values in (1 0 0) plane are found as 27.59° , 26.37° and 24.54° for LiNiH₃, NaNiH₃ and KNiH₃, respectively.

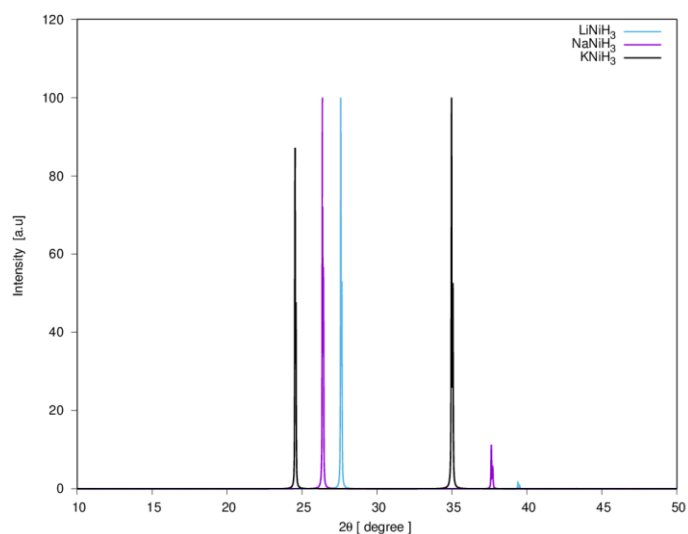
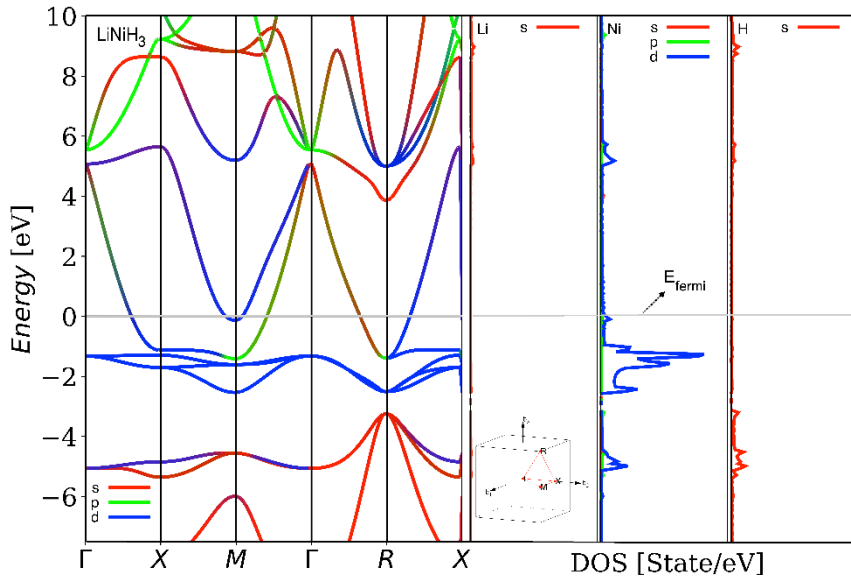


Figure 5.2 X-ray diffraction patterns for XNiH₃

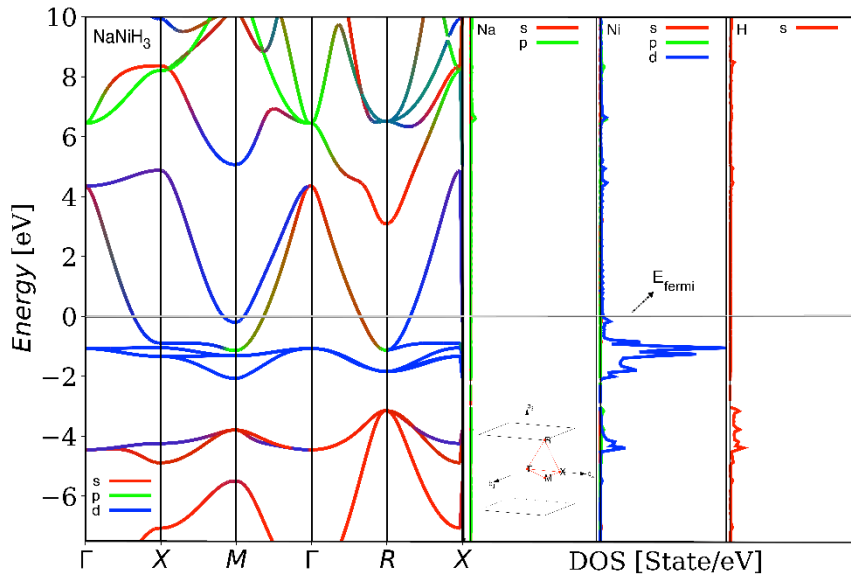
5.3. Electronic Properties for XNiH₃

The band structure and the corresponding density of states (PDOS) have been shown in Figure 5.3 for XNiH₃ compounds. The band branches have been shown with different colors to show the contributions from the s, p and d electrons to the band structure. All these compounds show metallic character as can be seen from Figure 5.3. Furthermore, the partial density of states have been shown in Figure 5.3 for each atom and the most contribution to the PDOS comes from the d states of Ni atoms as can be deduced from Figure 5.3.

(a)



(b)



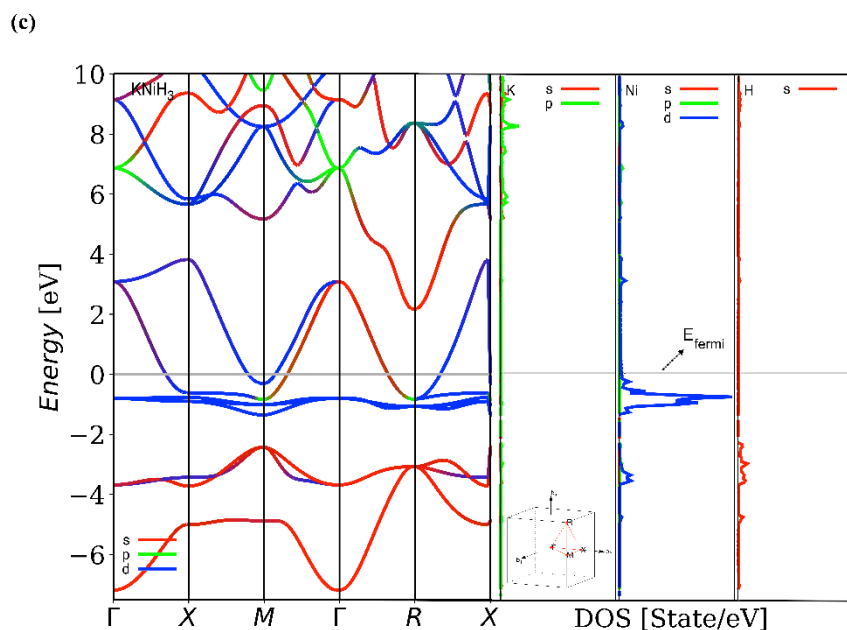


Figure 5.3 The band structures and corresponding partial density of states for (a) LiNiH_3 , (b) NaNiH_3 and (c) KNiH_3 .

The electron-density distribution for LiNiH_3 has been obtained and shown in Figure 5.4 that is generated for (1 0 0) direction for a $2 \times 2 \times 2$ supercell. As can be seen from the figure, LiNiH_3 has ionic bonding. Also, NaNiH_3 and KNiH_3 have similar electron-density distributions that are not given to save space in this chapter and they have ionic bonding. In addition, the Bader net partial charges for these compounds have been obtained and listed in Table 5.2. As can be deduced from the table, the charge is transferred away from X and Ni atoms, while it is transferred to H atoms. Also, the total Bader net charges are zero. Li, Na and K atoms have similar Bader net charges.

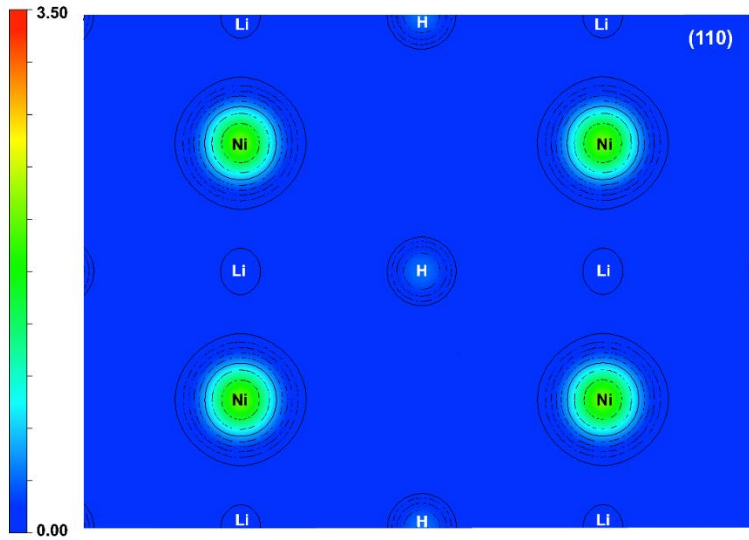


Figure 5.4 The electron-density distribution for LiNiH_3 along $(1\ 0\ 0)$ direction for a $2 \times 2 \times 2$ supercell

Table 5.2 The Bader net charges (in units of e per unit cell) for XNiH_3

Ion	LiNiH_3	NaNiH_3	KNiH_3
Li, Na or K	0.88	0.80	0.70
Ni	0.21	0.30	0.39
H	-1.09	-1.10	-1.09

5.4. Mechanical Properties for XNiH_3

The elastic constants (C_{ij}) for XNiH_3 compounds were calculated and listed in Table 5.3. All these compounds satisfy the Born stability criteria and as a result, they are mechanically stable compounds. Using these constants, the further mechanical properties could be obtained.

Table 5.3 The calculated elastic constants (C_{ij} in GPa) for XNiH_3

Compound	C_{11}	C_{12}	C_{44}
LiNiH_3	226.00	36.70	48.50
NaNiH_3	180.50	40.70	59.90
KNiH_3	113.20	46.90	59.40

The obtained mechanical properties such as bulk modulus, shear modulus, etc. have been listed in Table 5.4 for XNiH₃ compounds. LiNiH₃ has the highest bulk modulus and Young's modulus while NaNiH₃ has the highest shear modulus among these compounds. Also, these compounds have ionic bonding as concluded from Poisson's ratio and G/B ratio that is consistent with the electron-density distributions. Furthermore, these compounds have B/G ratios lower than 1.75 which indicates the brittleness of these compounds.

Table 5.4 Bulk modulus (B in GPa), shear modulus (G in GPa), Young's modulus (E in GPa), Poisson's ratio (ν), G/B ratio and B/G ratio for XNiH₃

Compound	B	G	E	ν	G/B	B/G
LiNiH ₃	99.80	63.50	157.10	0.24	0.64	1.57
NaNiH ₃	87.30	63.70	153.70	0.21	0.73	1.37
KNiH ₃	69.00	47.00	114.90	0.22	0.68	1.47

The anisotropic elastic properties of XNiH₃ compounds have been visualized in 3D as shown in Figure 5.5. Only the linear compressibility is found to be isotropic for all compounds and the remaining parameters are anisotropic. In addition, the minimum and maximum values for these parameters have been listed in Table 5.5.

Table 5.5 The minimum and maximum values of Young's modulus (E in GPa), linear compressibility (β), shear modulus (G in GPa), and Poisson's ratio(ν) for XNiH₃

Compound	E		β		G		ν	
	E_{min}	E_{max}	β_{min}	β_{max}	G_{min}	G_{max}	ν_{min}	ν_{max}
LiNiH ₃	125.22	215.75	3.34	3.34	48.50	94.65	0.09	0.44
NaNiH ₃	146.25	165.52	3.82	3.82	59.90	69.90	0.17	0.26
KNiH ₃	85.72	138.47	4.83	4.83	33.15	59.40	0.01	0.41

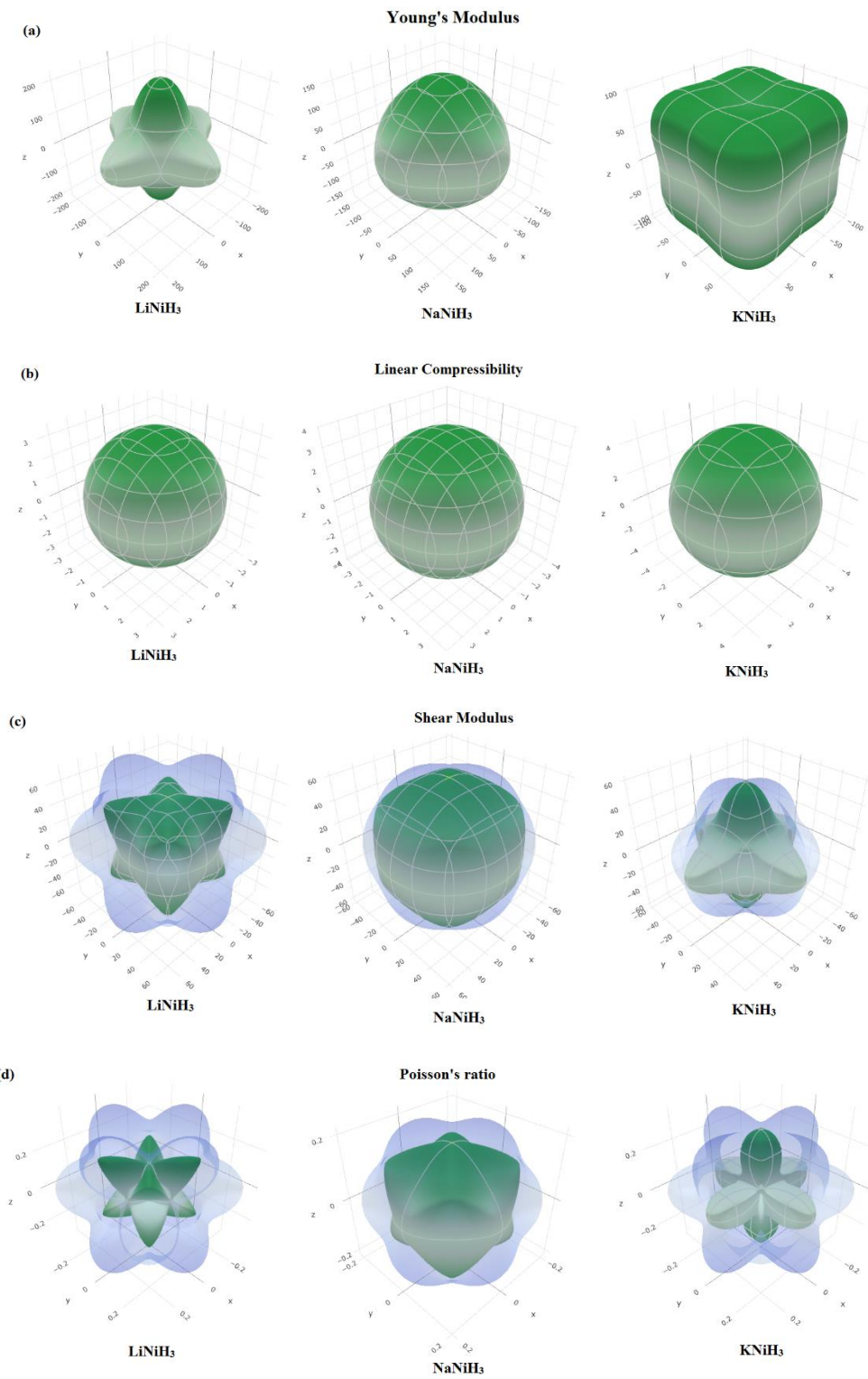


Figure 5.5 The direction dependent (a) Young's modulus, (b) linear compressibility (c) shear modulus and (d) Poisson's ratio in 3D for $XNiH_3$

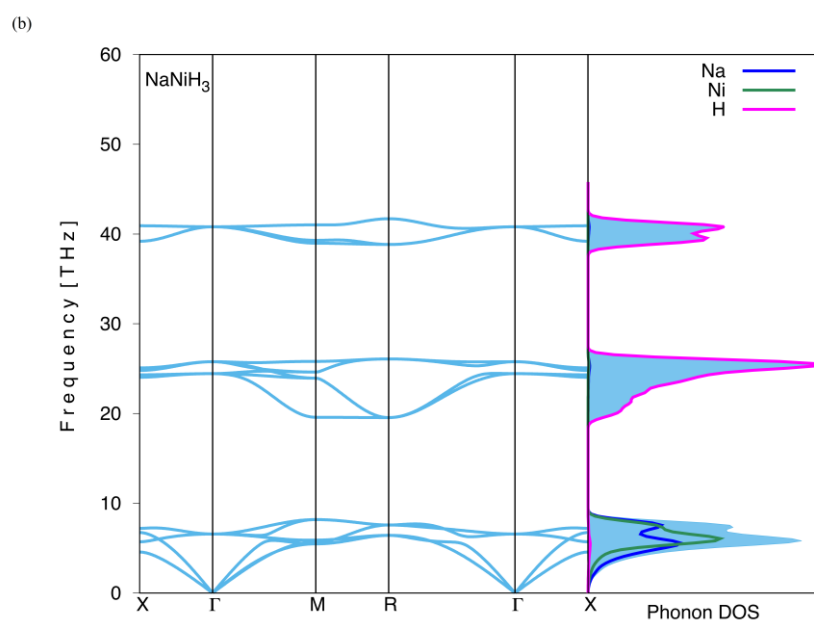
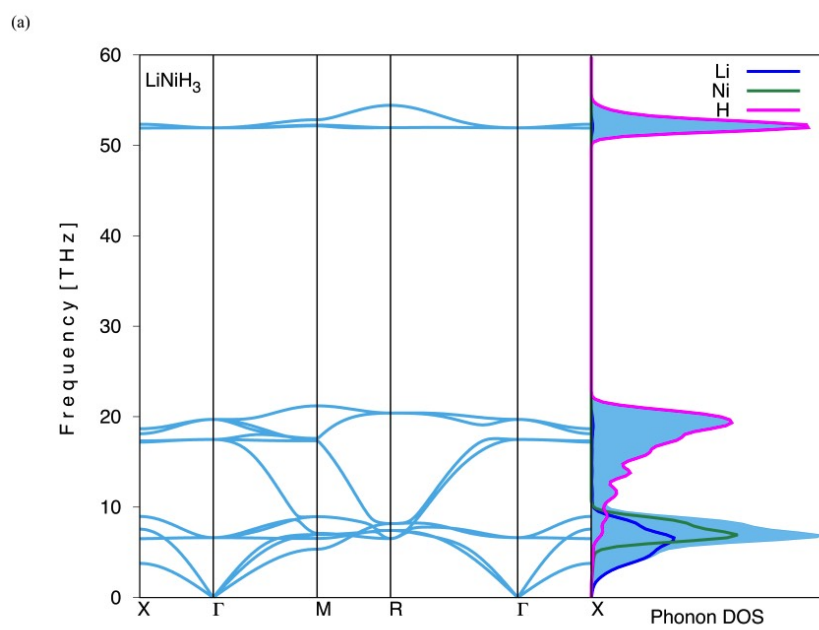
Moreover, the longitudinal wave velocity (V_l), the transverse wave velocity (V_t), the average wave velocity (V_m), the Debye temperature (Θ_D), the Zener anisotropic index (A), anisotropic index in shear (A_G) and compression (A_B) and the universal anisotropic index (A^U) have been determined and listed in Table 5.6. As can be deduced from Table 5.6, LiNiH₃ has the highest Debye temperature. Also, these compounds are mechanically anisotropic according to the anisotropic indexes except the anisotropic index in shear.

Table 5.6 The Debye temperature (Θ_D in K), longitudinal wave velocity (V_l in m/s), the transverse wave velocity (V_t in m/s), the average wave velocity (V_m in m/s), the Zener anisotropic factor A , the anisotropic factor in shear (A_G) and compression (A_B) and the universal anisotropic for (A^U) for XNiH₃

Compound	Θ_D	V_l	V_t	V_m	A	A_G	A_B	A^U
LiNiH ₃	756.50	7383	4331	4801	0.51	5.27	0.00	0.56
NaNiH ₃	695.60	6871	4178	4616	0.86	0.31	0.00	0.03
KNiH ₃	568.30	6122	3657	4047	1.79	4.04	0.00	0.42

5.5. Vibrational and Thermal Properties for XNiH₃

The vibrational properties of XNiH₃ compounds have been studied using a 2 x 2 x 2 supercell. Figure 5.6 shows the obtained phonon dispersion curves and corresponding phonon density of states (PDOS) for LiNiH₃, NaNiH₃ and KNiH₃, respectively. XNiH₃ compound has five atoms in its unit cell, so there are 15 phonon branches in the figures where three of them are acoustic branches and the remaining of them are optic branches. H is the lightest atom in the compounds, so it gives contributions to the higher frequencies as can be seen from the PDOS plots.



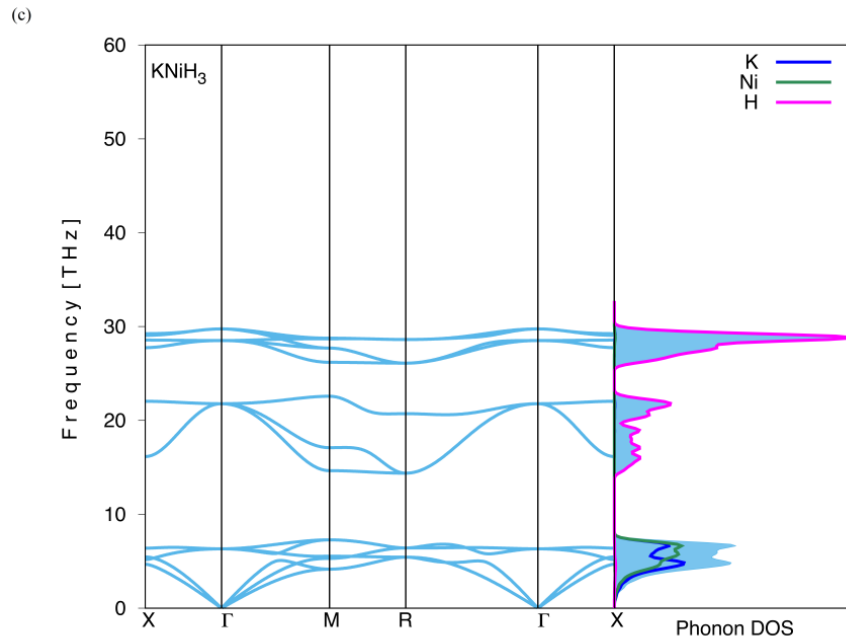


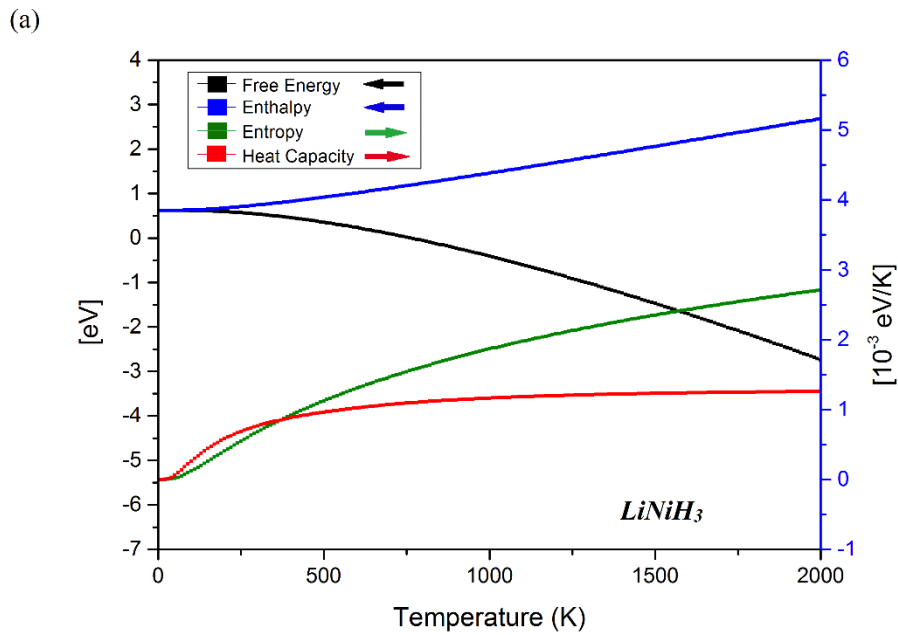
Figure 5.6 The phonon dispersion curves and corresponding phonon density of states for (a) LiNiH₃, (b) NaNiH₃ and (c) KNiH₃

According to the phonon dispersion curves, the acoustic and optic branches are more close to each other when the compound changes from LiNiH₃ to KNiH₃ that is related to the lower thermal conductivities. Table 5.7 lists the calculated minimum thermal conductivities obtained using the calculated elastic constants for two models that shows the consistency with the phonon dispersion curves. M_a is the average mass per atom and n is the density of number of atoms per volume. LiNiH₃ has the highest minimum thermal conductivities and KNiH₃ has the lowest thermal conductivities among these compounds. Also, n decreases while M_a increases from LiNiH₃ to KNiH₃.

Table 5.7 The minimum thermal conductivities (λ_{min} in $Wm^{-1}K^{-1}$), the average mass per atom (M_a in 10^{-26} kg) for Clarke model and the density of number of atoms per volume (n in $10^{28} m^{-3}$) for Cahill model for $XNiH_3$

Compound	Clarke's Model		Cahill's Model	
	M_a	λ_{min}	n	λ_{min}
LiNiH ₃	2.28	2.29	14.80	2.50
NaNiH ₃	2.81	2.00	12.90	2.17
KNiH ₃	3.35	1.53	10.40	1.67

The obtained phonon frequencies were employed to obtain thermal properties for $XNiH_3$. Figure 5.7 shows the free energy, enthalpy, entropy and heat capacity as a function of temperature for LiNiH₃, NaNiH₃ and KNiH₃. As the temperature increases, enthalpy, entropy and heat capacity increase while free energy decreases. In addition, the heat capacity reaches a constant called Dulong-Petit limit at high temperatures.



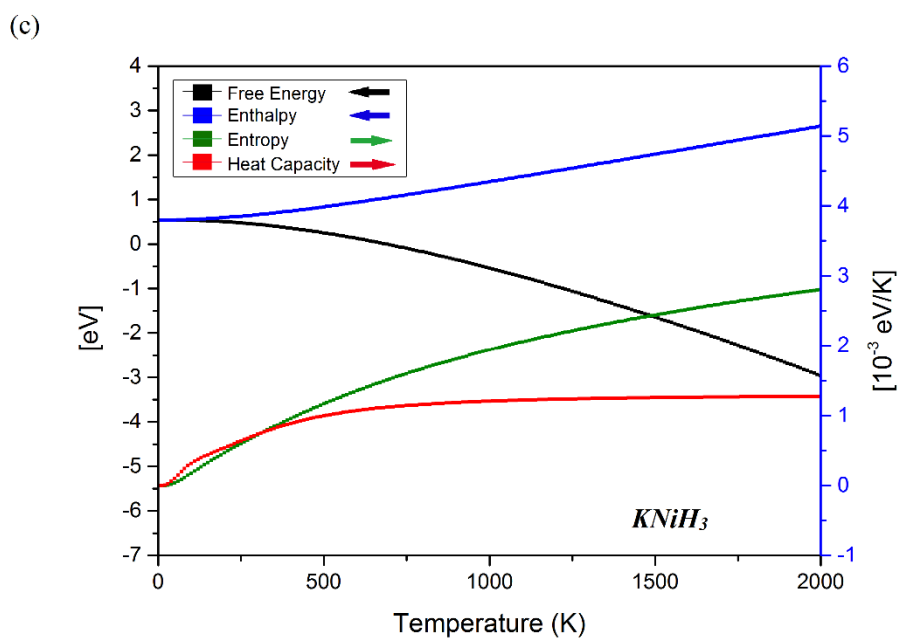
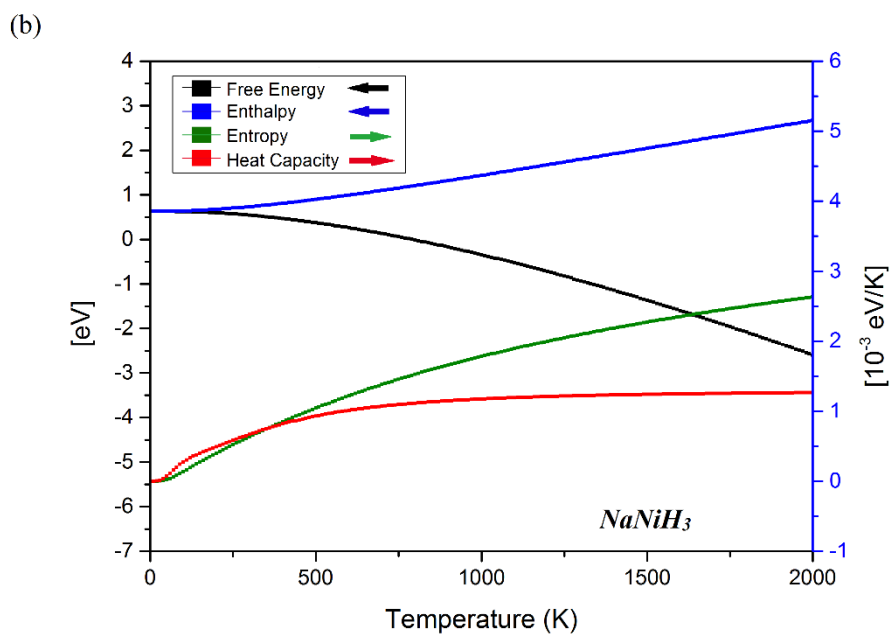


Figure 5.7 The free energy, enthalpy, entropy and heat capacity as a function of temperature for (a) LiNiH_3 , (b) NaNiH_3 and (c) KNiH_3

The studies for XNiH_3 reveals that these compounds are energetically, mechanically and dynamically stable. In addition, LiNiH_3 has the highest gravimetric storage capacity as 4.40 wt.% and KNiH_3 has the lowest desorption temperature as 447.1 K.

CHAPTER 6

CONCLUSION

The perovskite materials have been investigated for their hydrogen storage properties in this thesis that could be a potential candidate for solid state hydrogen storage method. The perovskite materials have been grouped into three as perovskite materials, anti-perovskite materials and perovskite type hydrides and their structural, mechanic, electronic and vibrational properties have been studied. The hydrogen doping studies have been performed and the gravimetric hydrogen storage capacities and the hydrogen desorption temperatures have been obtained for these materials.

The perovskite materials including $BaXO_3$ ($X=Sc$ or Y) and $XTiO_3$ ($X=Mg$ or Ca) compounds have been studied. $BaXO_3$ compounds have been investigated for the five possible crystal structures and it has been found that the most stable phases are orthorhombic and cubic phases for $BaScO_3$ and $BaYO_3$, respectively. The hydrogen doping studies have been performed to the most stable phases of these compounds and 0.22wt% and 1.09 wt. % gravimetric hydrogen storage capacities and 1769.7 K and 599.2 K hydrogen desorption temperatures have been obtained for $BaScO_3H_{0.5}$ and $BaYO_3H_3$, respectively. The hydrogen doping studies for $BaXO_3$ compounds reveal that the number of doped hydrogen atoms are related with the crystal structure where the cubic crystal structure provides to store more hydrogen atoms. Therefore, $XTiO_3$ compounds have been studied in the cubic crystal structure and it has been found that $XTiO_3$ compounds are energetically and mechanically stable. Several hydrogen doping studies to $XTiO_3$ compounds have been performed but both energetically and mechanically stable compound is only $CaTiO_3H_6$ compound with 4.27 wt. % gravimetric hydrogen storage capacity and 827.1 K hydrogen desorption temperature.

As a result of these studies, the cubic crystal structure provide to store more hydrogen atoms and the gravimetric hydrogen storage capacity increases with the light weight atoms in the structure.

The anti-perovskite materials with Ca_3XH ($\text{X}=\text{C}$ or N) compounds have been investigated. Ca_3XH compounds are energetically and mechanically stable and several hydrogen doping studies have been performed and the energetic and mechanic stability conditions eliminate some of them but there are still five compounds (Ca_3CH , Ca_3CH_4 , Ca_3CH_7 , Ca_3NH , and Ca_3NH_4) that satisfy these stability conditions. The thermo-elastic properties for these compounds have been obtained. In addition, their electronic properties have been studied and it has been found that they are metallic compounds. Among these stable compounds, Ca_3CH_7 has the highest gravimetric storage capacity as 5.08 wt.% with the hydrogen desorption temperature of 817.8 K.

Furthermore, the perovskite type hydrides with XNiH_3 ($\text{X}=\text{Li}$, Na or K) have been investigated. LiNiH_3 compound have been studied both experimentally and theoretically and the obtained lattice constant is consistent with these results. In addition, XNiH_3 compounds are found to be mechanically and dynamically stable compounds. The electronic properties of these compounds have showed that they are metallic compounds. In addition, the hydrogen storage properties have been studied and it has been found that LiNiH_3 has the highest gravimetric storage capacity as 4.40 wt.% and KNiH_3 has the lowest desorption temperature as 447.1 K.

REFERENCES

- [1] T. Wilberforce, A. Alaswad, A. Palumbo, and M. Dassisti, “Advances in stationary and portable fuel cell applications,” *Int. J. Hydrogen Energy*, vol. 41, no. 37, pp. 16509–16522, Oct. 2016.
- [2] P. Ferreira-Aparicio and A. M. Chaparro, *Portable hydrogen energy systems : fuel cells and storage fundamentals and applications*, 1st editio. Academic Press.
- [3] A. Züttel, “Hydrogen storage methods,” *Naturwissenschaften*, vol. 91, no. 4, pp. 157–172, Apr. 2004.
- [4] K. Mazloomi and C. Gomes, “Hydrogen as an energy carrier: Prospects and challenges,” *Renew. Sustain. Energy Rev.*, vol. 16, no. 5, pp. 3024–3033, Jun. 2012.
- [5] P. Nikolaidis and A. Poullikkas, “A comparative overview of hydrogen production processes,” *Renew. Sustain. Energy Rev.*, vol. 67, pp. 597–611, Jan. 2017.
- [6] U. Eberle, M. Felderhoff, and F. Schüth, “Chemical and Physical Solutions for Hydrogen Storage,” *Angew. Chemie Int. Ed.*, vol. 48, no. 36, pp. 6608–6630, Aug. 2009.
- [7] S. Niaz, T. Manzoor, and A. H. Pandith, “Hydrogen storage: Materials, methods and perspectives,” *Renew. Sustain. Energy Rev.*, vol. 50, pp. 457–469, Oct. 2015.
- [8] L. Schlapbach and A. Züttel, “Hydrogen-storage materials for mobile applications,” in *Materials for Sustainable Energy*, Co-Published with Macmillan Publishers Ltd, UK, 2010, pp. 265–270.
- [9] D. J. Durbin and C. Malardier-Jugroot, “Review of hydrogen storage techniques for on board vehicle applications,” *Int. J. Hydrogen Energy*, vol. 38, no. 34, pp. 14595–14617, Nov. 2013.
- [10] G. (Gavin) Walker, *Solid state hydrogen storage : materials and chemistry*. Woodhead Pub., 2008.
- [11] A. W. C. van den Berg and C. O. Areán, “Materials for hydrogenstorage: current research trends and perspectives,” *Chem. Commun.*, vol. 0, no. 6, pp. 668–681, Jan. 2008.
- [12] I. P. Jain, P. Jain, and A. Jain, “Novel hydrogen storage materials: A review of lightweight complex hydrides,” *J. Alloys Compd.*, vol. 503, no. 2, pp. 303–339, Aug. 2010.

- [13] D. P. Broom, *Hydrogen storage materials: the characterisation of their storage properties*. Springer, 2011.
- [14] US Department of Energy, “DOE Technical Targets for Hydrogen Storage Systems for Portable Power Equipment | Department of Energy.” [Online]. Available: <https://www.energy.gov/eere/fuelcells/doe-technical-targets-hydrogen-storage-systems-portable-power-equipment>. [Accessed: 25-Feb-2019].
- [15] A. C. Dillon, K. M. Jones, T. A. Bekkedahl, C. H. Kiang, D. S. Bethune, and M. J. Heben, “Storage of hydrogen in single-walled carbon nanotubes,” *Nature*, vol. 386, no. 6623, pp. 377–379, Mar. 1997.
- [16] N. L. Rosi *et al.*, “Hydrogen storage in microporous metal-organic frameworks,” *Science*, vol. 300, no. 5622, pp. 1127–9, May 2003.
- [17] I. P. Jain, P. Jain, and A. Jain, “Novel hydrogen storage materials: A review of lightweight complex hydrides,” *J. Alloys Compd.*, vol. 503, no. 2, pp. 303–339, Aug. 2010.
- [18] B. Sakintuna, F. Lamari-Darkrim, and M. Hirscher, “Metal hydride materials for solid hydrogen storage: A review,” *Int. J. Hydrogen Energy*, vol. 32, no. 9, pp. 1121–1140, Jun. 2007.
- [19] K. Ikeda, Y. Kogure, Y. Nakamori, and S. Orimo, “Formation region and hydrogen storage abilities of perovskite-type hydrides,” *Prog. Solid State Chem.*, vol. 35, no. 2–4, pp. 329–337, Jan. 2007.
- [20] T. Sato, D. Noréus, H. Takeshita, and U. Häussermann, “Hydrides with the perovskite structure: General bonding and stability considerations and the new representative CaNiH₃,” *J. Solid State Chem.*, vol. 178, no. 11, pp. 3381–3388, Nov. 2005.
- [21] A. H. Reshak, “NaMgH₃ a perovskite-type hydride as advanced hydrogen storage systems: Electronic structure features,” *Int. J. Hydrogen Energy*, vol. 40, no. 46, pp. 16383–16390, Dec. 2015.
- [22] D. Pottmaier *et al.*, “Structure and Thermodynamic Properties of the NaMgH₃ Perovskite: A Comprehensive Study,” *Chem. Mater.*, vol. 23, no. 9, pp. 2317–2326, May 2011.
- [23] Z. Wang, S. Tao, J. Deng, H. Zhou, and Q. Yao, “Significant improvement in the dehydriding properties of perovskite hydrides, NaMgH₃, by doping with K₂TiF₆,” *Int. J. Hydrogen Energy*, vol. 42, no. 12, pp. 8554–8559, Mar. 2017.
- [24] Y. Li, Y. Mi, J. S. Chung, and S. G. Kang, “First-principles studies of K_{1-x}M_xMgH₃ (M = Li, Na, Rb, or Cs) perovskite hydrides for hydrogen storage,” *Int. J. Hydrogen Energy*, vol. 43, no. 4, pp. 2232–2236, Jan. 2018.

- [25] K. Ikeda, Y. Kogure, Y. Nakamori, and S. Orimo, “Reversible hydriding and dehydriding reactions of perovskite-type hydride NaMgH_3 ,” *Scr. Mater.*, vol. 53, no. 3, pp. 319–322, Aug. 2005.
- [26] B. Rehmat, M. A. Rafiq, Y. Javed, Z. Irshad, N. Ahmed, and S. M. Mirza, “Elastic properties of perovskite-type hydrides LiBeH_3 and NaBeH_3 for hydrogen storage,” *Int. J. Hydrogen Energy*, vol. 42, no. 15, pp. 10038–10046, Apr. 2017.
- [27] Y. Bouhadda, N. Fenineche, and Y. Boudouma, “Hydrogen storage: Lattice dynamics of orthorhombic NaMgH_3 ,” *Phys. B Condens. Matter*, vol. 406, no. 4, pp. 1000–1003, Feb. 2011.
- [28] R. Martínez-Coronado, J. Sánchez-Benítez, M. Retuerto, M. T. Fernández-Díaz, and J. A. Alonso, “High-pressure synthesis of $\text{Na}_{1-x}\text{Li}_x\text{MgH}_3$ perovskite hydrides,” *J. Alloys Compd.*, vol. 522, pp. 101–105, May 2012.
- [29] G. Kresse and J. Furthmüller, “Efficient iterative schemes for *ab initio* total-energy calculations using a plane-wave basis set,” *Phys. Rev. B*, vol. 54, no. 16, pp. 11169–11186, Oct. 1996.
- [30] G. Kresse and J. Furthmüller, “Efficiency of *ab-initio* total energy calculations for metals and semiconductors using a plane-wave basis set,” *Comput. Mater. Sci.*, vol. 6, no. 1, pp. 15–50, Jul. 1996.
- [31] K. Capelle, “A bird’s-eye view of density-functional theory,” *Brazilian J. Phys.*, vol. 36, no. 4a, pp. 1318–1343, Dec. 2006.
- [32] M. J. Gillan, D. Alfè, J. Brodholt, L. Vočadlo, and G. D. Price, “First-principles modelling of Earth and planetary materials at high pressures and temperatures,” *Reports Prog. Phys.*, vol. 69, no. 8, pp. 2365–2441, Aug. 2006.
- [33] A. Zangwill, “A half century of density functional theory,” *Phys. Today*, vol. 68, no. 7, pp. 34–39, Jul. 2015.
- [34] R. O. Jones, “Density functional theory: Its origins, rise to prominence, and future,” *Rev. Mod. Phys.*, vol. 87, no. 3, pp. 897–923, Aug. 2015.
- [35] W. D. Callister and D. G. Rethwisch, *Materials science and engineering*. John Wiley High Education.
- [36] R. M. Martin, *Electronic structure: basic theory and practical methods*. Cambridge University Press, 2004.
- [37] E. Kaxiras, *Atomic and electronic structure of solids*, 1st edition. Cambridge University Press, 2007.
- [38] D. S. Sholl and J. A. Steckel, *Density functional theory: a practical introduction*. Wiley, 2009.

- [39] H. Toffoli, “Computational Materials Science 1 Physics 741 Lecture Notes.”
- [40] M. Born and R. Oppenheimer, “Zur Quantentheorie der Molekeln,” *Ann. Phys.*, vol. 389, no. 20, pp. 457–484, Jan. 1927.
- [41] P. Hohenberg and W. Kohn, “Inhomogeneous Electron Gas,” *Phys. Rev.*, vol. 136, no. 3B, pp. B864–B871, Nov. 1964.
- [42] W. Kohn and L. J. Sham, “Self-Consistent Equations Including Exchange and Correlation Effects,” *Phys. Rev.*, vol. 140, no. 4A, pp. A1133–A1138, Nov. 1965.
- [43] J. P. Perdew and Y. Wang, “Accurate and simple analytic representation of the electron-gas correlation energy,” *Phys. Rev. B*, vol. 45, no. 23, pp. 13244–13249, Jun. 1992.
- [44] J. P. Perdew, K. Burke, and M. Ernzerhof, “Generalized Gradient Approximation Made Simple,” *Phys. Rev. Lett.*, vol. 77, no. 18, pp. 3865–3868, Oct. 1996.
- [45] A. D. Becke, “Density-functional thermochemistry. III. The role of exact exchange,” *J. Chem. Phys.*, vol. 98, no. 7, pp. 5648–5652, Apr. 1993.
- [46] D. R. Hamann, M. Schlüter, and C. Chiang, “Norm-Conserving Pseudopotentials,” *Phys. Rev. Lett.*, vol. 43, no. 20, pp. 1494–1497, Nov. 1979.
- [47] D. Vanderbilt, “Soft self-consistent pseudopotentials in a generalized eigenvalue formalism,” *Phys. Rev. B*, vol. 41, no. 11, pp. 7892–7895, Apr. 1990.
- [48] P. E. Blöchl, “Projector augmented-wave method,” *Phys. Rev. B*, vol. 50, no. 24, pp. 17953–17979, Dec. 1994.
- [49] N. W. Ashcroft and N. D. Mermin, *Solid state physics*. Holt, Rinehart and Winston, 1976.
- [50] “Bilbao Crystallographic Server.” [Online]. Available: <http://www.cryst.ehu.es/>. [Accessed: 04-Mar-2019].
- [51] A. Jain *et al.*, “The Materials Project: Accelerating Materials Design Through Theory-Driven Data and Tools,” in *Handbook of Materials Modeling*, Cham: Springer International Publishing, 2018, pp. 1–34.
- [52] A. Erkişi, G. Gökoğlu, G. Sürücü, R. Ellialtıoğlu, and E. K. Yıldırım, “First-principles investigation of LaGaO₃ and LaInO₃ lanthanum perovskite oxides,” *Philos. Mag.*, vol. 96, no. 19, pp. 2040–2058, Jul. 2016.
- [53] K. Momma, F. Izumi, and IUCr, “VESTA 3 for three-dimensional visualization of crystal, volumetric and morphology data,” *J. Appl. Crystallogr.*, vol. 44, no. 6, pp. 1272–1276, Dec. 2011.

- [54] H. Ibach and H. (Hans) Lüth, *Solid-state physics : an introduction to principles of materials science*. Springer, 2009.
- [55] R. F. W. Bader, *Atoms in molecules : a quantum theory*. Clarendon Press, 1990.
- [56] W. Tang, E. Sanville, and G. Henkelman, “A grid-based Bader analysis algorithm without lattice bias,” *J. Phys. Condens. Matter*, vol. 21, no. 8, p. 084204, Feb. 2009.
- [57] R. S. Mulliken, “Electronic Population Analysis on LCAO–MO Molecular Wave Functions. I,” *J. Chem. Phys.*, vol. 23, no. 10, pp. 1833–1840, Oct. 1955.
- [58] F. L. Hirshfeld, “Bonded-atom fragments for describing molecular charge densities,” *Theor. Chim. Acta*, vol. 44, no. 2, pp. 129–138, 1977.
- [59] M. A. Caro, S. Schulz, and E. P. O’Reilly, “Comparison of stress and total energy methods for calculation of elastic properties of semiconductors,” *J. Phys. Condens. Matter*, vol. 25, no. 2, p. 025803, Jan. 2013.
- [60] Y. Le Page and P. Saxe, “Symmetry-general least-squares extraction of elastic coefficients from *ab initio* total energy calculations,” *Phys. Rev. B*, vol. 63, no. 17, p. 174103, Mar. 2001.
- [61] F. Mouhat and F.-X. Coudert, “Necessary and sufficient elastic stability conditions in various crystal systems,” *Phys. Rev. B*, vol. 90, no. 22, p. 224104, Dec. 2014.
- [62] M. Born, “On the stability of crystal lattices. I,” *Math. Proc. Cambridge Philos. Soc.*, vol. 36, no. 02, p. 160, Apr. 1940.
- [63] Z. Wu, E. Zhao, H. Xiang, X. Hao, X. Liu, and J. Meng, “Crystal structures and elastic properties of superhard IrN₂ and IrN₃ from first principles,” *Phys. Rev. B*, vol. 76, no. 5, p. 054115, Aug. 2007.
- [64] W. Voigt, *Lehrbuch der Kristallphysik*. Wiesbaden: Vieweg+Teubner Verlag, 1966.
- [65] A. Reuss, “Berechnung der Fließgrenze von Mischkristallen auf Grund der Plastizitätsbedingung für Einkristalle .,” *ZAMM - Zeitschrift für Angew. Math. und Mech.*, vol. 9, no. 1, pp. 49–58, Jan. 1929.
- [66] R. Hill, “The Elastic Behaviour of a Crystalline Aggregate,” *Proc. Phys. Soc. Sect. A*, vol. 65, no. 5, pp. 349–354, May 1952.
- [67] G. Surucu, “Investigation of structural, electronic, anisotropic elastic, and lattice dynamical properties of MAX phases borides: An Ab-initio study on hypothetical M₂AB (M = Ti, Zr, Hf; A = Al, Ga, In) compounds,” *Mater. Chem. Phys.*, vol. 203, pp. 106–117, Jan. 2018.
- [68] N. Miao, B. Sa, J. Zhou, and Z. Sun, “Theoretical investigation on the

- transition-metal borides with Ta₃B₄-type structure: A class of hard and refractory materials,” *Comput. Mater. Sci.*, vol. 50, no. 4, pp. 1559–1566, Feb. 2011.
- [69] S. I. Ranganathan and M. Ostoja-Starzewski, “Universal Elastic Anisotropy Index,” *Phys. Rev. Lett.*, vol. 101, no. 5, p. 055504, Aug. 2008.
- [70] R. Gaillac, P. Pullumbi, and F.-X. Coudert, “ELATE: an open-source online application for analysis and visualization of elastic tensors,” *J. Phys. Condens. Matter*, vol. 28, no. 27, p. 275201, Jul. 2016.
- [71] A. Erkisi, G. Surucu, and R. Ellialtioglu, “The investigation of electronic, mechanical and lattice dynamical properties of PdCoX (X = Si and Ge) half-Heusler metallics in α , β and γ structural phases: an *ab initio* study,” *Philos. Mag.*, vol. 97, no. 26, pp. 2237–2254, Sep. 2017.
- [72] D. R. Clarke, “Materials selection guidelines for low thermal conductivity thermal barrier coatings,” *Surf. Coatings Technol.*, vol. 163–164, pp. 67–74, Jan. 2003.
- [73] D. G. Cahill, S. K. Watson, and R. O. Pohl, “Lower limit to the thermal conductivity of disordered crystals,” *Phys. Rev. B*, vol. 46, no. 10, pp. 6131–6140, Sep. 1992.
- [74] E. Deligoz and H. Ozisik, “Mechanical and dynamical stability of TiAsTe compound from *ab initio* calculations,” *Philos. Mag.*, vol. 95, no. 21, pp. 2294–2305, Jul. 2015.
- [75] C. Kittel, *Introduction to solid state physics*. Wiley, 2005.
- [76] S. Baroni, S. de Gironcoli, A. Dal Corso, and P. Giannozzi, “Phonons and related crystal properties from density-functional perturbation theory,” *Rev. Mod. Phys.*, vol. 73, no. 2, pp. 515–562, Jul. 2001.
- [77] A. Togo, F. Oba, and I. Tanaka, “First-principles calculations of the ferroelastic transition between rutile-type and CaCl₂-type SiO₂ at high pressures,” *Phys. Rev. B*, vol. 78, no. 13, p. 134106, Oct. 2008.
- [78] A. Andreasen, “Predicting formation enthalpies of metal hydrides,” 2004.
- [79] Q. Zeng, K. Su, L. Zhang, Y. Xu, L. Cheng, and X. Yan, “Evaluation of the Thermodynamic Data of CH₃SiCl₃ Based on Quantum Chemistry Calculations,” *J. Phys. Chem. Ref. Data*, vol. 35, no. 3, pp. 1385–1390, Sep. 2006.
- [80] Z. Shi and A. H. Jayatissa, “Perovskites-Based Solar Cells: A Review of Recent Progress, Materials and Processing Methods,” *Mater. (Basel, Switzerland)*, vol. 11, no. 5, May 2018.
- [81] A. S. Bhalla, R. Guo, and R. Roy, “The perovskite structure—a review of its

- role in ceramic science and technology,” *Mater. Res. Innov.*, vol. 4, no. 1, pp. 3–26, Nov. 2000.
- [82] T. Wolfram and S. Ellialtıođlu, *Electronic and optical properties of D-band perovskites*. Cambridge University Press, 2006.
- [83] C. Kaderoglu, G. Surucu, and A. Erkisi, “The Investigation of Electronic, Elastic and Vibrational Properties of an Interlanthanide Perovskite: PrYbO₃,” *J. Electron. Mater.*, vol. 46, no. 10, pp. 5827–5836, Oct. 2017.
- [84] Z. Yi, N. H. Ladi, X. Shai, H. Li, Y. Shen, and M. Wang, “Will organic–inorganic hybrid halide lead perovskites be eliminated from optoelectronic applications?,” *Nanoscale Adv.*, 2019.
- [85] L. Pan and G. Zhu, *Perovskite Materials - Synthesis, Characterisation, Properties, and Applications*. InTech, 2016.
- [86] C. Moure and O. Peña, “Recent advances in perovskites: Processing and properties,” *Prog. Solid State Chem.*, vol. 43, no. 4, pp. 123–148, Dec. 2015.
- [87] M. A. Green, A. Ho-Baillie, and H. J. Snaith, “The emergence of perovskite solar cells,” *Nat. Photonics*, vol. 8, no. 7, pp. 506–514, Jul. 2014.
- [88] M. V Kovalenko, L. Protesescu, and M. I. Bodnarchuk, “Properties and potential optoelectronic applications of lead halide perovskite nanocrystals,” *Science*, vol. 358, no. 6364, pp. 745–750, Nov. 2017.
- [89] E. C. C. de Souza and R. Muccillo, “Properties and applications of perovskite proton conductors,” *Mater. Res.*, vol. 13, no. 3, pp. 385–394, Sep. 2010.
- [90] N. F. Atta, A. Galal, and E. H. El-Ads, “Perovskite Nanomaterials – Synthesis, Characterization, and Applications,” in *Perovskite Materials - Synthesis, Characterisation, Properties, and Applications*, InTech, 2016.
- [91] J. D. Pack and H. J. Monkhurst, “Special points for Brillouin-zone integrations—a reply,” *Phys. Rev. B*, vol. 16, no. 4, pp. 1748–1749, Aug. 1977.
- [92] H. J. Monkhurst and J. D. Pack, “Special points for Brillouin-zone integrations,” *Phys. Rev. B*, vol. 13, no. 12, pp. 5188–5192, Jun. 1976.
- [93] G. Narejo and W. F. Perger, “A Novel Coupling between the Electron Structure and Properties of Perovskite Transition Metal Oxides,” *Appl. Math.*, vol. 04, no. 09, pp. 1320–1325, Aug. 2013.
- [94] A. Togo and I. Tanaka, “First principles phonon calculations in materials science,” *Scr. Mater.*, vol. 108, pp. 1–5, Nov. 2015.
- [95] N. Pandech, “First-Principles Study of Pressure Dependent Elastic Properties in Selected Perovskite Materials,” Suranaree University of Technology, 2013.

- [96] S. Tariq, A. Ahmed, S. Saad, and S. Tariq, "Structural, electronic and elastic properties of the cubic CaTiO_3 under pressure: A DFT study," *AIP Adv.*, vol. 5, no. 7, p. 077111, Jul. 2015.
- [97] H. Moriwake, A. Kuwabara, C. A. J. Fisher, H. Taniguchi, M. Itoh, and I. Tanaka, "First-principles calculations of lattice dynamics in CdTiO_3 and CaTiO_3 : Phase stability and ferroelectricity," *Phys. Rev. B*, vol. 84, no. 10, p. 104114, Sep. 2011.
- [98] N. Pandech, K. Sarasamak, and S. Limpijumnong, "Elastic properties of perovskite ATiO_3 ($A = \text{Be, Mg, Ca, Sr, and Ba}$) and PbBO_3 ($B = \text{Ti, Zr, and Hf}$): First principles calculations," *J. Appl. Phys.*, vol. 117, no. 17, p. 174108, May 2015.
- [99] S. V. Krivovichev, "Minerals with antiperovskite structure: a review," *Zeitschrift für Krist. - Cryst. Mater.*, vol. 223, no. 1–2, pp. 109–113, Jan. 2008.
- [100] R. Sato *et al.*, "Formation process of perovskite-type hydride LiNiH_3 : *In situ* synchrotron radiation X-ray diffraction study," *Appl. Phys. Lett.*, vol. 102, no. 9, p. 091901, Mar. 2013.
- [101] S. Takagi *et al.*, "Density-functional study of perovskite-type hydride LiNiH_3 and its synthesis: Mechanism for formation of metallic perovskite," *Phys. Rev. B*, vol. 87, no. 12, p. 125134, Mar. 2013.

APPENDICES

A. BAND STRUCTURE AND PARTIAL DENSITY OF STATES FOR BaScO₃ PEROVSKITE COMPOUNDS

The band structure and corresponding partial density of states for BaScO₃ tetragonal, rhombohedral, hexagonal and cubic phases have been presented here. All these phases except the cubic phase have semiconducting behavior similar to the orthorhombic phase. The cubic phase shows metallic character. Table A.1 lists their band gaps and the following figures show their band structures and corresponding PDOS.

Table A.1 The band gaps for BaScO₃ tetragonal, rhombohedral and hexagonal phases

Phases	Band gap (eV)
Tetragonal	4.2
Rhombohedral	4.5
Hexagonal	3.0

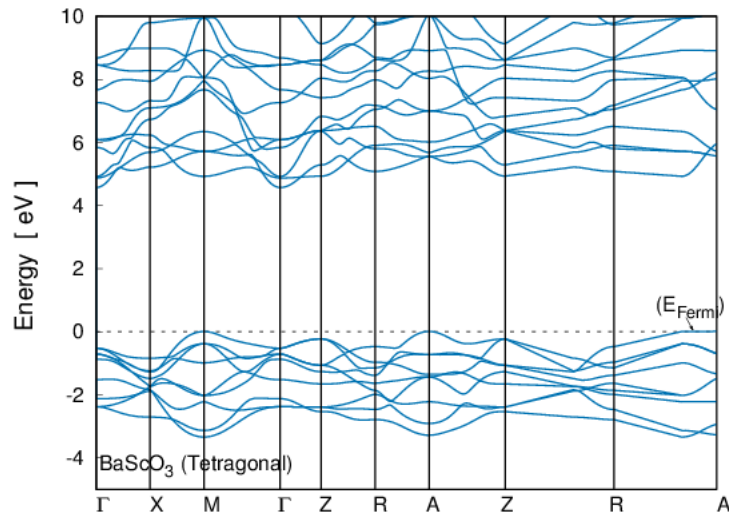


Figure A.1 The band structure for BaScO₃ tetragonal phase

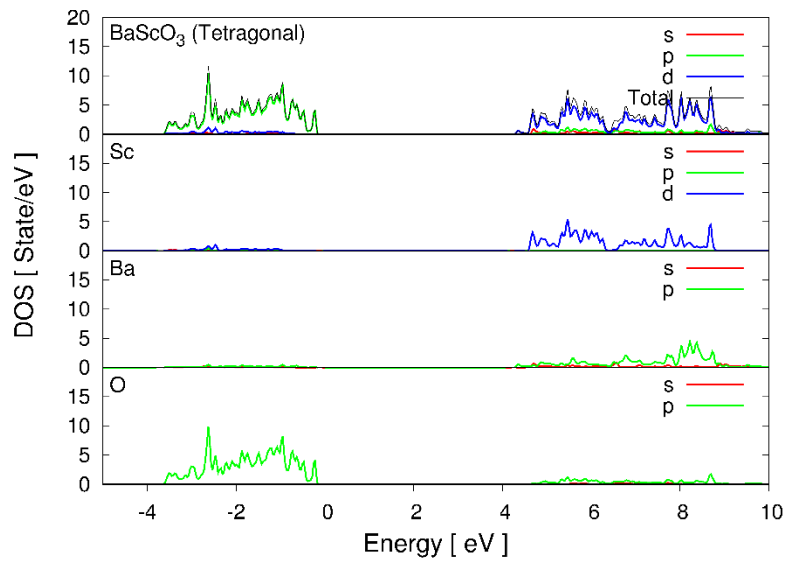


Figure A.2 The partial density of states for BaScO₃ tetragonal phase

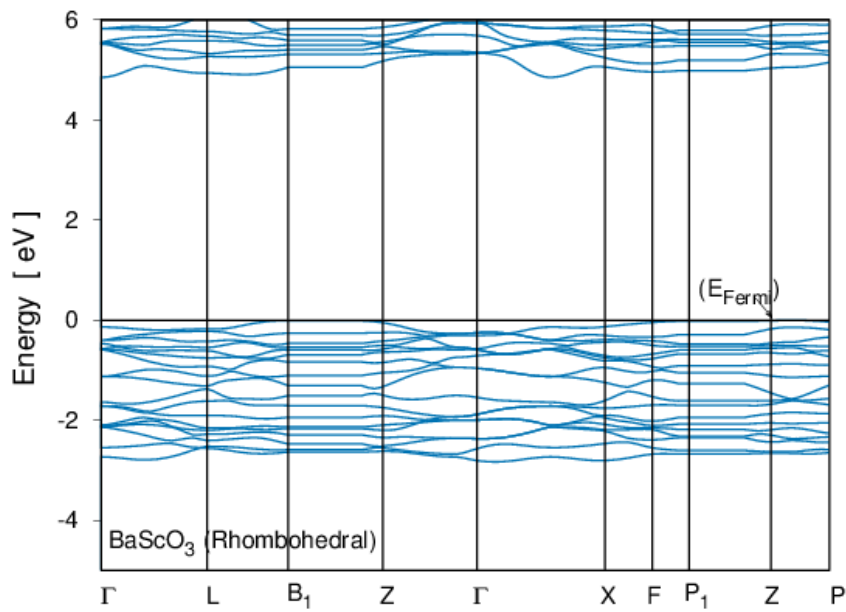


Figure A.3 The band structure for BaScO₃ rhombohedral phase

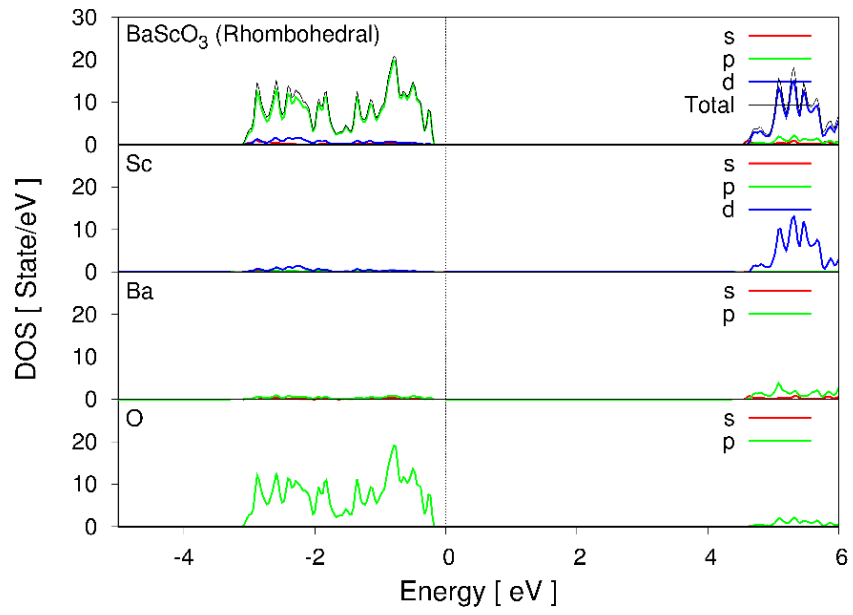


Figure A.4 The partial density of states for BaScO₃ rhombohedral phase

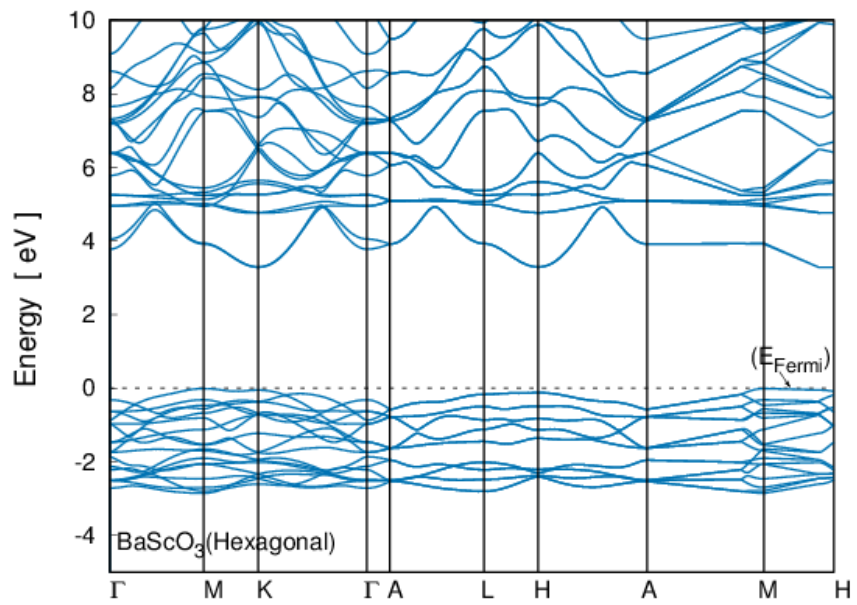


Figure A.5 The band structure for BaScO₃ hexagonal phase

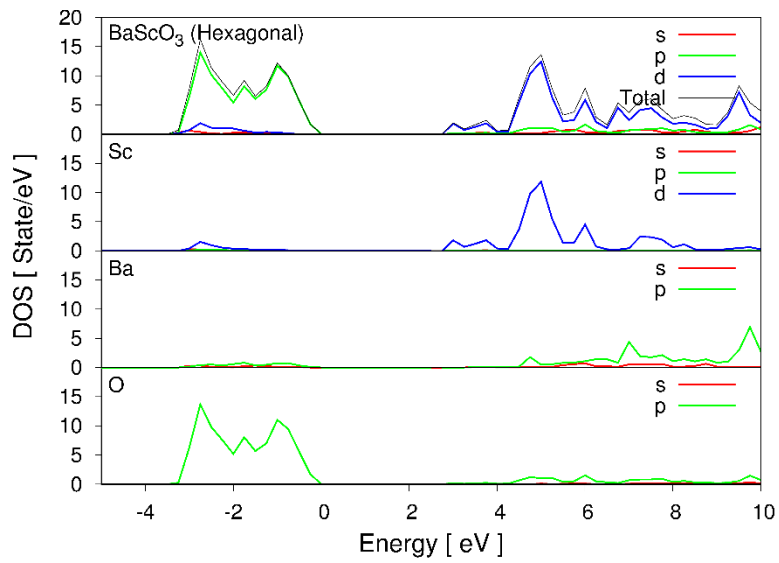


Figure A.6 The partial density of states for BaScO₃ hexagonal phase

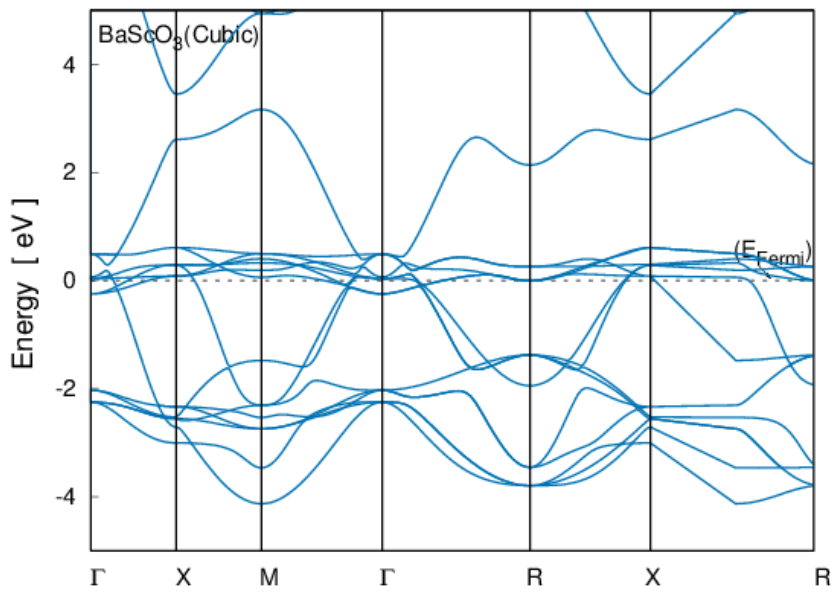


Figure A.7 The band structure for BaScO₃ cubic phase

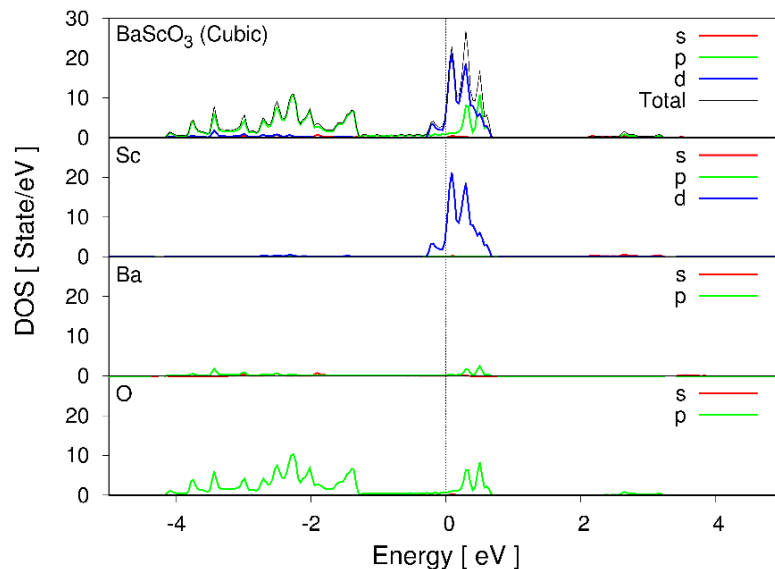


Figure A.8 The partial density of states for $BaScO_3$ cubic phase

Table A.2 lists the Bader net partial charges for $BaScO_3$ phases. Since the number of atoms differ from phase to phase, the Bader net charges differ for the same atom in different phases. General trend is the following: the charge is transferred away from Ba and Sc atoms while it is transferred to O atoms.

Table A.2 The Bader net charges (in units of e) for $BaScO_3$ phases

Ion	Tetragonal	Rhombohedral	Hexagonal	Cubic
Ba	1.55	3.53	3.45	1.66
Sc	1.92	3.90	3.71	1.79
O	-3.47	-7.43	-7.16	-3.45

The band structure and corresponding PDOS for $BaYO_3$ orthorhombic, tetragonal, rhombohedral, and hexagonal phases have been presented here. All these compounds except the orthorhombic phase have semiconducting behavior similar to the cubic phase. The orthorhombic phase shows metallic character. Table A.3 lists the band gaps and the following figures show the band structures and corresponding PDOS for these phases.

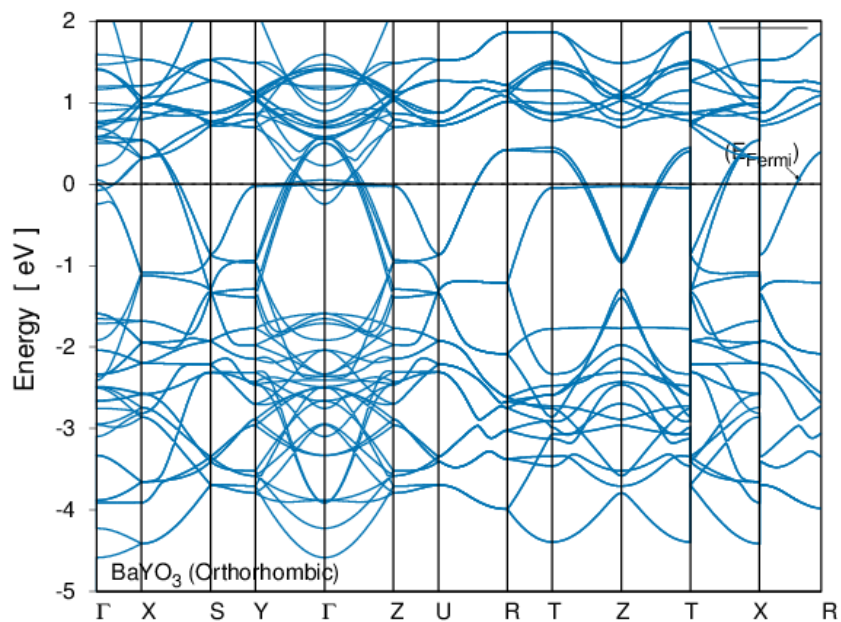


Figure A.9 The band structure for BaYO₃ orthorhombic phase

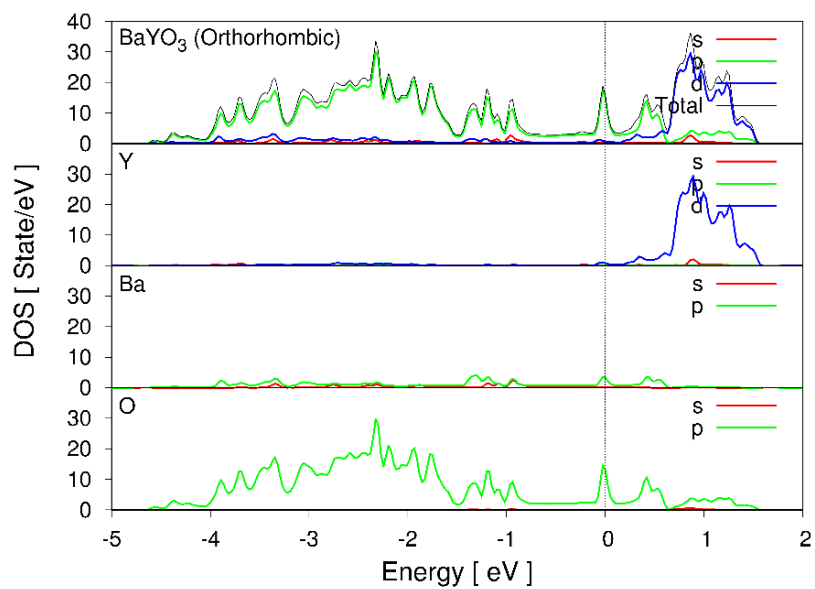


Figure A.10 The partial density of states for BaYO₃ orthorhombic phase

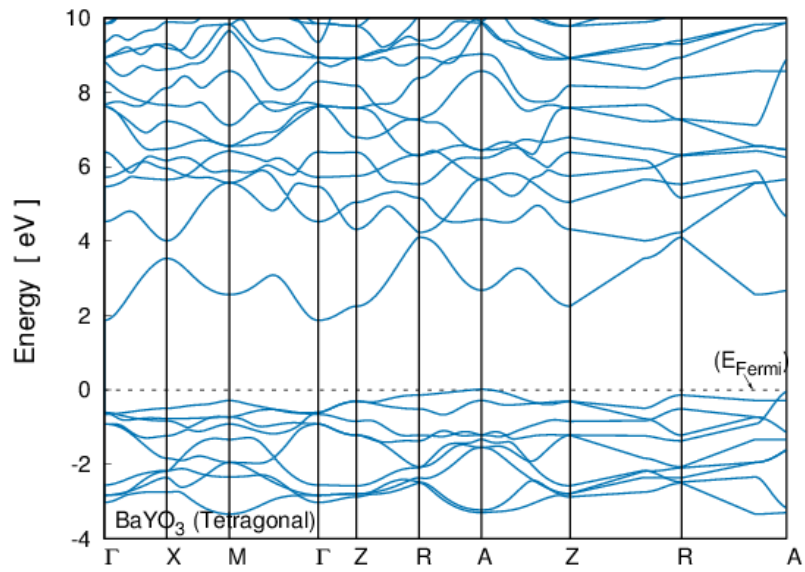


Figure A.11 The band structure for BaYO₃ tetragonal phase

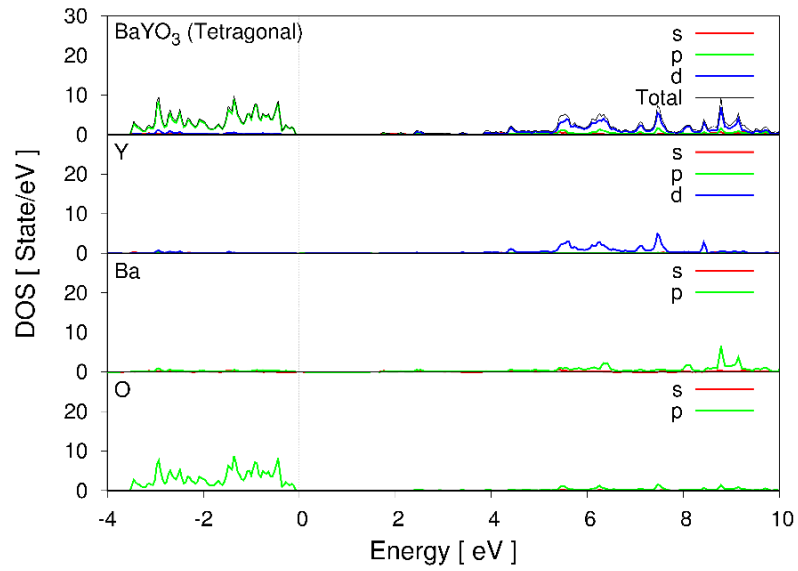


Figure A.12 The partial density of states for BaYO₃ tetragonal phase

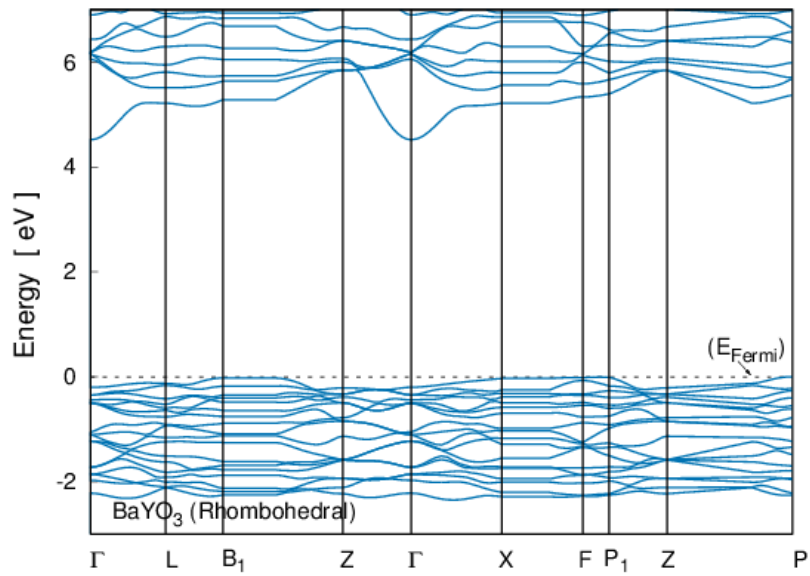


Figure A.13 The band structure for BaYO₃ rhombohedral phase

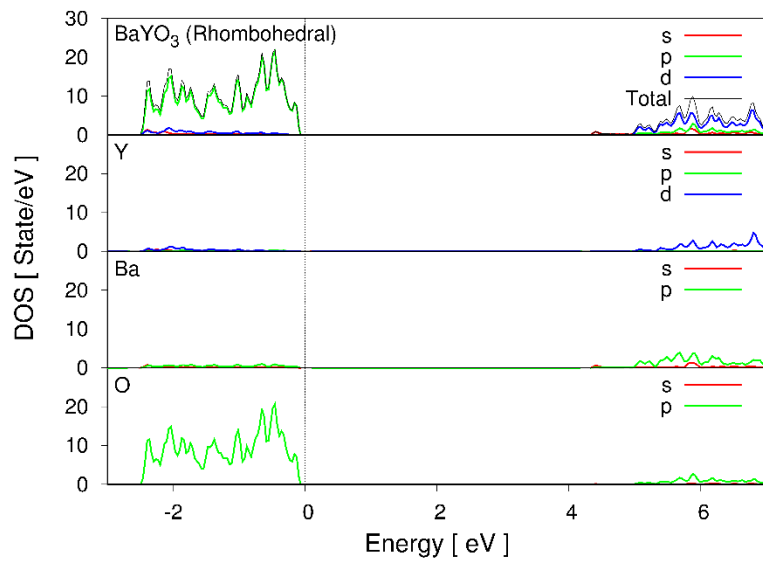


Figure A.14 The band partial density of states for BaYO₃ rhombohedral phase

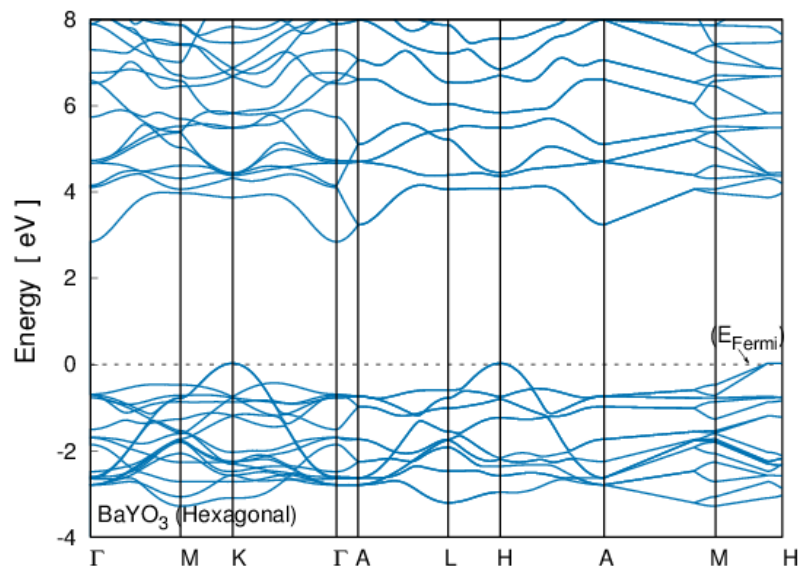


Figure A.15 The band structure for BaYO₃ hexagonal phase

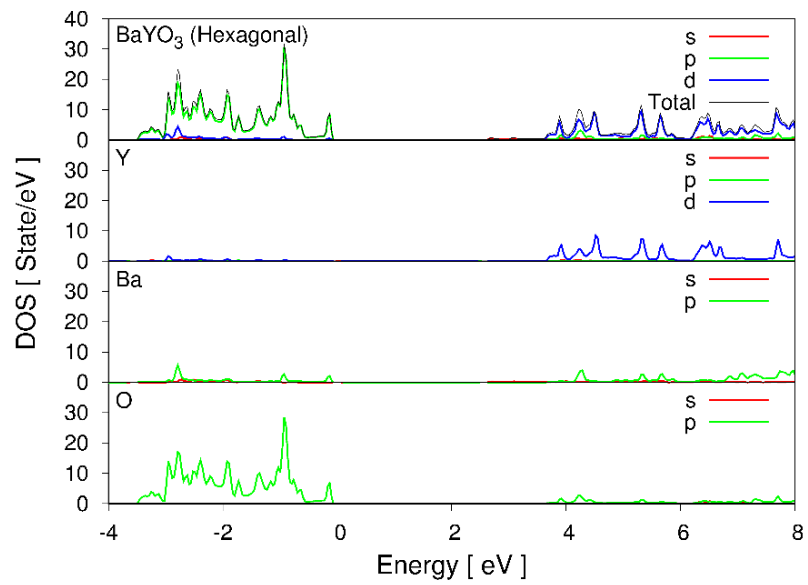


Figure A.16 The partial density of states for BaYO₃ hexagonal phase

Table A.3 The band gaps for BaYO₃ tetragonal, rhombohedral and hexagonal phases

Phases	Band gap (eV)
Tetragonal	1.7
Rhombohedral	4.3
Hexagonal	2.6

Table A.4 lists the Bader net partial charges for BaYO₃ crystal phases. For both phases, Ba and Y atoms give charge away, while O atoms take charge.

Table A.4 The Bader net charges (in units of e) for BaYO₃ phases

Ion	Orthorhombic	Tetragonal	Rhombohedral	Hexagonal
Ba	6.53	1.48	3.65	3.52
Sc	8.35	2.12	4.33	4.28
O	-14.88	-3.59	-7.98	-7.80

B. INPUT FILES FOR VASP

INCAR FILE:

SYSTEM = BaScO3

IBRION = 1

ISIF = 3

ICHARG = 1

PREC = H

EDIFF = 1.E-10

EDIFFG = -1.E-9

LREAL = F

LWAVE = F

LCHARG = F

ENCUT = 1000

NSW = 100

ADDGRID = T

ISMEAR = 1

SIGMA = 0.05

POSCAR FILE:

BaScO3

1

4.592141 0.000000 0.000000

0.000000 4.592141 0.000000

0.000000 0.000000 4.592141

O Sc Ba

3 1 1

Direct

0.50000000 0.00000000 -0.00000000

0.00000000 0.50000000 0.00000000

-0.00000000 0.00000000 0.50000000

0.50000000 0.50000000 0.50000000

0.00000000 0.00000000 -0.00000000

POTCAR FILE:

PAW_PBE O_GW 19Mar2012

6.000000000000000

parameters from PSCTR are:

VRHFIN =O: s2p4

LEXCH = PE

EATOM = 432.3788 eV, 31.7789 Ry

TITEL = PAW_PBE O_GW 19Mar2012

LULTRA = F use ultrasoft PP ?

IUNSCR = 1 unscreen: 0-lin 1-nonlin 2-no

RPACOR = 0.800 partial core radius

POMASS = 16.000; ZVAL = 6.000 mass and valenz

RCORE = 1.600 outmost cutoff radius

RWIGS = 1.600; RWIGS = 0.847 wigner-seitz radius (au A)

ENMAX = 434.431; ENMIN = 325.824 eV

ICORE = 3 local potential

LCOR = T correct aug charges

LPAW = T paw PP

EAUG = 1139.609

DEXC = 0.000

RMAX = 1.629 core radius for proj-oper

RAUG = 1.300 factor for augmentation sphere

RDEP = 1.652 radius for radial grids

RDEPT = 1.200 core radius for aug-charge

.....

KPOINTS FILE:

K-Mesh Generated with KP-Resolved Value (Low=0.08~0.05, Medium=0.04~0.03,
Fine=0.02~0.01): 0.015

0

Gamma

16 16 16

0.0 0.0 0.0

CURRICULUM VITAE

PERSONAL INFORMATION

Surname, Name : Gencer, Ayşenur
Nationality : Turkish (TC)
Date and Place of Birth : 12 May 1986, Polatlı
Phone : +90 505 365 06 35
E-mail : aysenurgencer@gmail.com

EDUCATION

Degree	Institution	Year of Graduation
PhD	METU	2019
BS	Gazi University Physics Education	2009
High School	TED Polatlı College	2004

WORK EXPERIENCE

Year	Place	Enrollment
2018-present	Karamanoğlu Mehmetbey University	Research Assistant
2011-2018	METU	Research Assistant
2010-2011	Karamanoğlu Mehmetbey University	Research Assistant

FOREIGN LANGUAGES

Advanced English

PUBLICATIONS

A. ARTICLES

A1. A. Gencer, G. Surucu, “Investigation of structural, electronic and lattice dynamical properties of $XNiH_3$ ($X=Li, Na$ and K) Perovskite Type Hydrides and their Hydrogen Storage Applications”, International Journal of Hydrogen Energy, in press, 2019, <https://doi.org/10.1016/j.ijhydene.2019.04.097>

A2. A. Gencer, G. Surucu, “DFT Study of $\text{BaScO}_3\text{H}_{0.5}$ Compound and Its Hydrogen Storage Properties”, accepted to publish in Canadian Journal of Physics.

A3. A. Gencer, G. Surucu, S. Al, ” MgTiO_3H_x and CaTiO_3H_x perovskite compounds for hydrogen storage applications”, International Journal of Hydrogen Energy, Volume 44, Issue 23, pp. 11930-11938, 2019, <https://doi.org/10.1016/j.ijhydene.2019.03.116>.

A4. İ. Yılmaz, U. Bayhan, A. Gencer, G. Surucu, "Anisotropic Elastic and Lattice Dynamical Properties of Cr_2AB MAX Phases Compounds". European Journal of Science and Technology, Number 15, pp. 351-359, 2019, doi: 10.31590/ejosat.510707.

A5. A. Gencer, G. Surucu, “Electronic and lattice dynamical properties of Ti_2SiB MAX phase”, Materials Research Express, Volume 5, Number 7, pp. 076303/1-9 2018, <https://doi.org/10.1088/2053-1591/aace7f>

A6. A. Gencer, B. Demirköz, I. Efthymiopoulos, M. Yigitoglu, “Defocusing beam line design for an irradiation facility at the TAEA SANAEM Proton Accelerator Facility”, Nucl. Instrum. Meth. A: 824, pp. 202-203, 2016, <http://dx.doi.org/10.1016/j.nima.2015.11.018>

A7. B. Demirköz, A. Gencer, D. Kiziloren, R. Apsimon, “Proposal for an irradiation facility at the TAEK SANAEM Proton Accelerator Facility”, Nuc. Instrum. Meth. A:730, pp. 232-234, 2013, <http://dx.doi.org/10.1016/j.nima.2013.06.022>

B. ORAL PRESENTATIONS

B1. A. Gencer, G. Surucu, “Hydrogen Storage Properties of CaTiO_3H_x and MgTiO_3H_x ”, International Computational Science Congress (CSC), 26-28 October 2018, Amasya, Turkey.

B2. G. Surucu, A. Gencer, “Properties of LiNiH_3 and NaNiH_3 Perovskite Type Hydrides for Hydrogen Storage Applications”, International Computational Science Congress (CSC), 26-28 October 2018, Amasya, Turkey.

B3. A. Gencer, G. Surucu, “Hydrogen Storage Properties of MgTiO_3H_x ”, International Congress on the World of Technology and Advanced Materials, 21-23 September 2018, Kırşehir, Turkey.

B4. A. Gencer, G. Surucu, “Mechanical, Vibrational and Thermodynamical Properties of Ti_2SiB MAX Phase”, International Congress on the World of Technology and Advanced Materials, 21-23 September 2018, Kırşehir, Turkey.

B5. A. Gencer, G. Surucu, “DFT Study of $\text{BaScO}_3\text{H}_{0.5}$ Compound and Its Hydrogen Storage Properties”, 34th Turkish Physical Society International Physical Congress, 5-9 September 2018, Bodrum, Turkey.

B6. İ. Yılmaz, Ü. Bayhan, A. Gencer, G. Sürücü, “Anisotropic Elastic and Lattice Dynamical Properties of C_{r2}AB MAX Phases Compounds”, 34th Turkish Physical Society International Physical Congress, 5-9 September 2018, Bodrum, Turkey.

B7. A. Gencer, G. Surucu, “Properties of BaYO_3 Perovskite and Hydrogen Storage Properties of BaYO_3H_x ”, 13th Advanced Nanomaterials Conference, 18-20 July 2018, Aveiro, Portugal.

B8. A. Gencer, G. Surucu, “Hydrogen Storage Properties of BaScO₃H_x Perovskite”, EMRS 2018 Spring Meeting, 18-22 June 2018, Strasbourg, France.

B9. M. B. Demirköz, A. Gencer, et. al., “Pretest Setup Installation of the METU-DBL Project to Perform Space Radiation Tests”, 8th International Conference on Recent Advances in Space Technologies, 19-22 June 2017, İstanbul, Turkey.

B10. A. Gencer, B. Bodur, M. B. Demirköz, I.Efthymiopoulos, R. Uzel, D. Veske, M. Yigitoglu, “Space Radiation Effects and Irradiation Tests of Semiconductor Devices in Turkey”, at RAD-2017, the 5th Int. Conf. on Radiation and Applications, 12-16 June 2017, Budva, Montenegro.

B11. A. Gencer, M. B. Demirköz, I. Efthymiopoulos, M. Yigitoglu, “Construction of METU Defocusing Beam Line at Turkish Atomic Energy Authority Proton Accelerator Facility and Performing Single Event Effect Tests”, 11th National Nuclear Science and Technologies Congress, 12-14 October 2016, Kuşadası, Turkey

B12. M. B. Demirköz, A. Gencer, M. Yigitoglu, “A Radiation Hardness Test Facility to Perform SEE Tests in Turkey”, SCI- 283 Symposium on Considerations for Space and Space-Enabled Capabilities in NATO Coalition Operations, 17-18 May 2016, Loughborough, United Kingdom

B13. M. B. Demirköz, A. Gencer, D. Kiziloren, R. Apsimon, “Proposal for an Irradiation Facility at the TAEK SANAEM Proton Accelerator Facility”, 9th Int. Conference on Radiation Effects on Semiconductor Materials and Devices, 9-12 October 2012, Florence, Italy

B14. V. Damli, B. Günes., R. Salar, A. Gencer, "Development of a Conceptual Test on Fluid Dynamics for Physics Teachers", 10th National Science and Mathematics Education Congress, 27-30 June 2012, Nigde, Turkey.

B15. U. Kanli, V. Damli, A. Gencer, P. Ünlü, B. Günes, "Determination of Science and Physics Teacher Candidates' Misconceptions about Basic Astronomy Concepts with a Three-tier Test", GIREP – ICPE - MPTL 2010 Int. Conf. 22 - 27 August 2010, Université de Reims Champagne Ardenne, Reims, France.

C. POSTER PRESENTATIONS

C1. A. Gencer, G. Sürücü, "BaScO₃ Bileşiminin Yapısal ve Elektronik Özelliklerinin İncelenmesi", 23rd Condensed Matter Physics Meeting Ankara, 22 Dec 2017, Ankara, Turkey.

C2. A. Gencer, G. Sürücü, "Anisotropic Elastic Properties of BaScO_{3-x}H_x Compounds", International Conference on Condensed Matter and Materials Science (ICMMS-2017), 11-15 Oct 2017, Adana, Turkey.

C3. A. Gencer, et al., "Preliminary Testing and Results from the METU Defocusing Beam Line, an Irradiation Test Facility in Turkey", IPAC'17, the 8th Int. Particle Accelerator Conference, 14-19 May 2017, Copenhagen, Denmark.

C4. A. Gencer, B. Demirköz, I. Efthymiopoulos, M. Yigitoglu, "Defocusing Beam Line Design for an Irradiation Facility at the TAEA SANAEM Proton Accelerator Facility", 13th Pisa Meeting, 24-30 May 2015, Elba, Italy.

C5. A. Gencer, M. B. Demirköz, I. Efthymiopoulos, M. Yigitoglu, "Defocusing Beam Line Design for an Irradiation Facility", Ankara National Physics Workshop, 12-14 February 2015, Ankara, Turkey.

